Delft University of Technology

Master Thesis

A study on the use of aluminium etching solution as an alkali activator

By:

Sep Hesselmans

studentnumber: 4860365

To obtain the degree of Master of Science in Civil Engineering at Delft University of Technology

Guided by:

Prof. Guang Ye

Dr. Shizhe Zhang

Dr. Mladena Luković

Delft - 3/11/2024

Preface

This master thesis represents the final step toward earning my Master degree in Civil Engineering, specializing in construction materials. Throughout my bachelor and master studies, the ambition to develop concrete with a low environmental impact has frequently crossed my mind, yet it often seemed out of my reach. However, upon choosing the specialization track: construction materials, this ambition became increasingly realistic.

I would like to express my deepest gratitude to Dr. Shizhe Zhang and Prof. Guang Ye for providing me with the opportunity to explore this fascinating field of study. From the moment the project was presented during a coffee break, I was intrigued by the prospect of researching ways to reduce the environmental impact of an already sustainable alternative binder while potentially transforming waste into valuable raw materials, an idea that had crossed my mind during my studies.

This research included both modeling and experimental work, which would not have been successful without the support of numerous colleagues. I would like to thank Luiz Miranda de Lima for his guidance in GEMS, including a valuable introduction to the program. I am also grateful to John van den Berg, Ton Blom, Arjan Thijssen, and Maiko van Leeuwen for their assistance in the laboratory, where they explained various experimental procedures and provided valuable insights and of course were always in for a good laugh. A special acknowledgment goes to Xuhui Liang for his help in initiating the experimental procedures and for offering useful tips and insights throughout my thesis.

I would like to extend my gratitude to my thesis committee: Prof. Guang Ye, Dr. Shizhe Zhang, and Dr. Mladena Luković. To Dr. Shizhe Zhang, my daily supervisor, I am thankful for the valuable discussions we had throughout the thesis, which always gave new insights and for your guidance in navigating this complex area of research. To Prof. Guang Ye, the committee chair, I appreciate the trust you placed in me to conduct this research and for your invaluable support. Lastly, I am grateful to Dr. Mladena Luković for the insightful suggestions and feedback during our progress meetings, which were of great value to me.

And finally, I want to thank my friends and family who supported me throughout my academic journey.

Sep Hesselmans

November 12, 2024

Delft

Abstract

The construction industry faces significant environmental challenges due to its reliance on Portland cement, which accounts for up to 7% of global CO_2 emissions (Benhelal, Zahedi, Shamsaei, & Bahadori, 2013). In the Netherlands, initiatives like the "Betonakkoord" aim to mitigate these emissions. Geopolymer concrete, which utilizes alkali-activated binders derived from industrial byproducts, presents a promising alternative. However, the carbon footprint associated with conventional activators remains a concern. This research investigates the viability of using waste aluminium etching solutions as a sustainable source of alkali activators, with the goal of minimizing the environmental impact of geopolymer concrete and providing a practical recycling pathway for waste aluminium etching solutions.

The research begins with the characterization of the aluminium etching solution received from APT Extrusions B.V., which serves as the basis for thermodynamic modelling to assess the influence of activator composition on reaction products. This modelling informs the development of six distinct mixture designs based on a BFS precursor, each varying in activator composition. The experimental study is organized into three sections: the first investigates the reaction process through dissolution tests, isothermal calorimetry, and pore solution chemistry; the second examines the fresh and hardened properties, including setting time and strength; and the third presents an analysis of the reaction products using techniques such as TGA, XRD, FTIR, and SEM-EDS.

The results indicate that aluminium-containing activators significantly influence reaction kinetics, initially delaying strength development. However, mixtures with higher aluminium content exhibit enhanced long-term strength due to increased geopolymerization and the formation of more cross-linked C-(N-)A-S-H gel phases. The delayed reaction kinetics are attributed to the passivation of Si sites and the formation of metastable phases, which temporarily impede the dissolution of slag particles. Although aluminium etching solutions can improve the mechanical performance of the mixtures, optimizing aluminium concentration is critical to avoid shrinkage-induced cracking. To validate this optimization, a new mixture was developed to prevent crack formation while enhancing strength development using the aluminium etching solution.

This study underscores the potential of aluminium etching solutions as eco-friendly activators in the production of sustainable cement alternatives. Given the promise of this byproduct, future research should focus on the dissolution behavior of the precursor in the new activator, detailed investigations of the reaction kinetics within the early age, and an in-depth exploration of metastable phases. Additionally, a comprehensive understanding of fresh and hardened properties, with a particular emphasis on autogenous shrinkage, will be essential for practical applications.

Contents

List of acronyms

AAM	Alkali Activated Material(s)
AAP	Alkali Activated Paste
BFS	Blast Furnace Slag
COV	Coefficient Of Variation
DoR	Degree of Reaction
EDS	Energy Dispersive X-ray Spectroscopy
FA	Fly Ash
FRB	Flowing Rinsing Bath
FTIR	Fourier Transform Infrared spectroscopy
GEMS	Gibbs Energy Minimization Software
$\mathbf{H}_{FP}$	Height of the first peak (isothermal calorimetry)
$\mathbf{H}_{SP}$	Height of the second peak (isothermal calorimetry)
IC	Ionic Chromatography
ICP-OES	Inductively Coupled Plasma Optical Emission Spectrometer
MCL	Mean Chain Length
NBO/T	Non-Bridging Oxygen atoms over tetragonal coordinated atoms
OPC	Ordinary Portland Cement
SEM	Scanning Electron Microscope
SRB	Stationary Rinsing Bath
$\mathbf{T}_{FP}$	Time till the first peak (isothermal calorimetry)
TGA	Thermogravimetric Analysis
$\mathbf{T}_{SP}$	Time till the second peak (isothermal calorimetry)
XRD	X-Ray Diffraction
XRF	X-Ray Fluorescence
	...

List of Figures

List of Tables

1 Introduction

1.1 Background and research problem

Concrete is the most widely used construction material globally, with annual production volumes reaching billions of tons. A key component of concrete is its binder, which provides the material with its strength and stability. Since the invention of Portland cement in the 19th century, this material has been the primary binder in conventional concrete. However, Portland cement presents a significant contemporary challenge due to its high carbon dioxide (CO_2) emissions. The concrete industry is responsible for up to 7% of global CO_2 emissions, making it a major contributor to climate change (Benhelal et al., 2013).

In the Netherlands, efforts to reduce the environmental impact of concrete are formalized in the "Betonakkoord" (Concrete Agreement), which sets ambitious goals for reducing CO_2 emissions from concrete by 30% relative to 1990 levels, and for fully recycling construction and demolition waste by 2030(BetonAkkoord, 2018). To meet these targets, alternative binders are being explored to replace Portland cement in concrete production. One promising solution to mitigate the high emissions of conventional concrete is geopolymer concrete. This type of concrete utilizes an alkali-activated binder, often originating from industrial by-products, as a substitute for cement.

Alkali-activated binders consist of a precursor and an activator, which react to form a solid binder. The precursor, analogous to cement, does not react with water alone but requires an alkali activator. The activator creates an environment which benefits the dissolution and reaction of the precursor. Commonly, precursors are industrial by-products, while the activators are typically produced through industrial processes and thus remain a notable source of CO_2 emissions.

By recovering alkali activators from waste streams, the overall emissions associated with geopolymer concrete could be further reduced. One potential source of such activators is the aluminium anodizing industry, where alkaline solutions are used in etching baths. These solutions, once saturated and discarded by the industry, have the potential to serve as alkali activators. Research on its viability as a sustainable activator is still limited. Further investigation is needed to confirm its feasibility.

The field of research on alkali-activated materials is relatively recent but has experienced significant growth in recent years. Studies have explored various precursors, including both industrial by-products and other precursors such as metakaolin, for use in alkali-activated systems. While much of this research has focused on the combination of these precursors with commercially manufactured alkali activators, the use of industrial by-products as activators remains underexplored. The potential variability among these by-products as activators introduces considerable complexity into this line of research.

Previous research has extensively investigated the composition of common used alkali activators, the reaction products formed in conjunction with specific precursors, and the mechanical properties of the resulting materials. However, the examination of industrial by-products as potential activators is still in its early stages, and there is currently no standardized guideline on how to process these by-products for use as activators in alkali-activated systems.

The critical gap in the current literature is the lack of integration between by-product analysis, activator development, and the performance evaluation of resulting geopolymers. This research seeks to address this gap by investigating the use of industrial by-products as activators and presenting key findings that provide insights into activator development from such materials.

1.2 Research objectives

This research aims to study the feasibility of using the saturated aluminium etching solution as an activator in alkali-activated paste (AAP). This includes the following research objectives.

- To characterize the composition of the aluminium etching solution and to determine its stability.
- To develop a predictive model in GEMS for forecasting the reaction products formed during the interaction between the activator and the precursor.
- To clarify the reaction mechanisms, micro-structural development, and mechanical properties of AAPs prepared with the aluminium-containing activator.
- To explain the mechanical behavior of the mixtures and presenting key findings and recommendations based on the observations.

1.3 Scope of the current study

This research focuses on the use of a specific industrial by-product, the saturated aluminium etching solution, as an activator in alkali-activated materials (AAM). The primary emphasis is placed on the activator rather than the precursor. Various activators derived from the etching solution will be developed and tested to assess their effects. For comparison, commonly used reference activators, such as sodium hydroxide solutions, will also be included. The study is limited to the investigation of alkali-activated pastes, without considering geopolymer concretes or mortars. The precursor selected for this research is blast furnace slag (BFS) due to its well-documented and favorable engineering properties.

1.4 Research structure

This research will be divided into separate sections, this being the following.

- Literature review
- Characterization of the aluminium etching solution
- Thermodynamic modelling
- Experimental work
- Key findings and recommendations

The literature review focuses on basic knowledge of alkali activated materials and will review more state of the art concepts related to activators containg aluminium. As a start of the experimental work, the aluminium etching solution is characterized, giving insight in the composition and data that can be used for mixture design. Based on the composition of the solution, thermodynamic modelling is performed using Gibbs Energy Minimization Software (GEMS), which predicts the reaction products that form, based on the mixture design presented to the model. The modelling gives important guidance into different mixture designs which are investigated in the experimental work. The experimental work itself is divided into subsections, this being the reaction process, the reaction products and the fresh and hardened properties. Finally all the results are analyzed and discussed and the key findings are presented, together with recommendations for further research. The structure of the research is visualized in the framework shown in Figure 1

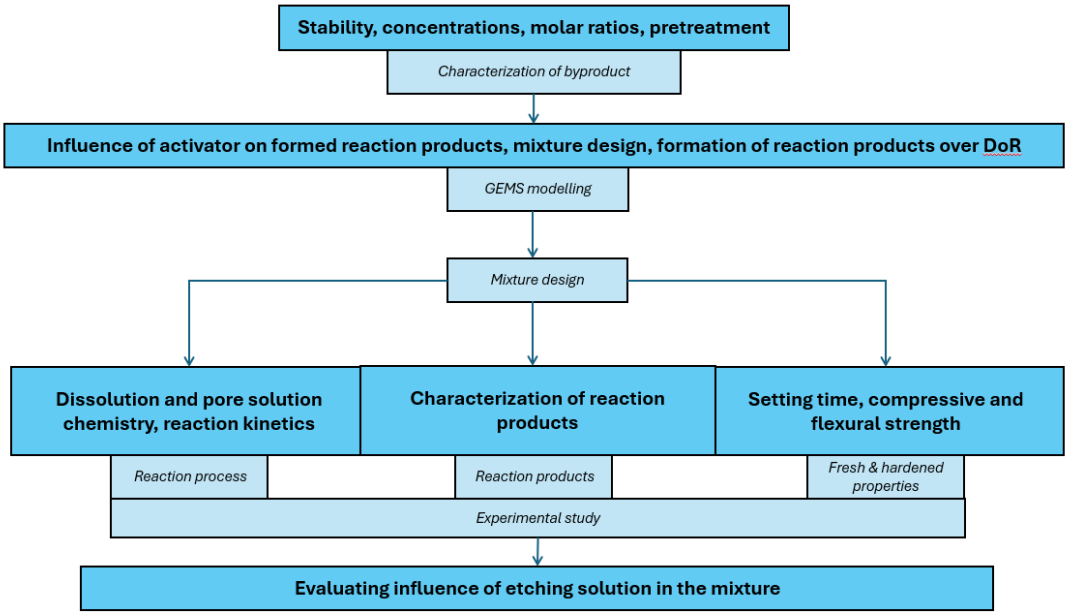

Figure 1: Framework of the research

2 Literature review

The literature review examines key aspects of alkali-activated materials (AAMs), progressing from foundational concepts to current advancements. Sections 2.1 and 2.2 introduce essential principles of AAMs, providing a basis for understanding the broader context. Sections 2.3, 2.4 and 2.5 then present a state-of-the-art analysis of aluminium etching solutions, their influence on reaction processes, and the role of aluminium-containing activators. Together, these sections outline both fundamental concepts and the potential applications of aluminium etching solutions in enhancing AAM performance.

2.1 Blast Furnace Slag

Blast furnace slag is an industrial by-product in steel production. When the iron ore, coke and limestone are placed in the blast furnace, the two fractions that will be produced are molten iron and molten slag. The slag has a lower density compared to the iron, meaning the separation of the two fractions is quite easy. The composition of BFS is quite uniform, consisting out of mainly silica (SiO_2), alumina (Al_2O_3) and lime (CaO) combined with some other elements as magnesium, sulfur and some oxides (Yuksel, 2018). The BFS shows, once granulated to a very fine fractions, hydraulic properties and is already been used as an constituent in Portland Blast-Furnace-Slag cement (CEM III/B). The reactivity of the granulated blast furnace slag (GBFS) is a complex property and it depends on a lot of different factors such as chemical composition of the slag, fineness, processing temperature, glass structure and the alkali environment (Yuksel, 2018).

The main components of BFS, in oxide forms, are MgO, Al_2O_3, SiO_2 and CaO. The hydraulic activity is influenced by the ratio of these components. Different equations are created to reflect the hydraulic reactivity of the BFS. The equations that reflect the reactivity of the BFS are shown in Table 1 (G. Ye, 2023) (Yuksel, 2018).

Table 1: Design equations for mixture design with BFS as solid precursor

Equation	Description
$\frac{CaO+MgO+Al_2O_3}{SiO_2+(TiO_2)}$	K_q, Quality coefficient ≥ 1.4
$\frac{CaO+1.4MgO+0.56Al_2O_3}{SiO_2}$	Alternative for K_q
$\frac{CaO+MgO}{SiO_2+Al_2O_3}$	K_b, Basicity coefficient ≥ 1.0
$\frac{CaO}{SiO_2}$	Value should be larger than 0.5 and smaller than 2.0
$\frac{Al_2O_3}{SiO_2}$	Value should be larger than 0.1 and smaller than 0.6

With an increase of both K_q and K_b, the reactivity of the BFS increases (G. Ye, 2023). In addition to the ratios presented in Table 1, it is important to note that an increase in MgO content may enhance the strength of alkali-activated materials (AAMs), while an increase in Al_2O_3 content can reduce early-age strength in alkali activated slag, regardless of the activator employed. Beyond the chemical composition, the reactivity of the precursor is also influenced by its glassy phase content and particle size. A higher glassy phase-to-crystalline phase ratio correlates with increased reactivity, and a finer precursor particle size further promotes this reactivity (G. Ye, 2023).

2.2 NaOH activator

BFS shows very low reactivity when mixed with only water. In order to accelerate the dissolution of the solid precursor, a medium with an increased pH is desired. A method to facilitate this increased pH is by using alkali activators which consist out of an alkali dissolved in water, which goes paired with hydroxide ions to balance the charge, resulting in an increased pH (Lambert & Mangat, 2016). Besides the increased pH, the alkali ion acts as a catalyzer in the early stage of the reaction via cationic exchange with the Ca ions and over time the alkali ions will be incorporated in the structure formed. This process was firstly described by Glukhovsky (Glukhovsky, 1994). Different alkali activators can be applied for AAMs, but this research will focus on NaOH as it will be used for reference later in the research. The process of how the alkali activator will accelerate the dissolution of the precursor, and thus the reaction, is visualised in Figure 2.

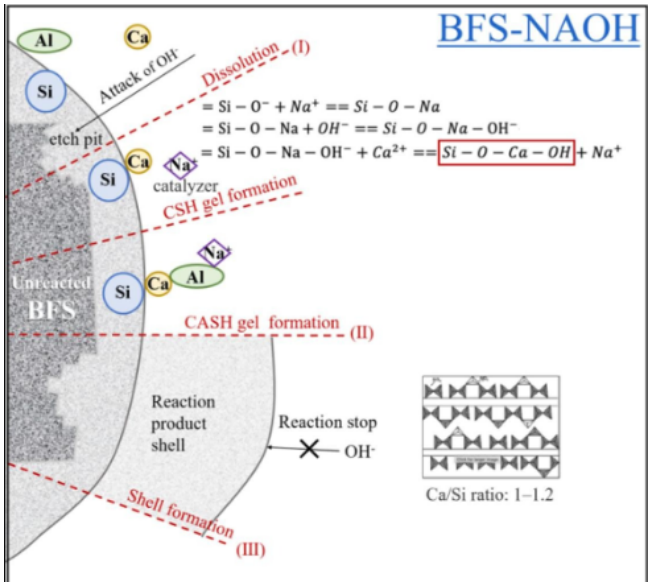

Figure 2: Mechanism of the BFS-NaOH reaction (B. Sun et al., 2022)

The accelerated dissolution by the attack of OH ions on BFS is shown in Figure 2. The oxides present in the BFS dissolve into ions such as Al, Si and Ca. Together with the present alkali ions (Na), reaction products can precipitate into thermodynamic stable phases. For mixture design, the alkali's are expressed in the weight percentage of present sodium oxide (Na_2O) relative to the precursor. When using NaOH as activator, it should be noted that a small calculation has to be made to transform it to Na_2O. The reaction that has to be taken into account can be seen in Equation 1.

$$Na_2O + H_2O \rightarrow 2NaOH \tag{1}$$

2.3 The aluminium etching solution

Within the aluminium industry, there is a specialized sector, which focuses on the anodizing of aluminium products. Anodizing is performed to obtain resistance against corrosion and for aesthetic value. The anodizing process exists out of multiple sections which are visualized in Figure 3.

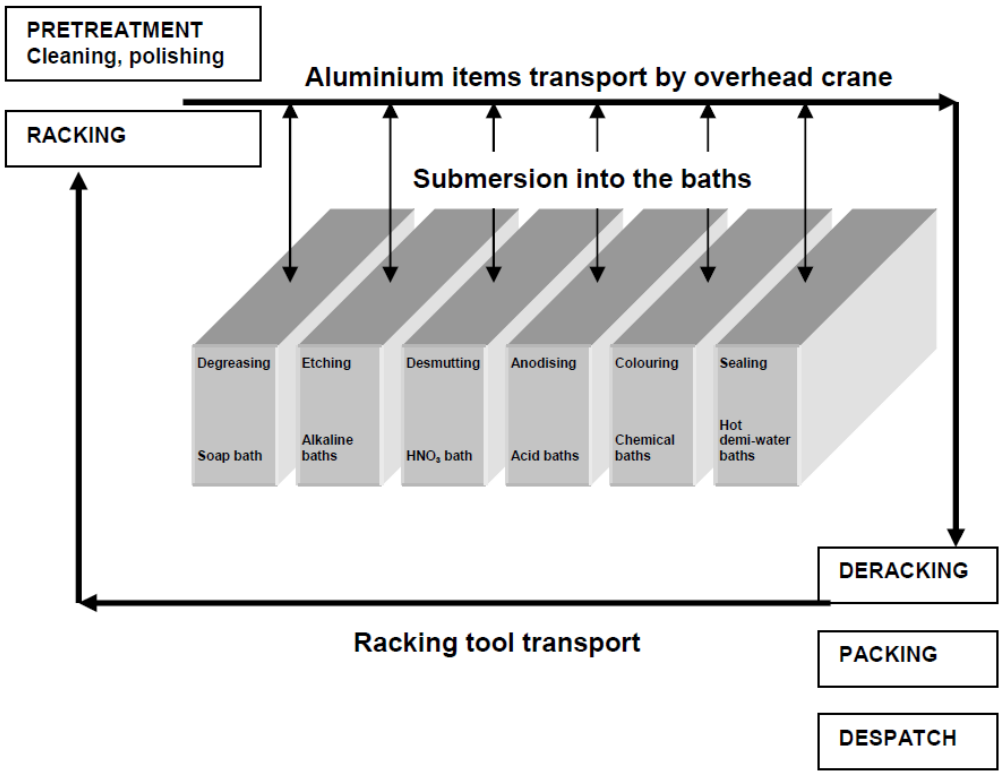

Figure 3: Overview of the aluminium anodizing process (Nugteren, 2010)

This research exclusively uses a by-product originating from the etching process. The etching procedure is illustrated in Figures 4 and 5, which depict two commonly used methods. In both processes, two baths, E0 and E6, are employed. Bath E0 is reserved for particularly intensive tasks and for cleaning the racks that hold the aluminium products, while bath E6 serves as the initial bath for standard operations.

In the stationary etching process, the aluminium products are first submerged in bath E6 for 15 to 20 minutes. Afterward, they are transferred to two stationary rinsing baths (SRB1 and SRB2) and then to a flowing rinsing bath (FRB). The stationary etching process is shown in Figure 4.

The Al concentration in bath E6 can be regulated by controlling the drip-off time of the treated products. Since some of the liquid from bath E6 drips into SRB1, the concentrations of NaOH and Al in SRB1 will rise over time. Once these concentrations surpass certain thresholds, SRB1 is emptied and refilled with the contents of SRB2, which in turn is replenished with water from the FRB. The FRB is then refilled with fresh water. As the liquid from bath E6 drips into SRB1, NaOH and other additives are lost to SRB1 and must be replenished in bath E6 to maintain its effectiveness.

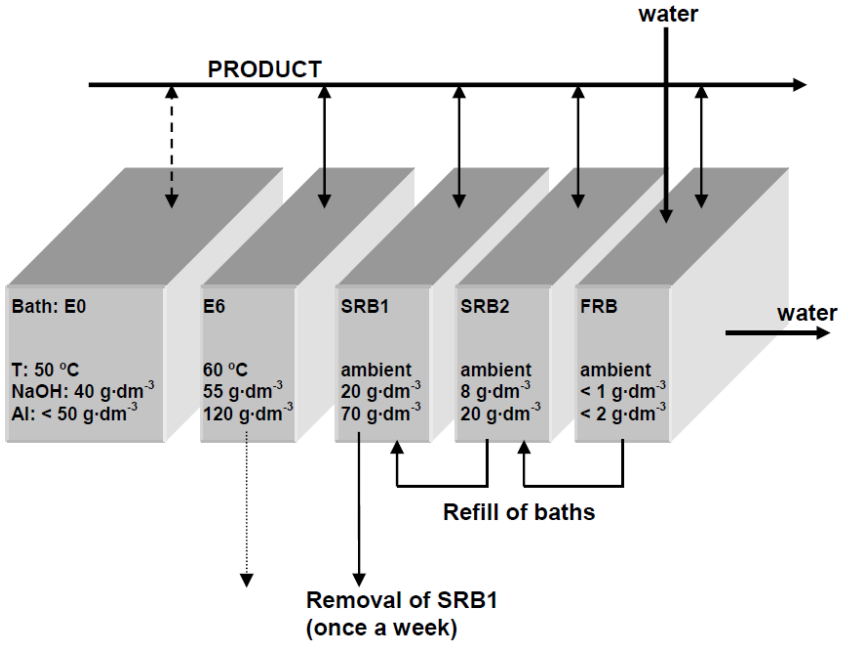

Figure 4: Stationary etching procedure (Nugteren, 2010)

The alternative method, known as the flowing etching process, differs significantly from the stationary etching procedure. In this approach, the stationary rinsing baths SRB1, SRB2, and FRB are replaced with a series of flowing rinsing baths: FRB1, FRB2, and FRB3. A constant flow is maintained from FRB3 to FRB1, with FRB3 containing the lowest concentrations and FRB1 the highest. This arrangement results in a continuous discharge of wastewater from FRB1, with concentration levels comparable to the solution from SRB1 in the stationary etching process. The flowing etching procedure is shown in Figure 5.

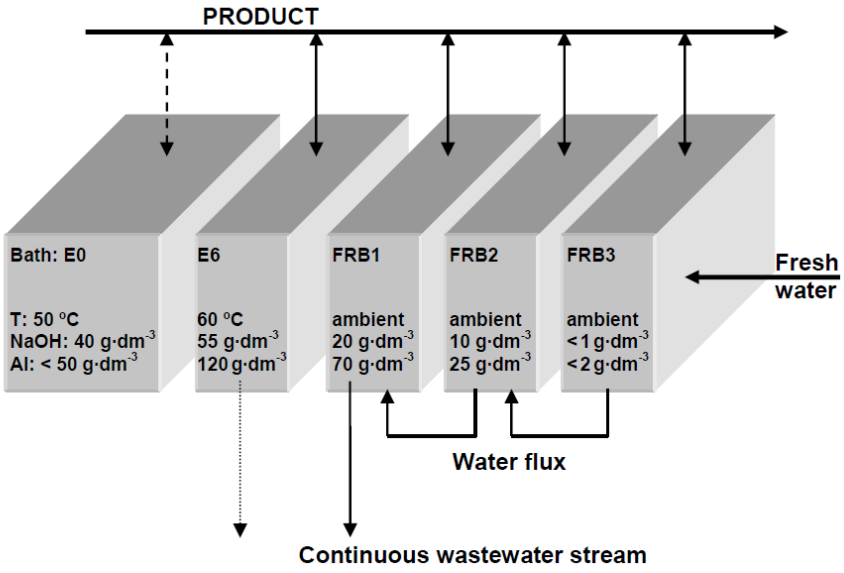

Figure 5: Flowing etching procedure (Nugteren, 2010)

In addition to describing the anodizing process, previous literature also examined the composition of the saturated etching solution and the suspended solids within it (Nugteren, 2010). The composition of two solutions from different anodizing plants was analyzed, each employing different methods for treating aluminium products. The first sample originated from a plant utilizing stationary rinsing baths (SRB), where the primary source of waste was the rinsing bath, as aluminium carryover from the etching bath accumulated in this bath. The second sample came from a plant that minimized aluminium-rich fluid spillover into the rinsing baths, allowing

the rinsing baths to be discharged into the sewage system. In this case, the etching bath (E6) required more frequent replenishment and thus became the main source of waste. Both solutions exhibited a dark coloration, which was attributed to precipitation occurring in the liquid. This precipitation was partly due to additives introduced to prevent the formation of aluminium oxides or hydroxides, and also to precipitate metals such as zinc (Zn), copper (Cu), and lead (Pb) as sulfides, which would otherwise negatively affect the surface quality of the products.

To analyze the composition of the solids and the liquid in the solutions, it is reported that the samples were filtered using a 0.45 μm membrane filter. The compositions of both the rinsing bath and main etch bath post-filtration were determined by ICP-OES, highlighting the differences in concentrations of both solutions. The concentrations in the rinsing bath and main etch bath can be seen in Table 2.

Table 2: Composition of the filtered aluminium etching solution, determined by ICP (Nugteren, 2010)

Solution	Al ($g \cdot kg^{-1}$)	Na ($g \cdot kg^{-1}$)	S ($g \cdot kg^{-1}$)	Zn ($mg \cdot kg^{-1}$)	Cr ($mg \cdot kg^{-1}$)	Si ($mg \cdot kg^{-1}$)	Mg ($mg \cdot kg^{-1}$)
Rinsing bath	51.6	52.6	1.71	< 1	3.8	267	< 1
Main etch bath	95.9	101	5.89	< 1	3.7	461	2.0

It is important to note that the presence of sulfate in the solution could potentially pose challenges in the context of geopolymers due to sulfate attack and aesthetic appearance as sulfate could darken the color. However, it is reported that neither the precipitated sulfates nor the use of the aluminium etching solution in geopolymers caused issues or affected the color of the mixture (Nugteren, 2010).

The composition of the precipitates was determined by performing X-Ray diffraction (XRD) and X-Ray fluorescence (XRF). The XRD showed that the main constituent of the filter residue was $NaAlO_2$ and this corresponded with the findings of the XRF where the two main oxides that were found were Al_2O_3 and Na_2O, both in the weight percentages corresponding to that of when the crystalline phase $NaAlO_2$ is present (Nugteren, 2010).

$$Na_2O + Al_2O3 \rightarrow 2 \cdot NaAlO_2 \tag{2}$$

With the molar weights of Na_2O and Al_2O_3 being approximately 62 [g/m] and 102 [g/m] respectively, the weight percentage of Na_2O is approximately 61% within $NaAlO_2$.

$$\frac{61.98}{101.96} \cdot 100 = 60.8\% \tag{3}$$

Comparing this to the weight percentages of both Na_2O and Al_2O_3 in Table 3, the amount of Na_2O present relative to the Al_2O_3 content has similar percentages as that within $NaAlO_2$, indicating that $NaAlO_2$ is the occurring phase in the filter residue. The validation of this composition can be seen in Equation 4 and 5.

$$\frac{24.93}{40.89} \cdot 100 = 61\% \tag{4}$$

$$\frac{24.84}{41.45} \cdot 100 = 59.9\% \tag{5}$$

Table 3: Composition of the filtered residue in weight percentage, determined by XRF (Nugteren, 2010)

Origin	Al_2O_3	Na_2O	MgO	Fe_2O_3	SiO_2	S	CaO	MnO	ZnO	CuO
Rinsing bath	40.89	24.93	6.70	1.34	0.702	0.317	0.264	0.192	0.150	0.119
Main etch bath	41.45	24.84	4.39	1.58	0.577	0.555	0.206	0.174	0.095	0.090

In order avoid any further precipitation in the solution, the literature proposed a method to stabilize the solution as the solution could in its current composition, still form precipitation over time (Nugteren, 2010). This precipitation is dependent on the concentrations of Al_2O_3 and Na_2O. By alternating the concentrations of these elements, the stability of the solution can be achieved, where stable is defined by no formation of precipitation. The liquid stability field of a Na_2O and Al_2O_3 containing solution can be seen in Figure 6. Point 1 indicates the composition of the solution as received, reported in the literature (Nugteren, 2010). While point 2 represents a stable solution after diluting with a NaOH solution in order to lower the Al_2O_3 content.

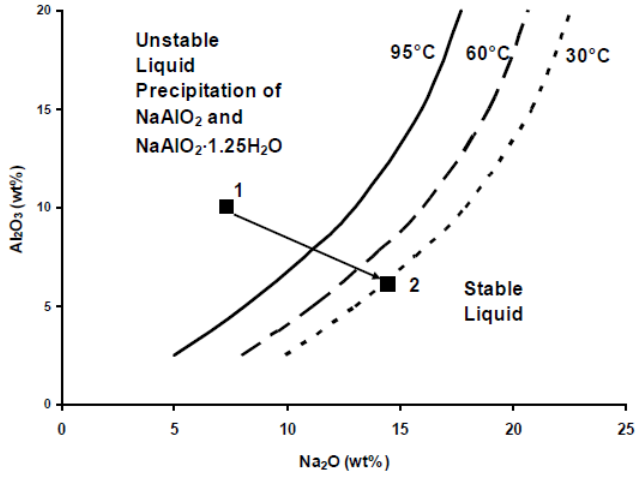

Figure 6: Liquid stability fields of solutions containing Na_2O and Al_2O_3. (Nugteren, 2010)

Similar ternary diagrams for the liquid stability of solutions containing Na_2O and Al_2O_3 are also reported in the literature, where the stability at 30°C is shown (Graham et al., 2022). The ternary diagram as a function of H_2O, Al_2O_3 and Na_2O can be seen in Figure 7.

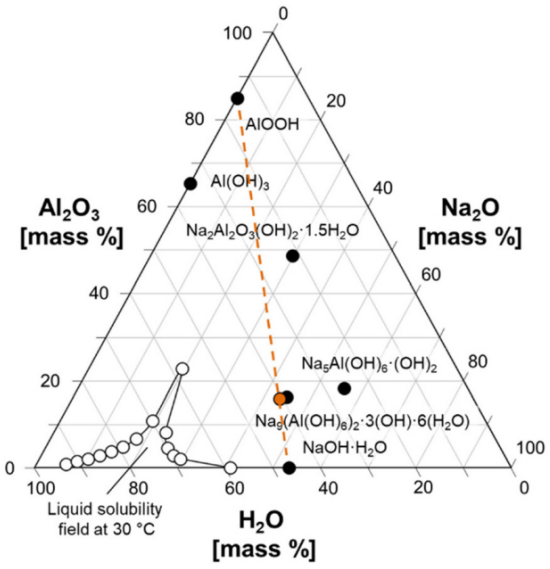

Figure 7: The range of liquid state of solutions containing Na_2O and Al_2O_3. (Graham et al., 2022)

The solubility field of the solution containing Na_2O and Al_2O_3 is plotted as white dots.

2.4 Influence aluminium on the reaction process

Aluminium is present in BFS as an oxide in the form of Al_2O_3. During the reaction the Al_2O_3 will dissolve and aluminium will be present in a dissolved state. To make comparisons in the Al_2O_3 in the precursor and the aluminium in the activator it is important to know in what form the Al_2O_3 dissolves to and in what form the aluminium is present in the activator. In the etching solution the metallic aluminium will react with hydroxide, the reaction that will take place is shown in Equation 6 (Nugteren, 2010).

$$Na^+ + OH^- + Al + 3H_2O \rightarrow Na^+ + Al(OH)_4^- + 1.5H_2 \uparrow \tag{6}$$

The concentrations of some important elements in the etching solution are shown in Table 4 (Nugteren, 2010). It can be seen that 100% of the aluminium is in the species of $Al(OH)_4^-$.

Table 4: Concentrations in the saturated etching solution (Nugteren, 2010)

Stream #	Concentrations			pH	Species		Saturated species
	Na $mol \cdot dm^{-3}$	Al $mol \cdot dm^{-3}$	free OH^- $mol \cdot dm^{-3}$		Na^+ %	$Al(OH)_4^-$ %	
1 (max)	4.33	3.71	0.63	13.8	100	100	Diaspore Böhmite Gibbsite α-$Al(OH)_3$ Al_2O_3
2 (min)	0.047	0.037	0.01	12.0	100	100	Diaspore
2 (max)	0.099	0.074	0.025	12.4	100	100	Böhmite Gibbsite

Most solid precursors contain Al_2O_3 and once in contact with the activator, Al_2O_3 dissolves into $Al(OH)_4^-$ (Liu et al., 2022). This means that Al_2O_3 dissolves into the same form as which is present in the etching solution reported in the literature (Nugteren, 2010). The presence of Al_2O_3 in the precursor is already investigated very well. As this research focuses on the impact of aluminium in the activator, the effect of the aluminium content in the AAM mixture will be evaluated so that the function and consequences of aluminium in the mixture are well known. In the section below some statements about aluminium in the mixture will be shown so later on in the research, this section could be used for guidance and to reflect on these statements.

- A study which investigated the reactivity of Metakaolin and Fly ash precursors reported that Al_2O_3 is more reactive than SiO_2 in the precursor. Al_2O_3 is released first and is earlier available for the geopolymerization compared to the SiO_2 (Marvila, de Azevedo, & Vieira, 2020).
- The formation of secondary reaction products in calcium rich precursors depends on the aluminium and magnesium content (Marvila et al., 2020).
- In alkali activated BFS, Aluminium ions (Al^{3+}) can replace the silicon ions (Si^{4+}) in the tetrahedral chain which leads to a charge which can be compensated by the positively charged alkali metal ions (Provis & Bernal, 2014).
- The replacement of Si by Al in the silicate chains, as explained in the point above, leads to cross-linking of the silicate chains (Provis & Bernal, 2014).
- In a hydroxide activated BFS system the Al only gets substituted in the bridging sites. This leads to a limitation of the Al substitution in the C-A-S-H gel, depending on degree of cross linking and the chain length(Provis & van Deventer, 2014).
- For alkali-activated BFS, a higher activator modulus could increase the incorporation of Al into the gel as more Ca that is present in the interlayer can react with present Si and therefore, the Al can take the place of the Ca in the interlayer and make new cross-links as well (Provis & van Deventer, 2014).
- SiO_2 and Al_2O_3 solubility increases with a higher pH while the solubility of Ca decreases (Provis & van Deventer, 2014).

- When the content of Al increases in calcium rich precursors, precipitation of the Al begins to occur in the C-A-S-H chains. This means that the C-A-S-H chains have more difficulty to cross-link and to become saturated and secondary Al rich phases start to form (Marvila et al., 2020).
- A molar ratio of $\frac{Si}{Al}$, equal to 1.9 of an AAM mixture gives the highest compressive strength. However, this is for mixtures based on a metakaolin precursor and activated with either NaOH or waterglass with varying activator moduli. (Duxson et al., 2005).
- A molar ratio of $\frac{Si}{Al}$, equal to 1.65 of an AAM mixture gives the highest Young's modulus. However, this is for mixtures based on a metakaolin precursor and activated with either NaOH or waterglass with varying activator moduli. (Duxson et al., 2005).
- The presence of dissolved Al in a NaOH activator leads to the shift of Si in BFS from fully tetrahedrally coordinated to become partially tetrahedrally coordinated, which dissolves faster compared to the fully tetrahedrally coordinated Si (Zuo, 2019).
- Within BFS dissolution in a NaOH activator, the dissolution of Al in the precursor is preferred over the dissolution of Si as the Al-O bonds are more easily to break than the Si-O bonds. (Zuo, 2019).

2.5 Current studies on aluminium containing activators

Even though the literature on aluminium containing is scarse, there are some papers that investigate aluminium containing activators. In all the papers a solid $NaAlO_2$ or a $NaAlO_2$ solution is considered as the activator. Even though the activator is not completely similar, the research can give good guidance and function as reference.

2.5.1 Type of activator

The type of activator that is used in the considered literature is either a solid or dissolved $NaAlO_2$. When the $NaAlO_2$ is dissolved in water before mixing, there will be an equal amount of Na and Al (in moles) present in the solution. When the $NaAlO_2$ is added as a solid into the mixture, the dissolution will be dependent on the total dissolution of the dry constituents.

Besides a pure $NaAlO_2$ activator, a solid $NaAlO_2$ combined with Na_2SiO_3 is reported in the literature in order to alter the $NaAlO_2$ content in the mixture (Chen et al., 2021). Dissolved $NaAlO_2$ is prepared by dissolving solid $NaAlO_2$ and optionally NaOH into de-mineralized water before mixing the solution with the dry ingredients (Liu, Tang, et al., 2024). In this section only the mixtures with BFS as precursor will be investigated.

2.5.2 Influence of activator on setting time

The first property that is considered, is the setting time of AAP, activated by aluminium containing activators. The Al_2O_3 content and the Na_2O content of the solid activator presented in the literature can be seen in Table 5 (Chen et al., 2021). The w/b ratio was set to 0.35 for all mixtures and BFS was used as precursor.

Table 5: Mixture details of the mixtures containing a solid activator, reported in the literature (Chen et al., 2021)

Mixture	Al_2O_3 **[wt%]**	Na_2O **[wt%]**	**BFS/b**	**w/b**
A0S10	0	5	1	0.35
A2S8	1.6	5	1	0.35
A4S6	3.2	5	1	0.35
A6S4	4.8	5	1	0.35
A8S2	6.4	5	1	0.35
A10S0	8.0	5	1	0.35

The setting times of the different solid $NaAlO_2$ - Na_2SiO_3 activators can be seen in Figure 8, where the name is indicating the amounts of $NaAlO_2$ and Na_2SiO_3. Fore example, mixture A6S4-5M indicates 60% of $NaAlO_2$ and 40% of Na_2SiO_3 with a total of 5 weight percent of Na_2O relative to the precursor.

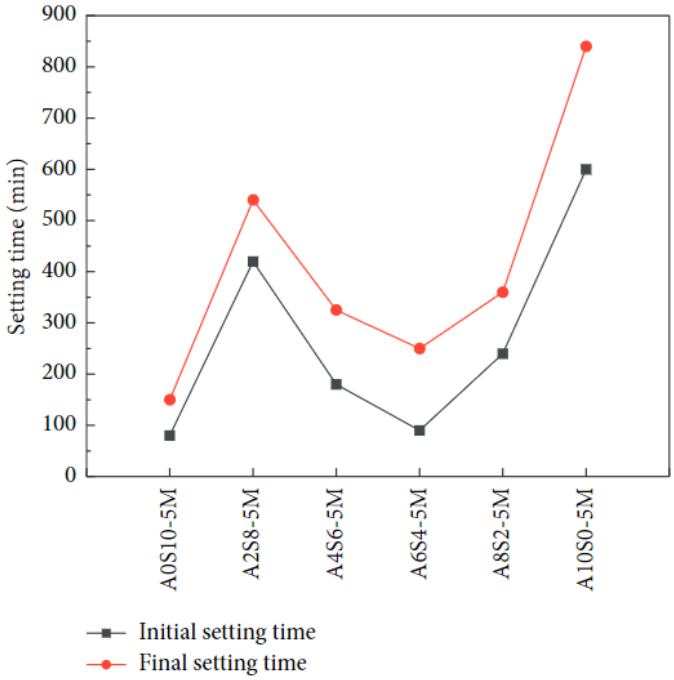

Figure 8: Setting time of different mixtures containing solid $NaAlO_2$ and Na_2SiO_3. (Chen et al., 2021)

Figure 8 shows that there is not a clear correlation between the setting time and $NaAlO_2$ dosage. The shortest setting times are achieved for the mixture without any $NaAlO_2$ and overall, the mixtures which contain $NaAlO_2$ experience an extended setting time. Between 20 and 60% of $NaAlO_2$, the setting times decrease compared to the 20% value.

It is difficult to make a direct relation between the Al content and the setting time as there is also silicates in the mixture which could also influence the setting time. The only direct result that can be obtained is that a pure Na_2SiO_3 activator sets significantly quicker compared to a $NaAlO_2$ activator.

2.5.3 Influence of activator on strength development

Various studies have reported different observations regarding strength development. In one study, strength was measured at 3, 7, and 28 days (Chen et al., 2021), while another study measured it at 7, 28, and 56 days (Liu, Tang, et al., 2024). The mixture considered in the section above was also tested on strength. Another study used a mixed precursor where bottom ash (BA) was mixed with BFS (Liu, Tang, et al., 2024). The study used a dissolved $NaAlO_2$ activator and a w/b ratio of 0.5. In sake for good comparison with this study, only the mixture without any BA will be considered as it only has BFS as precursor. The activator details of mixture BA0 can be seen in Table 6.

Table 6: Mixture details of mixture BAO reported in the literature (Liu, Tang, et al., 2024)

Mixture	Al_2O_3 **[wt%]**	Na_2O **[wt%]**	**BFS/b**	**w/b**
BA0	4.9	3	1	0.5

The mixture shown in Table 6 has a significantly lower Na_2O content compared to the mixtures shown in Table 5. The compressive strength data of the mixtures shown in Table 5 can be found in Figure 9.

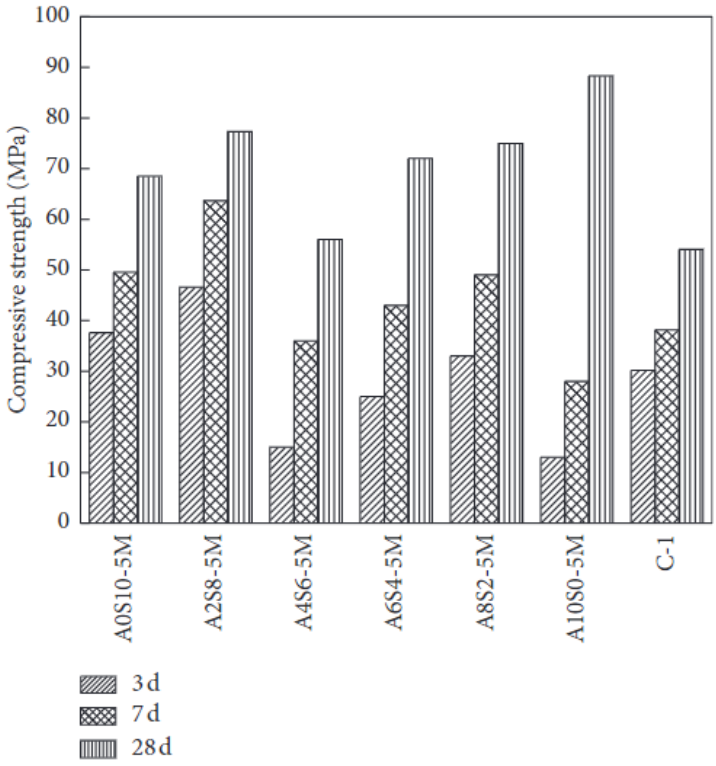

Figure 9: Compressive strength of the mixtures shown in Table 5 (Chen et al., 2021)

The mixture with the highest Al content showed the lowest 3 and 7 day strength, while it had the highest 28 day strength. A10S0 reacted very slowly in the early phase, but picked up reaction at a later stage, leading to a high 28-day strength (Chen et al., 2021). The slow reaction for mixture A10S0 was confirmed by the setting time results, shown in Section 2.5.2. The lower 3 day strength the A10S0 mixture was due to the Al^{3+} ions in the activator which initially wrap around slag particles which inhibits the slag dissolution (Chen et al., 2021). It was stated that the Al^{3+} ions promote the formation of higher cross-linked gel during the later phase of reaction (Chen et al., 2021).

The compressive strength results of the mixture shown in Table 6 are presented in Figure 10.

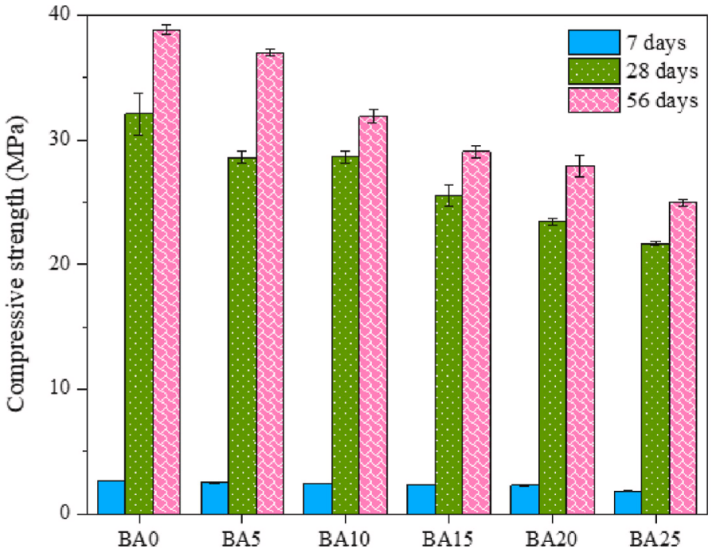

Figure 10: Compressive strength data of mixtures shown in Table 6 (Liu, Tang, et al., 2024)

Mixture BA0 showed a very low 7 day strength and a significant increase in strength between 7 and 28 days. The difference in strength between mixture BA0 In Figure 10 and A10S0 in Figure 9 can be explained by the lower content of $Na2O$ and higher water to binder ratio of mixture BA0.

The reason for the high compressive strength increase between 7 and 28 days is a drastic increase of C-(N-)A-S-H gel in the later phase of the reaction because of the re-dissolution of a metastable phase, gibbsite, into $Al(OH)_4^+$, which can then react with $Si(OH)_4$, Ca^{2+} and Na^+ into C-(N-)A-S-H, hydrotalcite and zeolites (Liu, Tang, et al., 2024).

The studies both reported that $NaAlO_2$ activated BFS mixtures experience slow early age strength development while in later stages the mixtures showed superior strength development compared to mixtures with lower or no $NaAlO_2$ content.

2.5.4 Influence of activator on reaction kinetics

The presence of dissolved Al can have an influence on the dissolution of slag which in turns influences the setting time and strength development as shown Section 2.5.2 and 2.5.3. Previous studies used isothermal calorimetry to investigate the influence of $NaAlO_2$ on the reaction kinetics of the mixture.

Several studies investigated the reaction kinetics of $NaAlO_2$ activated BFS (Liu et al., 2022; Liu, Tang, et al., 2024). The study which investigated the mixture shown in Table 6, which was also discussed in Section 2.5.3, also investigate the reaction kinetics of the mixture.

Another study which investigate the reaction kinetics of $NaAlO_2$ activated BFS, considered different contents of $NaAlO_2$. The mixtures considered in this study can be seen in Table 7. The $NaAlO_2$ is dissolved in de-mineralized water prior to mixing.

Table 7: Mixture details reported in the literature (Liu et al., 2022)

Mixture	$NaAlO_2$ **[wt%]**	$NaOH$ **[wt%]**	Na_2O **[wt%]**	**BFS/b**	**w/b**
NA2	5.288	-	2	1	0.4
NA2.5	6.610	-	2.5	1	0.4
NA3	7.933	-	3	1	0.4
NA3.5	9.255	-	3.5	1	0.4
NA4	10.577	-	4	1	0.4
REF-NH	-	5.161	4	1	0.4

The mixtures have either a $NaAlO_2$ or NaOH activator. The column 'Na_2O [wt.%]' shows the equivalent weight percentage of Na_2O to the BFS of the activator used.

The normalized heat flow and cumulative heat release of the mixtures shown in Table 7 can be seen in Figure 11.

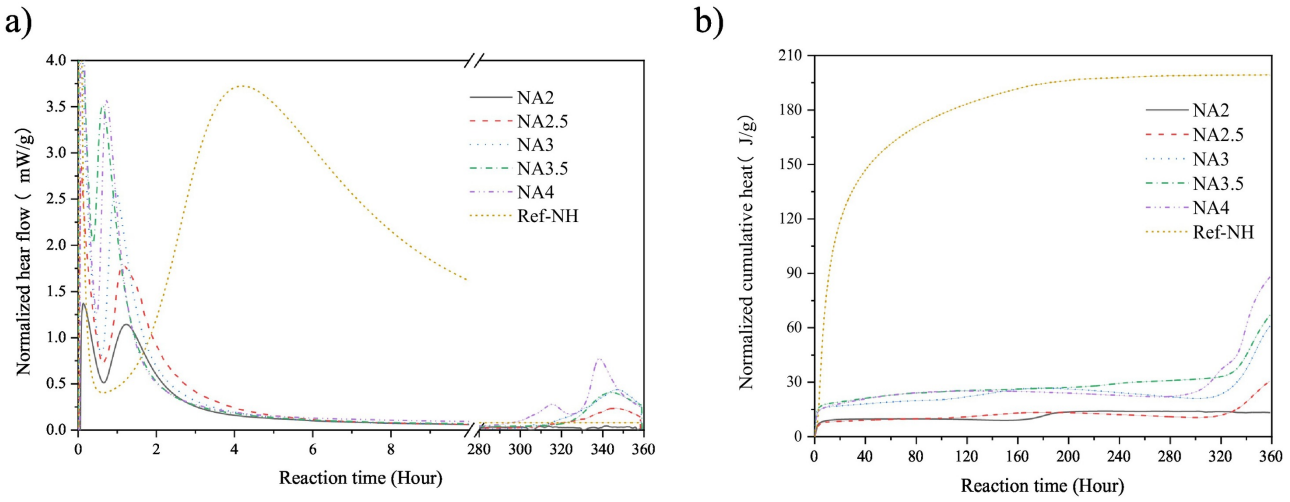

Figure 11: Reaction kinetics of the mixtures shown in Table 7 (Liu et al., 2022)

When $NaAlO_2$ is used as an activator, the graphs showed a significantly different trend compared to the reference mixture. The normalized heat flow and cumulative heat release showed that the reference mixture experienced higher peaks in the heat flow and higher cumulative heat compared to the $NaAlO_2$ activated mixtures. A higher $NaAlO_2$ content in a mixture lead to earlier and higher heat flow peaks, as to a higher cumulative heat release. The $NaAlO_2$ activated mixtures showed a total of three peaks of which two are within the first 3 hours and the last occurred around 300 hours. The first two peak occurred earlier as the $NaAlO_2$ content increased, due to the increase of Na_2O in the mixture (Liu et al., 2022). Mixture NA4 deviated from the observed trend as the first two peaks of mixture NA4 occurred after that of mixture NA3.5, implying that a higher content of Al in the activator prohibits the precursor to dissolve and thus lowering reactivity in early phase.

Another study in the literature elucidated the different reaction stages observed in the reaction kinetics (Liu, Tang, et al., 2024). In total five different stages during the reaction were identified, this being the initial dissolution (1), metastable period(2), induction period (3), acceleration/deceleration period (4) and the stable reaction period (5) (Liu, Tang, et al., 2024). The normalized heat flow, with the reaction stages identified, can be seen Figure 12.

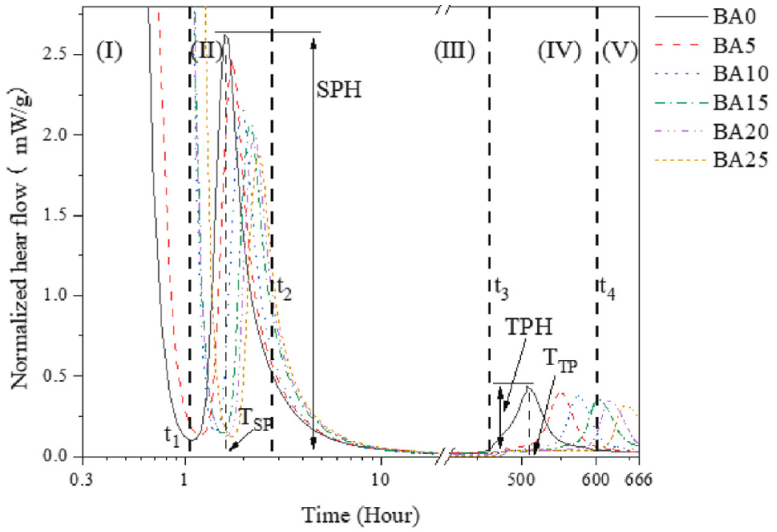

Figure 12: The different stages displayed in the calorimetry response from T. Liu. (Liu, Tang, et al., 2024)

The initial dissolution refers to the heat released within the first few hours of the reaction, corresponding to the dissolution of the precursor. It was found that the addition of bottom ash (BA) extends the duration of this phase, likely due to the lower reactivity of BA (Liu, Tang, et al., 2024).

The second stage has been attributed to the metastable period, which occurred between 1 and 10 hours into the reaction. During this phase, metastable phases such as gibbsite formed, contributing to a second heat peak. Gibbsite is later incorporated into primary and secondary reaction products, such as C-(N-)A-S-H and zeolites. This metastable period is considered unique to this type of activator (Liu, Tang, et al., 2024).

The third stage, described as the induction period, lasted more than 462 hours. This extended duration is attributed to the high concentration of aqueous aluminium in the pore solution, which inhibited the dissolution of SiO_2 from the BFS. As a result, the geopolymerization process was delayed. Additionally, a gel formed around the unreacted particles, preventing further contact with the pore solution. This phenomenon is not unique to this activator but is common in most cementitious systems (Liu, Tang, et al., 2024).

The acceleration/deceleration period followed the induction phase, during which the third reaction peak occurred. Over time, the barrier of reaction products surrounding the grains either dissolved or became permeable, allowing new reactions to take place and generating additional heat. Once all accessible anhydrous phases have been reached by the aqueous solution, the deceleration phase began, where the reaction rate and heat release decreased. Finally, the stable period set in, during which reactions continued at a very slow rate, resulting in negligible heat release (Liu, Tang, et al., 2024).

2.5.5 Influence of activator on pore solution

In the literature, the pore solution chemistry of $NaAlO_2$ activated BFS was investigated as well (Liu et al., 2022). The considered mixtures are the same as which are shown in Table 7. By performing a cold water extraction and using those solutions in ICP and IC, the ion concentrations could be determined. The concentrations that were measured are Al, Ca, Si, Mg, Na and OH. The OH concentrations can be seen in Figure 13.

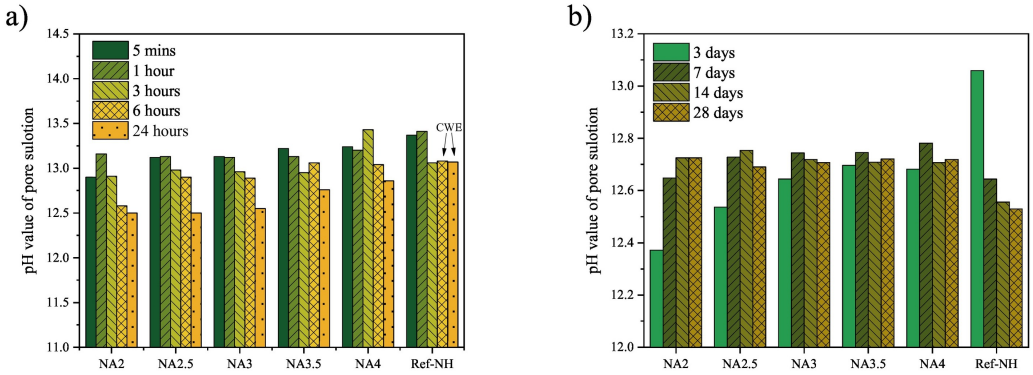

Figure 13: The concentrations of hydroxide over time per mixture from the paper of T. Liu. (Liu et al., 2022)

It is known that OH ion concentrations in geopolymers decrease with curing time, as these ions are consumed during precursor dissolution and the reaction process itself (Paudel, Yang, & Gao, 2020). Figure 13 showed that the pH and therefore the hydroxide concentration decreased for all mixtures in the early stages, correlating with the dissolution process. However, this decrease was less significant for the $NaAlO_2$ activated mixtures compared to the reference mixture. This is attributed to the fact that $NaAlO_2$ is formed between a weak acid and a strong base, allowing it to sustain hydroxide hydrolysis, thereby providing a buffering effect on the hydroxide concentration (Liu et al., 2022).

In later stages of the reaction, the pH of the pore solution of mixture REF-NH continued to decline, whereas for the $NaAlO_2$ activated mixtures, the pH began to rise and remained stable over time. This is also due to the buffering effect of the $NaAlO_2$ activator (Liu et al., 2022).

The concentrations of the elements Al, Si, Na, Ca and Mg measured with ICP or IC can be seen in Figure 14.

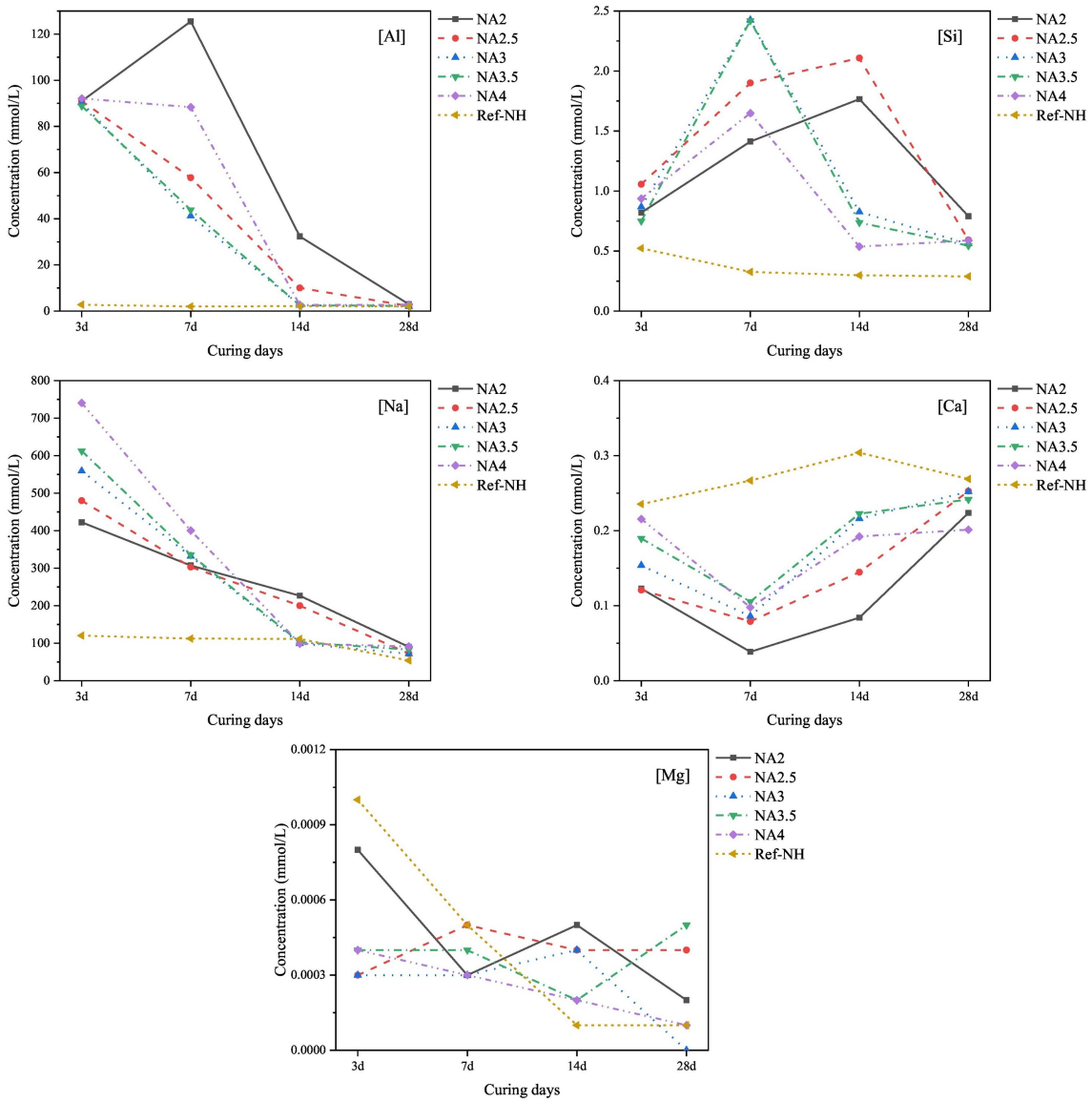

Figure 14: Concentrations of ions in the pore solution for each different mixture. (Liu et al., 2022)

The concentrations of Mg and Ca in the pore solution are negligible compared to other elements. This suggests that when Mg and Ca dissolve, they react almost immediately with other elements to form reaction products, maintaining consistently low concentrations of these ions.

The concentrations of Al, varied significantly during the curing process in $NaAlO_2$ activated mixtures, whereas in the reference mixture, they remained relatively constant over time. Notably, NA2 was the only mixture where an increase in Al concentration was observed. This increase is attributed to the alkaline environment being strong enough to break Al-O bonds, but not sufficient to promote the interaction between alumina and silica species, which typically occurs at a pH of approximately 12.7. Between 3 and 7 days, the pH is below this threshold, resulting in an accumulation of Al. In contrast, the other mixtures exhibited higher alkalinity at this stage, allowing for the consumption of Al ions, leading to a decreasing trend in Al concentrations. Finally, at 28 days, Al concentrations were similar across all mixtures (Liu et al., 2022).

The concentrations of Si first increased and then declined with the curing time. The highest concentration of Si was reached at different curing times. As Si concentrations depend on the BFS dissolution, the time to the peak correlated with the rate of dissolution, which was faster in mixtures with higher $NaAlO_2$ content and thus higher alkalinity, promoting precursor dissolution. The subsequent decline in Si concentration was due to its consumption in forming reaction products. The reference mixture showed a slight decline from 3 days onward, indicating that most of the Si dissolution and consumption occurred before this time (Liu et al., 2022).

Na concentrations exhibited a similar trend across all $NaAlO_2$ activated mixtures, with a general decrease over time. Higher Na_2O concentrations are observed in mixtures with greater $NaAlO_2$ content. Compared to the NaOH activated mixture, $NaAlO_2$ activated mixtures exhibited delayed activation, as most of the Na in the reference mixture was consumed before 3 days, while the decrease of the Na in the $NaAlO_2$ activated mixtures happened after 3 days. This delayed activation is corroborated by the Si and Al concentrations, which also start to decrease later than in the reference mixture (Liu et al., 2022).

Ca concentrations in the $NaAlO_2$ activated mixtures displayed a decreasing trend till 7 days after which the concentration began to rise. Whereas the Ca concentration in NaOH activated mixture showed an increase till 14 days and decreased after. The initial decline in Ca concentration in the $NaAlO_2$ mixtures was due to the high availability of Si and Al in the first 7 to 14 days, promoting Ca consumption. Additionally, the increasing pH in $NaAlO_2$ activated mixtures after 3 days slowed the dissolution rate of Ca, reducing its presence in the pore solution. In the NaOH activated mixture, activation primarily occurred within the first 3 days, as indicated by the measured concentrations. After this point, with lower Al and Si concentrations, the dissolved Ca was not fully consumed and instead accumulates in the pore solution (Liu et al., 2022).

The Mg concentration was insignificant for all mixtures and was therefore not be discussed in detail. The only observable trend was that mixtures NA4 and REF-NH showed higher initial concentrations at 3 days due to elevated alkalinity.

2.6 GEMS modelling

Gibbs Energy Minimization Selektor (GEMS) is a thermodynamic software program which is already used in previous literature to analyze alkali activated BFS (Myers et al., 2015). A thermodynamic database can be used to predict which phases form based on the equilibrium between the solid reaction products and pore solution (Lothenbach, 2010).

Different thermodynamic databases are present and the selection of these databases can be dependent on the project. Additional databases to the default software are CNASH_ss and MA-OH-LDH_ss. CNASH_ss is an additional database which accounts for the Al and Na incorporation in CSH like phases (Myers, Bernal, & Provis, 2014). MA-OH-LDH_ss contains three end members with different Mg/Al ratios which match the known composition of the solid (Myers et al., 2015).

The influence of different input parameters in the mixture can be investigated using the software. Besides that, the evolution over degree of reaction of reaction products can also be investigated. In the literature, the influence of different mineral content in the precursors is investigated as is the evolution over degree of reaction. The many possibilities the software offers, gives great potential for this research. An example of the possibilities using GEMS is shown in Figure 15, where the evolution of reaction products over degree of reaction and the influence of the wt.% of Al_2O_3 in the slag is shown.

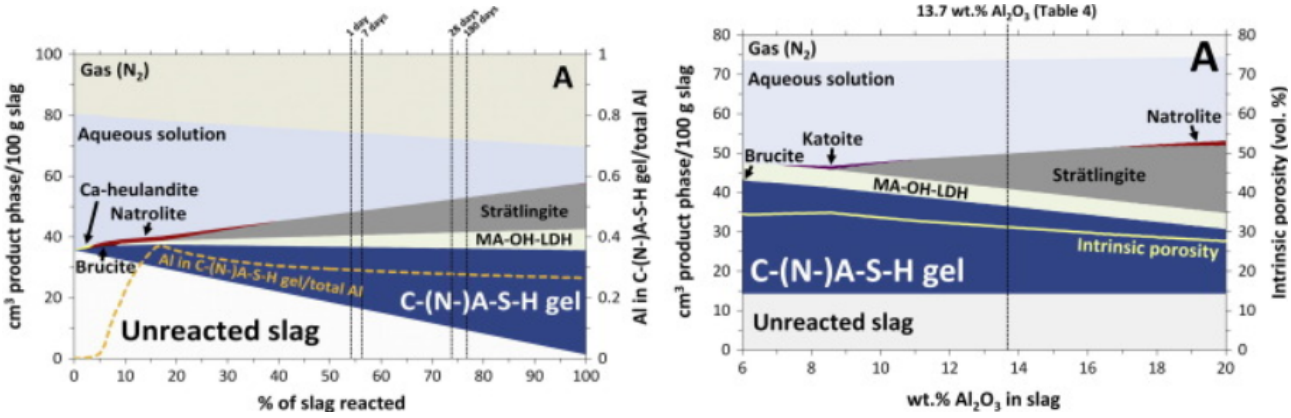

Figure 15: Formation of reaction products over degree of reaction and the influence of the Al_2O_3 content in slag (Myers et al., 2015)

2.7 Summary

The literature review examined the use of BFS as a precursor and NaOH as a traditional activator, which will serve as a reference in this research. Studies on the composition of aluminium etching solutions highlight their viability as alternative activators. Current research on $NaAlO_2$ activators further supports the feasibility of using aluminium-rich solutions in alkali-activated systems. However, minimal research has specifically addressed the use of aluminium etching solutions as activators, and no existing thermodynamic modeling has been conducted to predict reaction behaviors for activators containing aluminium. This gap leaves reaction mechanisms, product stability, and performance of systems activated by the aluminium etching solution largely unexplored, underscoring the need for further investigation into these complex and potentially high-performance formulations.

3 Characterization of the aluminium etching solution

The anodizing of aluminium is an important technique in the aluminium industry, particularly for enhancing the surface properties of aluminium profiles. Within this process, etching plays a critical role, involving submersion of aluminium profiles in a NaOH solution with additives to manage precipitate formation. This etching process dissolves aluminium into the solution, which, once saturated, is replenished to maintain effectiveness.

To use aluminium etching solutions as alkali activators, it is essential to understand their chemical composition and stability. By determining the composition, mixture designs can be formulated accordingly. This chapter aims to characterize the aluminium etching solution and assess its stability to support accurate modeling and mixture design in subsequent stages.

3.1 Method

Samples of the saturated etching solution were obtained from the APT Extrusions factory in Roermond. Nine batches were collected, each representing the solution discarded during a single workweek. Additionally, a larger sample, denoted as batch J.C., was collected from a jerry can, which had been stored for a duration of over a year. The 9 batches which were collected besides J.C., are denoted by the date of replenishing, being: 10-1, 17-1, 25-1, 31-1, 29-2, 7-3, 12-3, 19-3 and 22-3.

The solution is discarded by transferring the saturated solution into a storage vessel once it is no longer reactive with aluminium, and this vessel is emptied weekly and processed by a waste management company. The pH in the storage vessel is kept equivalent to a 25% NaOH solution. Oversaturation in the vessel leads to precipitation, so the initial step involves separating the solids from the solution through filtration.

The filtration process was performed using Whatman GF/A grade filters with a pore size of 1.6 μm. The setup included a filtration Erlenmeyer, funnel, and a vacuum pump to facilitate the passage of the viscous fluid through the filter paper. Afterwards, the clear solution was transferred to new storage bottles.

To determine the chemical composition of the aluminium etching solution, Inductively Coupled Plasma - Optical Emission Spectrometry (ICP-OES) was employed. The samples were diluted with nitric acid to prepare them for ICP-OES analysis. The concentrations of Na, Al, Si, Mg, P, S and Zn were measured.

Since the OH concentration could not be determined using ICP-OES, titration was performed. Hydrochloric acid (0.1 mol/L) served as the titrant, with phenolphthalein as the pH indicator, marking a neutral point at pH 7. A 0.2 mL sample of the solution was diluted with de-mineralized water before titration. The titration was carried out until the solution turned colorless, and the volume of hydrochloric acid added was recorded. Each sample was titrated twice to ensure accuracy and minimize potential errors. The OH concentration was then calculated using Equation 7.

$$[OH^-] = 0.1 * \frac{V_t}{V_s} \tag{7}$$

Where:

- V_t, the titrated volume
- V_s, the volume of the aluminium etching solution.

3.2 Results and discussion

The concentrations of Na, Al, Si, S, Mg and Zn, measured by ICP-OES are shwon in Table 8.

Table 8: Concentrations of Na, Al, Si, P, S, Mg, and Zn measured by ICP-OES, expressed in mg/L

	Na	**Al**	**Si**	**P**	**S**	**Mg**	**Zn**
10-1	241,250	75,345	434	<50	<200	<4	6.4
17-1	260,950	84,700	381	<50	<200	5.3	7.4
25-1	243,450	63,560	311	<50	<200	<4	6.6
31-1	261,500	47,830	107	<50	<200	<4	6.7
29-2	216,838	79,824	392	n.m	53	0.62	5.6
7-3	244,293	71,578	353	n.m	<50	<0.5	7.0
12-3	246,050	72,775	367	n.m	<50	0.73	6.3
19-3	258,970	77,634	386	n.m	<50	0.50	6.5
22-3	191,615	78,109	403	n.m	102	0.90	5.1
J.C.	164,160	59,261	365	n.m	103	3.2	2.0

Table 8 shows that the magnitude of the elemental concentration varied significantly. Na, Al and Si were measured in significant quantities and are thus included in the analysis. However, the concentrations of P, S, Mg and Zn are negligible.

The OH concentration, determined by titration and expressed in moles per liter is presented in Table 9. The concentration of Na, Al and Si can also be expressed in mole per liter and are presented together with the titration results in Table 9.

Table 9: Concentration of OH measured by titration and Na, Al and Si concentrations expressed in mol/L

	OH	**Na**	**Al**	**Si**
10-1	10.50	10.49	2.79	0.02
17-1	11.06	11.35	3.14	0.01
25-1	10.16	10.59	2.36	0.01
31-1	10.94	11.37	1.77	0.00
29-2	9.52	9.43	2.96	0.01
7-3	10.94	10.63	2.65	0.01
12-3	10.44	10.70	2.70	0.01
19-3	11.17	11.26	2.88	0.01
22-3	8.40	8.33	2.90	0.01
J.C.	7.33	7.14	2.20	0.01

Table 9 shows that the main composition of the etching solution is NaOH into dissolved form as the molar concentrations of Na and OH are almost identical. The presence of Al indicates that the metallic Al reacted with the solution and dissolved into the solution.

The concentrations of Na, Al, Si and OH are transformed in equivalent oxide concentrations with unit g/kg, presented in Figure 16. The X-axis in Figure 16 shows the names of the batches, presented earlier in this chapter. In addition to the oxide concentrations, a new parameter, the aluminium modulus (M_a), the OH concentrations and the density of the batches are introduced. For conventional sodium silicate activators, the activator modulus, defined by the molar ratio of SiO_2 to Na_2O, is used as a design parameter. Similarly, an aluminium modulus defines the amount of Al_2O_3 present in the activator relative to Na_2O, and is expressed as the molar ratio of Al_2O_3 to Na_2O ($M_a = \frac{Al_2O_3}{Na_2O}$).

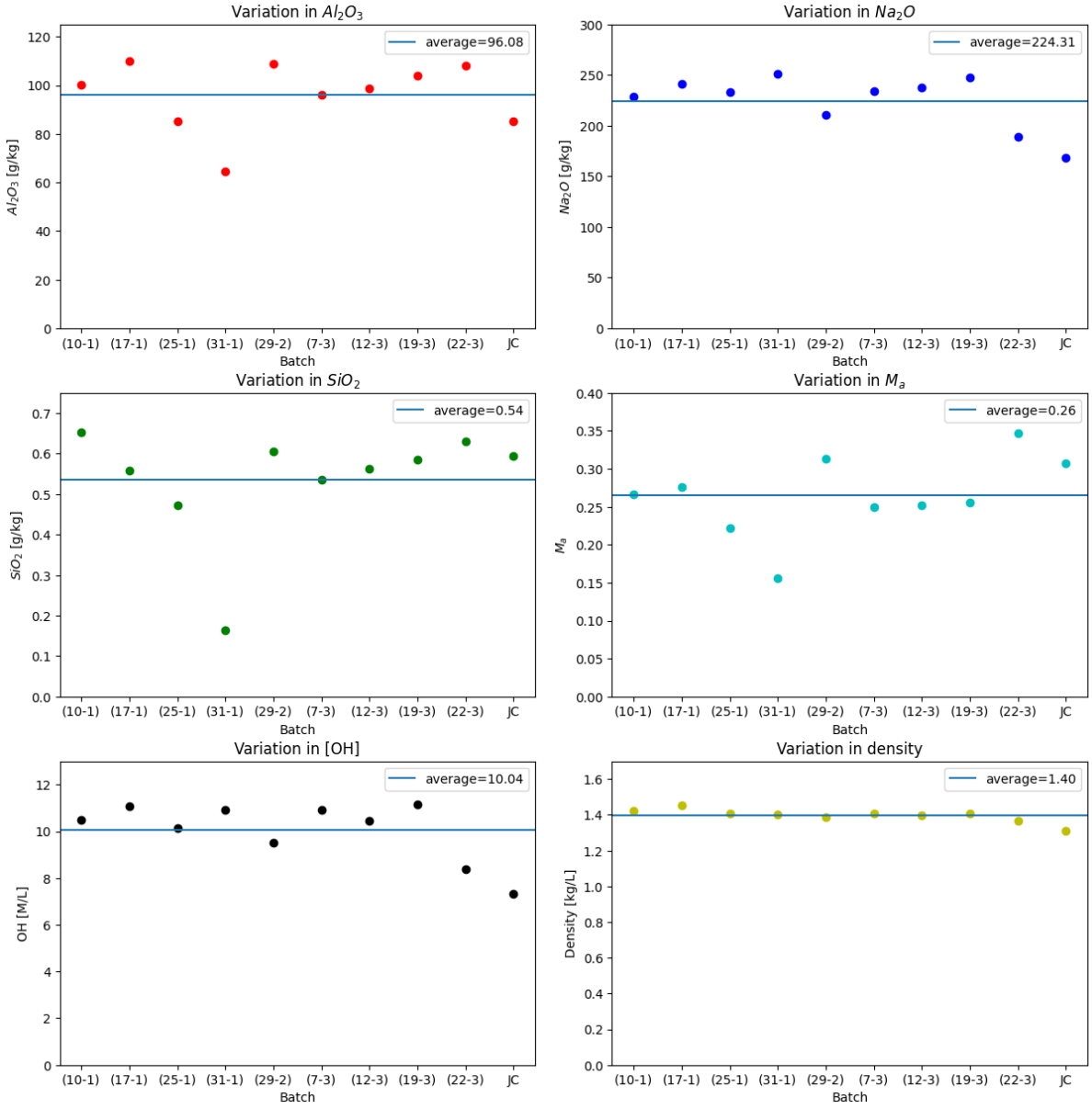

Figure 16: Characterization of the received aluminium etching solutions

From the analysis of Figure 16, several conclusions can be drawn. Notably, the Al_2O_3 and SiO_2 content in batch 31-1 is significantly lower than the average. However, batch 31-1 exhibits the highest Na_2O content among all the batches. This discrepancy suggests that the solution may have been replaced before reaching saturation, as the lower aluminium content and higher Na content indicate that some reactivity may still remain.

In addition to batch 31-1, batches 22-3 and J.C. show deviations compared to the other batches, particularly in Na_2O content, OH concentration, and density. As the Na_2O content and OH concentration are correlated, it makes sense that these both concentrations are lower. It is worth noting that the M_a values for these batches do not significantly differ from the average.

The observed deviations in batches 22-3 and J.C. may also be attributed to the sample collection method. As shown in Figure 17, Na and OH concentrations increase with rising density. If these batches were collected from the upper part of the storage tanks, where the liquid has a lower density compared to the bottom, it could explain the lower concentrations of Na and OH in these samples. The relation between the Na and OH concentration and density can be seen in Figure 17a. The relation between the Al_2O_3 content and density is shown in Figure 17b and the relation between Al_2O_3 content and OH concentration is presented in Figure 17c

Figure 17b shows that the Al_2O_3 content remains relatively stable over varying density, while Figure 17c shows

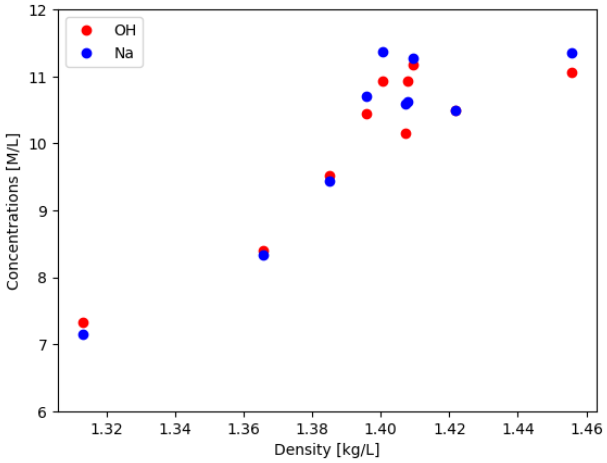

(a) Relation between concentrations OH, Na & density

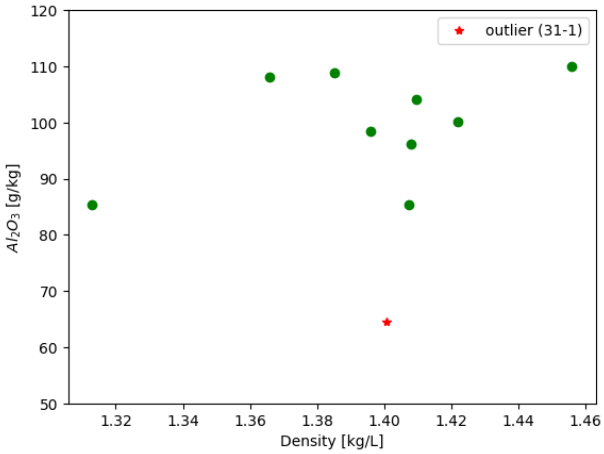

(b) Relation between Al_2O_3 content & density

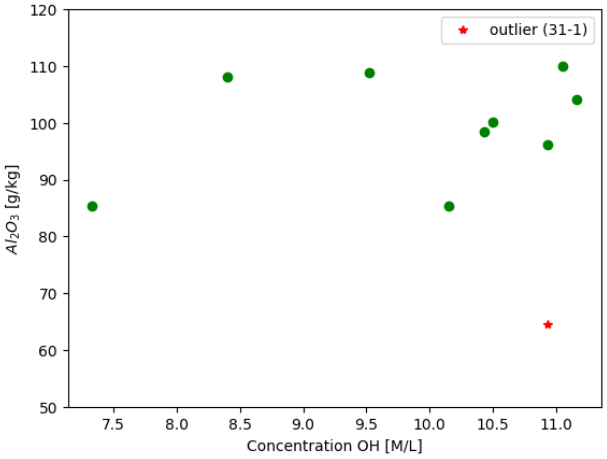

(c) Relation between concentration OH & Al_2O_3 content

Figure 17: Relations between different properties of the etching solution

that the Al_2O_3 content remains relatively stable over the OH concentration. However, there appears to be a slight increase in Al_2O_3 content as both density and OH concentration rise.

It is decided that the aluminium modulus M_a, defined as the ratio of Al_2O_3 to Na_2O, would be the main property to asses the stability of the solution. This ratio serves as a useful guide for mixture design, ensuring that even if the absolute quantities of Na_2O and Al_2O_3 vary, the relative proportion between them remains consistent. It should be noted that in this case the oxide equivalents are used, but in reality only ions are present in the solution.

The deviating value of M_a compared to the other batches can be observed in the plot shown in Figure 16. As mentioned before there is a suspicion that this batch is replenished before reaching saturation. Therefore, batch 31-1 is considered as an outlier and the coefficient of variation parameters were checked when excluding 31-1. The COV of the M_a, Na_2O content, Al_2O_3 content and SiO_2 content in the solutions is shown in Table 10.

Table 10: COV of parameters of the aluminium etching solution, excluding batch 31-1

Parameter	**COV** [%]
M_a [-]	13.3
Na_2O [g/kg]	11.3
Al_2O_3 [g/kg]	8.9
SiO_2 [g/kg]	8.7

Although the concentrations in the etching solution are relatively consistent across batches, some variation is evident. This variation may be attributed to factors such as the volume of aluminium product exposed to

the etching solution and the amount of complexing agents added, which can elevate Al and Si concentrations. Additionally, discussions with APT indicated that the collection method may contribute to this variance, as a clean flow of solution could only be obtained after precipitates were drained. The first four batches (10-1, 17-1, 25-1, and 31-1) were collected before the flow was cleared of most precipitates, resulting in higher levels of precipitate within these samples.

As indicated by batch J.C., storage duration may influence concentrations, as prolonged storage allows additional precipitation, potentially reducing solute concentrations. This observation suggests that the batches might converge to the concentration profile of J.C. over time, as equilibrium within the solution could be achieved. During this study, it was noted that after filtration and storage for several weeks, new precipitates formed, likely leading to lower Na and Al concentrations. This precipitate is most likely $NaAlO_2$, as reported in the literature (Nugteren, 2010). The observed precipitate after filtration and storage is shown in Figure 18.

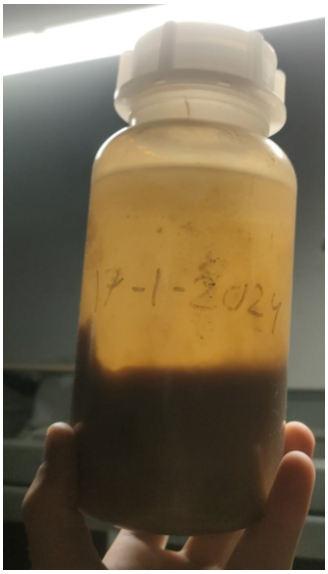

Figure 18: Observed precipitate after filtration and weeks of storage

The literature review revealed that by increasing the Na_2O content, precipitation could be prevented, shown by Figure 6 and 7.

3.3 Conclusions

- In the characterization, it was established that Na, Al, and Si were the only elements present at significant concentrations in the etching solution, with minimal variation observed in their oxide-equivalent concentrations across batches. This consistency supports reliable formulation in later mixture designs. Additionally, a new design parameter, the aluminium modulus (M_a), was introduced to aid in mixture formulation, and it exhibited minimal variation across the batches, confirming its suitability as a stable reference value. Batch 31-1 was excluded from the data due to significant deviations.
- Some variation in concentration was noted, likely influenced by differences in product exposure to the etching solution, the addition of complexing agents, and procedural aspects such as the collection process. For instance, the initial four batches collected before removing precipitates from the flow contained more particulates, which may have impacted concentration consistency.
- The stability study further revealed that prolonged storage, as observed in batch J.C., could lead to additional precipitation and lower concentrations over time, suggesting that other batches may eventually stabilize to J.C.'s concentration profile as equilibrium is achieved. To achieve stability, it is recommended to either store the samples for a significant duration to let precipitation occur over time or to increase the Na_2O content in the solution in order to prevent the precipitation.
- Considering these findings, batch J.C. was selected for the mixture design, as it is the most readily available and its M_a value aligns well with the batch average.

4 Thermodynamic modelling

Thermodynamic modelling is a computational technique employed to predict the formation of reaction products based on specified input parameters. By analyzing the effects of these parameters, researchers can obtain valuable insights to optimize mixture designs. The literature review highlighted the potential of thermodynamic modelling to evaluate how various mixture designs influence the formation of reaction products over time.

The composition of the aluminium etching solution, as determined in Chapter 3, serves as a key input for this modelling. This chapter aims to explore the impact of adding a specific amount of aluminium etching solution on the alkali activation of blast furnace slag (BFS). To perform the thermodynamic analysis, Gibbs Energy Minimization Selektor (GEM-Selektor V.3) is utilized, as it is the most widely adopted software in the literature for similar applications.

4.1 Materials and method

In this research, ground granulated blast furnace slag is used as the precursor, with its chemical composition consistent with that used in prior studies at Delft University of Technology. The BFS has a density of 2.97 g/cm^3, and this composition serves as the input for the modelling. Additionally, the aluminium etching solution characterized in Chapter 3 is used as input for the activator in this section. The chemical composition of the BFS used at Delft University of Technology is presented in Table 11.

Table 11: Chemical composition of the BFS used in this research (Zuo, 2019)

Oxide	SiO_2	CaO	Al_2O_3	MgO	Fe_2O_3	SO_3	K_2O	TiO_2	$L.I.$
wt.%	32.91	40.96	11.85	9.23	0.46	1.61	0.33	1.00	1.15

To investigate the influence of the aluminium etching solution as activator for alkali activated slag, analyses were performed using GEMS. This software accesses data from various material databases, including properties such as molar volume, molar mass, Gibbs energy of formation, entropy, enthalpy, and heat capacity. The CEMDATA07 database, which includes relevant data for alkali-activated materials (AAMs), were used, along with CNASH_ss and MA-OH-LDH_ss databases, both of which include phases commonly present in AAMs. The extended Debye-Huckel equation is applied to calculate ion activity coefficients, as supported by previous studies (Myers et al., 2015; Zuo, 2019; Myers, Bernal, & Provis, 2017), which showed that the modelling result following this approach agrees well with the experimental results.

To improve accuracy, some phases were deactivated to prevent unwanted formations, following approaches in the literature (Zuo, 2019). Model validation involves using inputs from prior studies. When the output aligns, the model is deemed valid. It is important to note that the model assumes complete reaction of the input, leading to a reaction degree of 100%. In order to account for the unreacted part of the precursor, a percentage of the mixture precursor should be presented to the model and the unreacted part should be visualized in the results.

This modelling approach investigated the influence of Al_2O_3 weight percentage in the activator relative to the precursor on reaction products at a 70% reaction degree. The simulations used 100 grams of BFS as a precursor, analyzing the effect of Al_2O_3 content in the activator on:

- Formation of reaction products dependent on wt.% of Al_2O_3 in the activator.
- Volume percent of the reaction products dependent on wt.% Al_2O_3 in the activator.
- Composition of the pore solution dependent on wt.% Al_2O_3 in the activator.
- Composition of the main reaction product C-(N-)A-S-H dependent on wt.% Al_2O_3 in the activator.

The results can be used to design mixtures for further analysis, focusing on the formation of reaction products at various reaction stages.

4.2 Influence of activator composition on the reaction products

In order to investigate the influence of the activator composition, two different parameters were investigated, this being the Al_2O_3 and Na_2O content. As the Na_2O content in an activator has been researched in detail in the literature, this research focuses on the Al_2O_3 content. Three levels of Na_2O content were assumed and based on the composition of batch J.C. a range of corresponding possible Al_2O_3 content can be evaluated for all mixtures. The Al_2O_3 range increases with higher Na_2O content, as more Al etching solution, and consequently Al_2O_3, is introduced into the mixture. The mixtures which were investigated are presented in Table 12, with Al_2O_3 content shown as a variable range.

Table 12: Mixture designs with the Na_2O and Al_2O_3 present in the activator.

Sample	Na_2O [g]	BFS [g]	$water$ **[g]**	Al_2O_3 [g]
N4Ax	4	100	40	0 - 2.2
N6Ax	6	100	40	0 - 3.2
N8Ax	8	100	40	0 - 4.2

Mixture N4Ax is investigated in Section 4.2.1, mixture N6Ax in Section 4.2.2 and mixture N8Ax in Section 4.2.3, presented in the follow-up sections

4.2.1 Mixtures with 4 wt.% Na_2O

This section examines the impact of Al_2O_3 content in the activator, on the formation of reaction products for a mixture containing 4 wt.% of Na_2O. The X-axis displays the weight percentage of Al_2O_3 relative to BFS, while the corresponding reaction products are shown in volume [cm^3/100 g BFS]. The reaction products over Al_2O_3 content can be seen in Figure 19. The degree of reaction (DoR) across all plots is set to 70%.

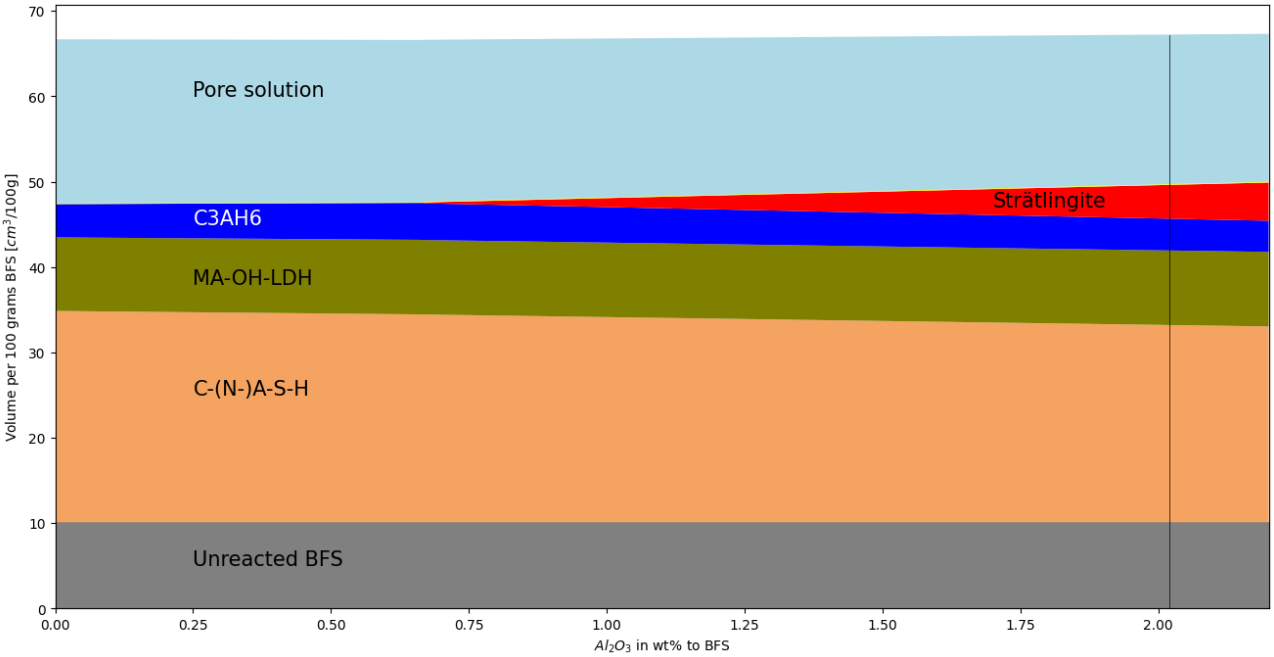

Figure 19: Volume of reaction products formed per 100 grams of BFS as a function of weight percent Al_2O_3 (DoR=70%).

The Al_2O_3 content in the activator ranges from 0 wt.%, representing a conventional NaOH activator, to 2.2 wt.%. Based on the composition of batch J.C., the highest possible Al_2O_3 content in an activator with 4 wt.% of Na_2O is equivalent to 2.02 wt.% Al_2O_3. This means that Figure 19 exceeds the highest possible content of Al_2O_3 in the activator. The highest amount of Al_2O_3 in the activator is represented by the black line in Figure 19.

Figure 19 shows that the volume of the primary reaction product, C-(N-)A-S-H gel, decreases as the Al_2O_3 content in the activator increases. Conversely, the volume of hydrotalcite-like phases (MA-OH-LDH) remains relatively stable, showing only a slight increase with higher Al_2O_3 content. At an Al_2O_3 content of 0.66 wt.%, strätlingite begins to form, and its volume continues to increase with rising Al_2O_3 content. Additionally, the total mixture volume decreases linearly from 66.67 cm^3 at 0 wt.% Al_2O_3 to 66.60 cm^3 at 0.66 wt.%, before rising to 67.32 cm^3 at 2.2 wt.%.

Given these changes in volume, the volume of the reaction products should be normalized to the total volume before further investigation. This approach could avoid a slight bias toward mixtures with higher Al_2O_3 content, which exhibit larger total volumes.

To further investigate the influence of Al_2O_3 content in the activator on the primary reaction products, being C-(N-)A-S-H gels, hydrotalcite phases (MgAl-OH-LDH), and katoite (C3AH6). The normalized volume of these phases are plotted against the Al_2O_3 content in the activator. The formation of the main reaction products' volume normalized to the total volume is illustrated in Figure 20. The red line illustrates a mixture with an activator in which the aluminium etching solution is diluted solely with water to achieve a concentration of 4 wt.% Na_2O. In contrast, the black line represents a mixture where the solution is diluted with a NaOH solution, also maintaining 4 wt.% Na_2O, but resulting in a reduced Al_2O_3 content.

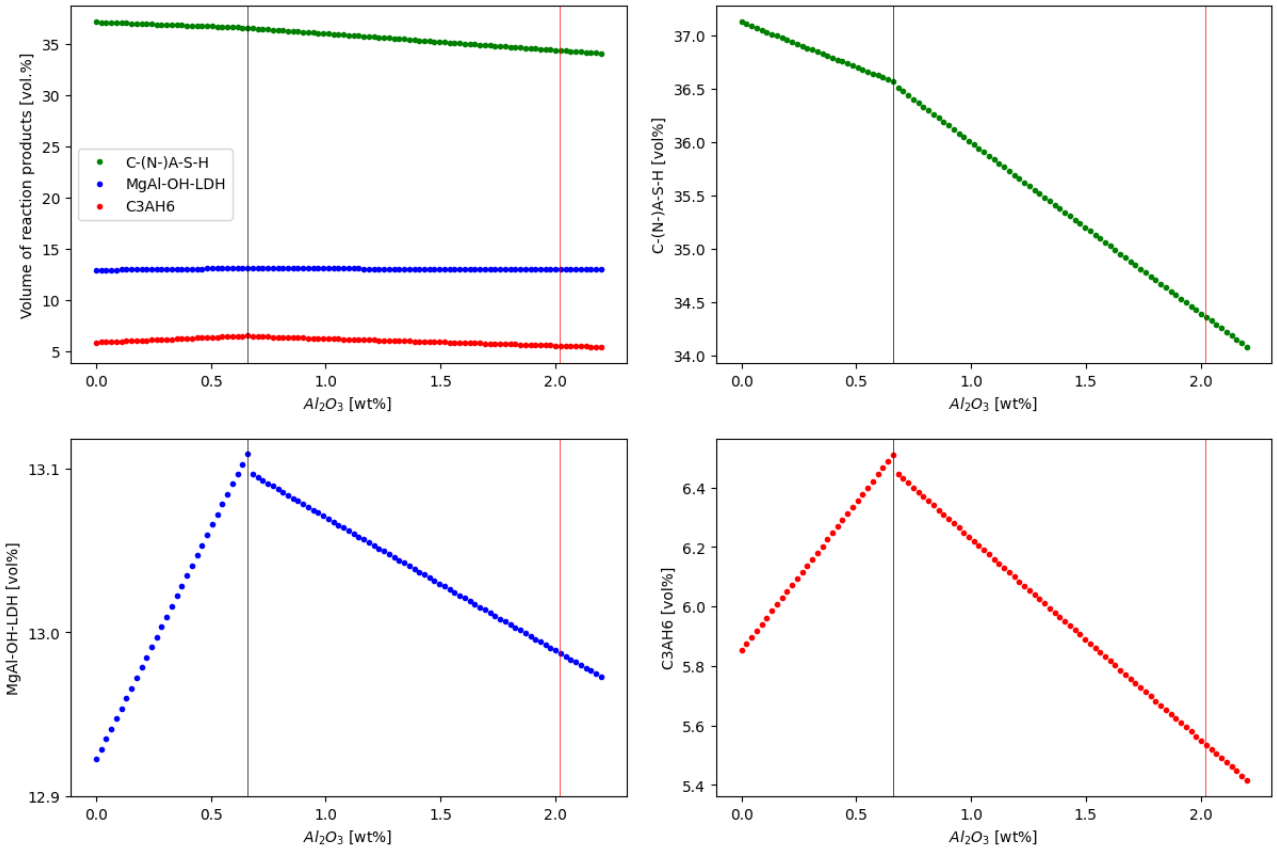

Figure 20: Volume percentage of the main reaction products as a function of Al_2O_3 content. Black line: 0.66 wt.%, red line 2.02 wt.%.

At the black line, the C-(N-)A-S-H gel and hydrotalcite phases exhibit maximum gains compared to the red line, alongside an increase in katoite. Diluting the solution to 0.66 wt.% Al_2O_3 surpasses the steepest increase in C-(N-)A-S-H gel volume, indicating optimal returns from the dilution process in terms of C-(N-)A-S-H gel formation, which is the most desirable reaction product. It is also evident that the maximum C-(N-)A-S-H volume is achieved at 0 wt.% Al_2O_3, a condition impossible to reach through dilution alone.

At the point where the normalized volume of C-(N-)A-S-H gel reaches the first change of slope, both hydrotalcite and katoite reach their maximum standardized volume. However, the variance on the y-axis scale for hydrotalcite is significantly smaller than that for C-(N-)A-S-H and katoite, raising questions about the actual impact of hydrotalcite variations on the overall mixture performance. It should be noted that the decrease in volume percentages of all phases after the peaks is directly linked to the formation of strätlingite at 0.66 wt.% Al_2O_3.

The influence of the Al_2O_3 content on the Al, Ca, Na, Mg and Si content in the pore solution is shown in Figure 21.

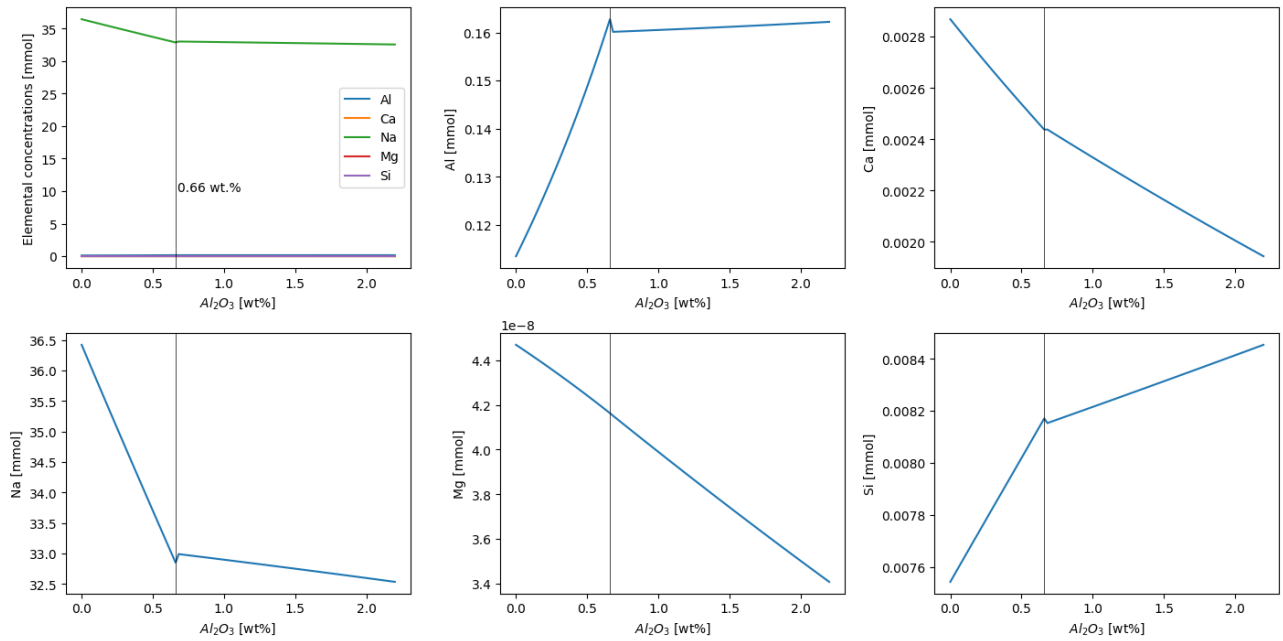

Figure 21: Elemental composition of the pore solution as a function of the Al_2O_3 content.

The top left plot shows all elements together, revealing that Na is the most significant element present in the pore solution. At the critical point of 0.66 wt.% Al_2O_3, indicated by the black line, the rate of Na concentration decline decelerates compared to earlier stages. As the Al_2O_3 content in the activator increases, Na incorporation into the C-(N-)A-S-H gel also rises, since the additional Al allows more extensive reaction with Ca and Si to form C-(N-)A-S-H gel. However, once the Al_2O_3 content surpasses 0.66 wt.%, strätlingite begins to form, consuming elements in the pore solution except for Na, as it is not incorporated into strätlingite. Consequently, Na concentrations remain nearly constant beyond this point.

While the concentrations of other elements are negligible, some trends become visible when zooming in on the data. For all graphs, a distinct break point can be observed, corresponding to the formation of strätlingite, with the exception of magnesium (Mg). Magnesium exhibits only a slight change in slope, likely due to the small variation in hydrotalcite formation. The onset of strätlingite formation is consistently observed at an Al_2O_3 content of 0.66 wt.%, marked by the black line in the graph.

The influence of the Al_2O_3 content on the the composition of the C-(N-)A-S-H gel can be seen in Figure 22. The first plot shows Si, Ca and Al incorporation into the C-(N-)A-S-H gel in a single graph. The unit on the y-axis is $mmol/cm^3$ C-(N-)A-S-H as the total volume of the C-(N-)A-S-H gel also changes with a change in Al_2O_3 content. The three elements are also plotted separately to see the influence on each element separately. In the last two plots, the ratio between Ca/Si and Al/Si can be seen. These two ratio within the C-(N-)A-S-H gel are studied in the literature in certain depths, meaning it could create some guidance for a mixture design.

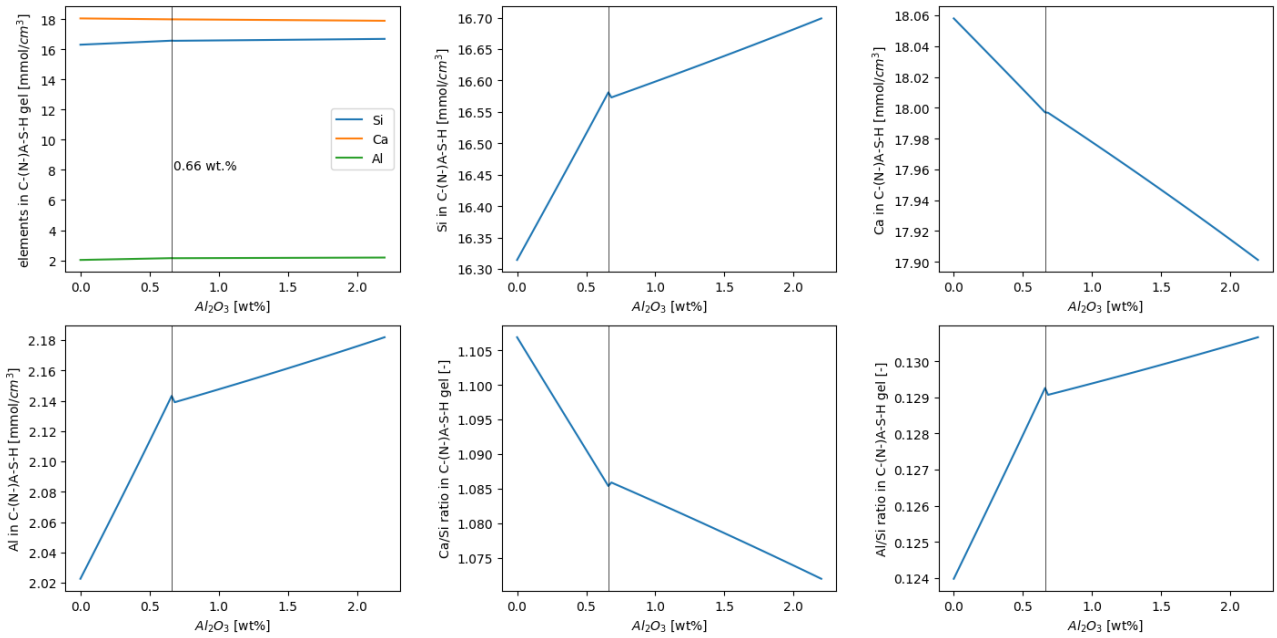

Figure 22: Composition of the C-(N-)A-S-H gel as a function of the Al_2O_3 content.

4.2.2 Mixtures with 6 wt.% Na_2O

The influence of the Al_2O_3 content on the formation of reaction products in a mixture containing 6 wt.% Na_2O can be seen in Figure 23.

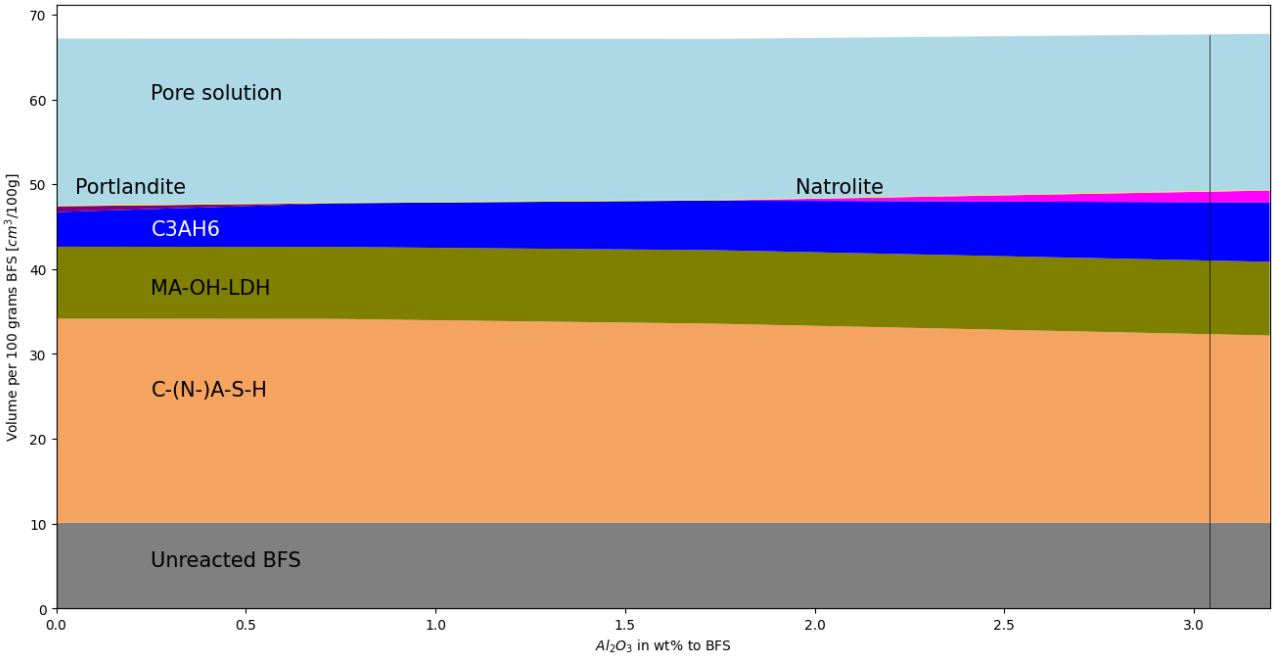

Figure 23: Volume of reaction products formed per 100 grams of BFS as a function of weight percent Al_2O_3 (DoR=70%).

Compared to the N4Ax mixture, strätlingite is no longer forming. The highly alkaline environment, due to increased Na_2O content, inhibits strätlingite formation, as Na_2O is one of the two main variables. Besides its dependency on Na_2O, strätlingite formation also depends on Al_2O_3 content, as shown in Figure 19. However, when Na_2O content surpasses a certain threshold, strätlingite ceases to form, and other reaction products, dependent on Al_2O_3 levels, emerge. In addition to C-(N-)A-S-H, hydrotalcite, and katoite, portlandite forms at Al_2O_3 levels up to 0.74 wt.%, while natrolite appears from 1.73 wt.% Al_2O_3 onward, as shown in Figure 23.

It is logical that when little or no Al_2O_3 is present in the activator, portlandite forms, as only Ca and OH are required for its formation ($Ca(OH)_2$). As Al_2O_3 content in the activator increases, natrolite ($Na_2Al_2Si_3O_{10} * 2H_2O$) begins to form. Being a Na and Al containing mineral, the elevated Na_2O and Al_2O_3 levels create an environment favoring natrolite formation over portlandite or strätlingite.

The volume percentage of the main reaction products are evaluated to see the influence of the Al_2O_3 content in the activator. The volume percentage of the main reaction products over Al_2O_3 content can be seen in Figure 24.

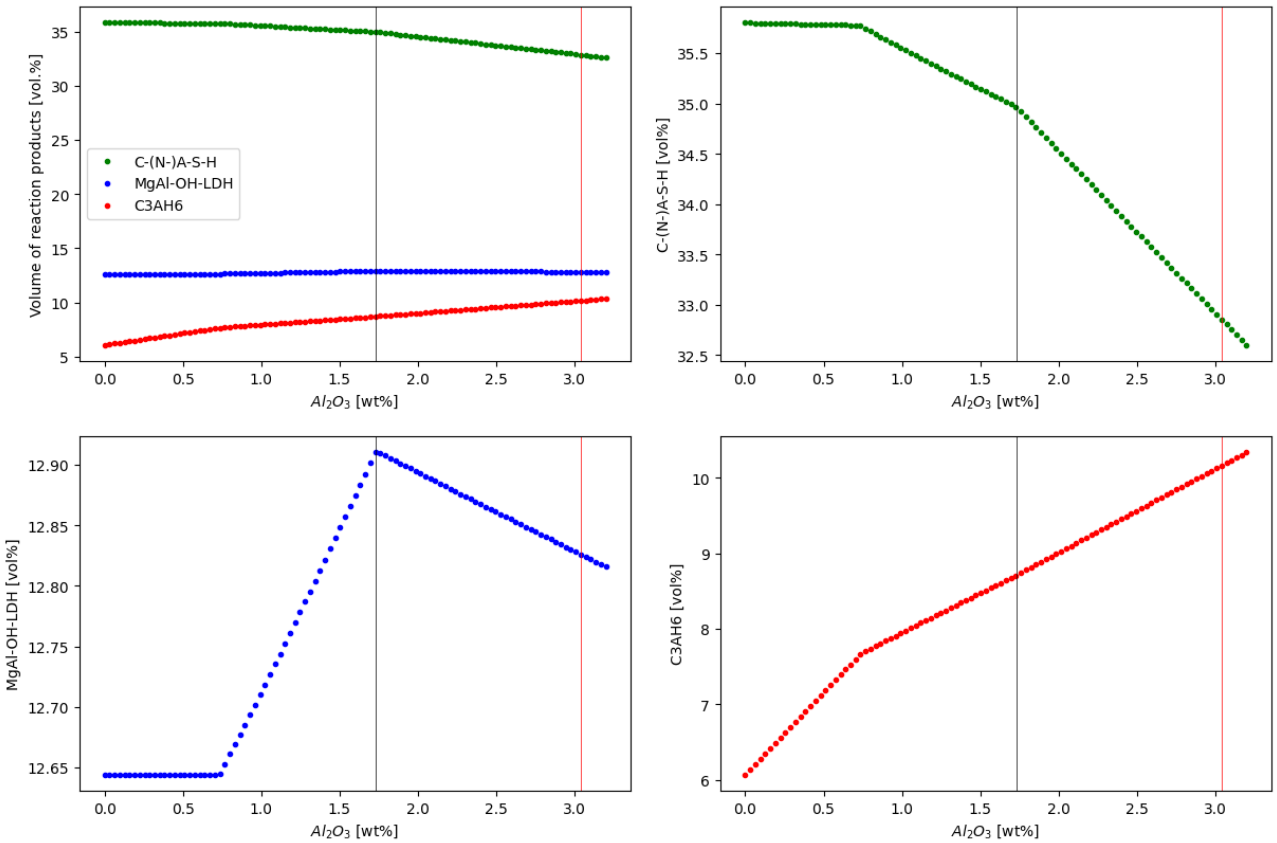

Figure 24: Volume percentage of the main reaction products as a function of Al_2O_3 content. Black line: 1.73 wt.%, red line 3.04 wt.%.

Compared to N4Ax, containing 4 weight percent of Na_2O, there are now two breaking points of slope change. These breaking points can be explained by the presence of two phases, portlandite and natrolite, that do not span the entire Al_2O_3 range. Since both phases depend on Al_2O_3 content, they appear and disappear at certain levels, resulting in variations in the volume percentage of reaction products across the Al_2O_3 content range. The first break point occurs at an Al_2O_3 content of 0.74 wt.%, corresponding to the depletion of portlandite. The second break point appears at an Al_2O_3 content of 1.73 wt.%, marking the onset of natrolite formation. In the katoite graph, natrolite formation shows no adverse impact on katoite production. The graphs suggest that natrolite formed at higher Al_2O_3 concentrations likely incorporates Ca and Si, which would otherwise be integrated into the C-(N-)A-S-H gel at lower Al_2O_3 concentrations.

The influence of the Al_2O_3 content on the Al, Ca, Na, Mg and Si content in the pore solution is shown in Figure 25.

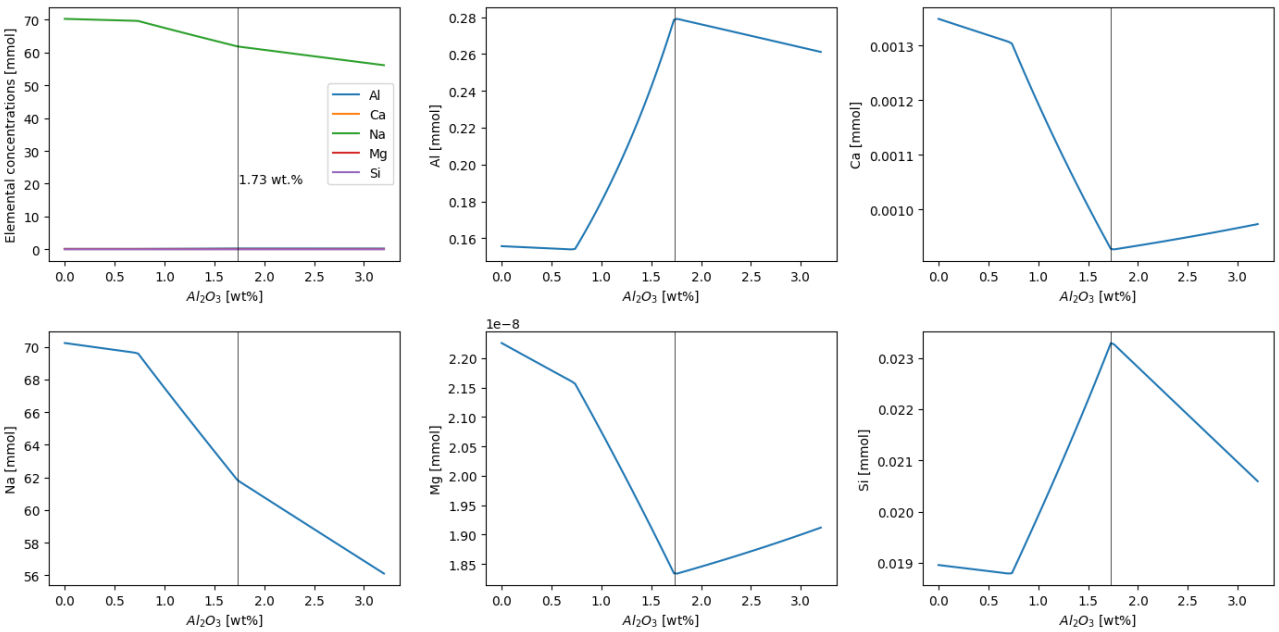

Figure 25: Elemental composition of the pore solution as a function of the Al_2O_3 content.

In the top-left plot, all elements are displayed together, once again showing Na as the most significant element present. Each element shows two slope changes, corresponding to the formation of portlandite and natrolite. Na concentrations remain relatively constant until portlandite disappears, as portlandite itself does not consume Na. Between Al_2O_3 levels of 0.74 and 1.73 wt.%, Na uptake by the C-(N-)A-S-H gel increases, resulting in a decrease of Na in the pore solution. The second slope change for Na corresponds to the onset of natrolite formation, a Na-containing mineral. It is worth noting that Na uptake by the C-(N-)A-S-H gel decreases again after 1.73 wt.% Al_2O_3, yet Na levels in the pore solution continue to fall due to natrolite formation.

The other elements remain relatively stable before the first slope change, indicating that all dissolved elements are sufficiently reacting into solid phases. However, after this initial slope change, Al concentrations rise significantly, suggesting that not enough other elements are dissolving to react with the excess Al. When Al_2O_3 content further increases to 1.73 wt.%, natrolite begins to form, consuming Na, Al, and Si. At this point, Ca concentrations in the pore solution start to increase, as natrolite does not incorporate Ca. The decline in Ca concentrations after 0.74 wt.% Al_2O_3 is due to an increase in Ca-containing phases, which reach their peak at 1.73 wt.% Al_2O_3.

The composition of the C-(N-)A-S-H gel as a function of the weight percentage of Al_2O_3 in the activator can be seen in Figure 26.

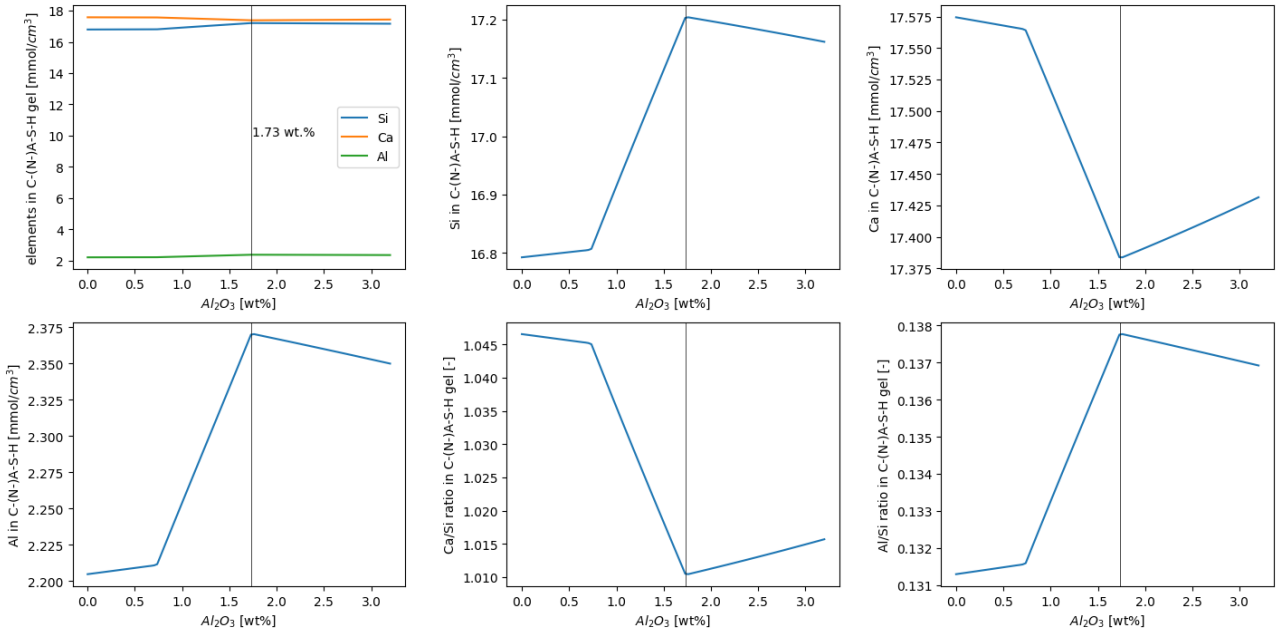

Figure 26: Composition of the C-(N-)A-S-H gel as a function of the Al_2O_3 content.

In the first plot the Si, Ca and Al incorporation into the C-(N-)A-S-H gel are plotted in the same graph. The unit on the y-axis is moles/cm^3 C-(N-)A-S-H as the total volume of the C-(N-)A-S-H gel also changes with a change in weight percentage of Al_2O_3. Ca, Si and Al are shown in separate plots to see the incorporation of the elements into the C-(N-)A-S-H gel as a funciton of Al_2O_3 content The last two plots who the Ca/Si and Al/Si ratio, being parameters that could influence micro properties as stated by the literature (Wang et al., 2022; Zhang, Li, Ghiassi, Yin, & Ye, 2021). Again two breaking points are observed, which are related to portlandite and natrolite formation. It can be seen that the Ca/Si reaches the lowest possible value at 1.73 wt.% of Al_2O_3, while it reaches a maximum value for the Al/Si ratio.

4.2.3 Mixtures with 8 wt.% Na_2O

The influence of the Al_2O_3 content on the formation of reaction products for mixture N8Ax can be seen in Figure 27.

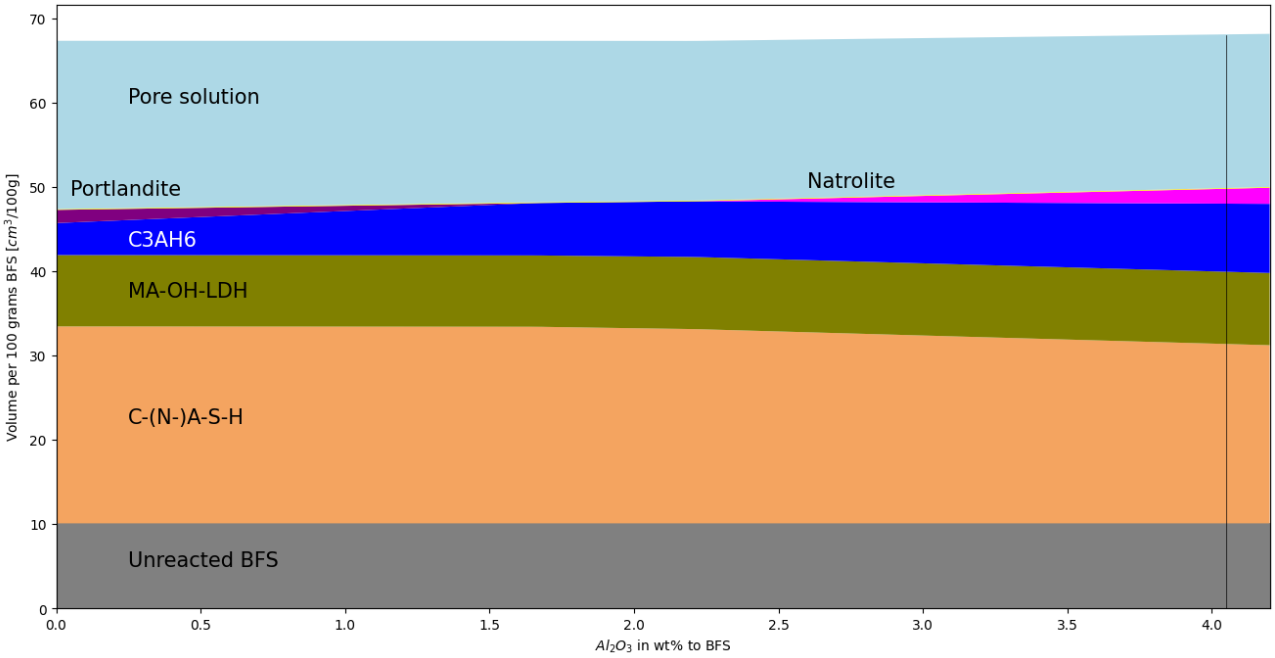

Figure 27: Volume of reaction products formed per 100 grams of BFS as a function of weight percent Al_2O_3 (DoR=70%).

The same reaction products are observed as in mixture N6Ax. However, initially at 0 wt.% of Al_2O_3, there is a larger quantity of portlandite present and the phase is present till an Al_2O_3 content of 1.68 wt.%. From 2.23 wt.% onward, natrolite forms and shows higher volumes compared to N6Ax. Given the similar shape of the graphs, the explanation for the formation of reaction products in N6Ax also applies here.

The standardized volumes of the main reaction plotted as function of Al_2O_3 content can be seen in Figure 28.

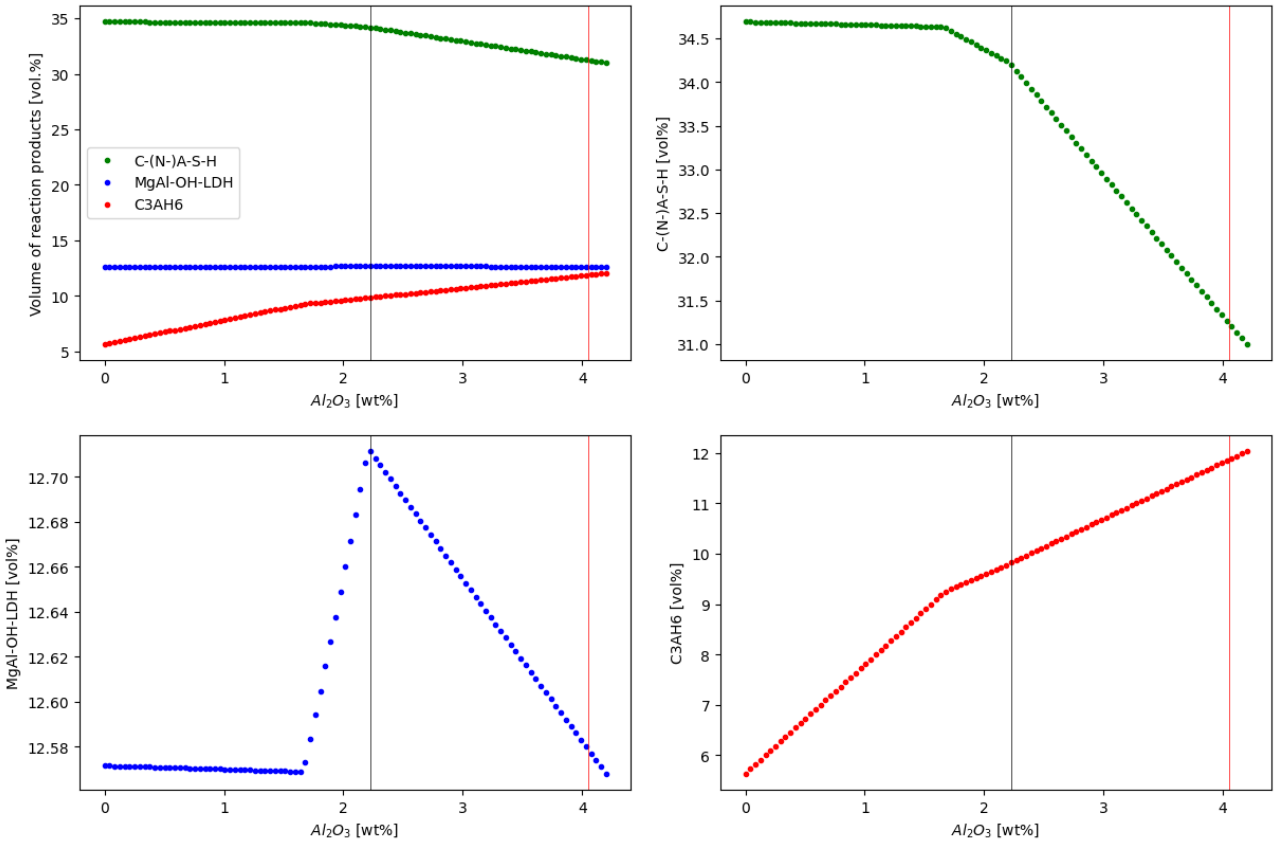

Figure 28: Volume percentage of the main reaction products as a function of Al_2O_3 content. Black line: 2.23 wt.%, red line 4.05 wt.%

Compared to mixtures N4Ax and N6Ax, the C-(N-)A-S-H and hydrotalcite phases are present in lower quantities, while katoite is more abundant. Additionally, the range without portlandite or natrolite is smaller than in mixture N6Ax. As before, the plots exhibit two slope changes, except in the case of katoite. These breaking points of slope change correspond to the formation and disappearance of portlandite and natrolite, indicating that the graph characteristics are driven by the same factors as in mixture N6Ax. The first breaking point is initiated by the depletion of portlandite which leads to an increase in katoite and decrease in C-(N-)A-S-H gel. The formation of natrolite mainly influences the decrease of C-(N-)A-S-H gel, while the katoite formation seems not influenced by this natrolite formation.

The influence of the Al_2O_3 content on the Al, Ca, Na, Mg and Si content in the pore solution is shown in Figure 29.

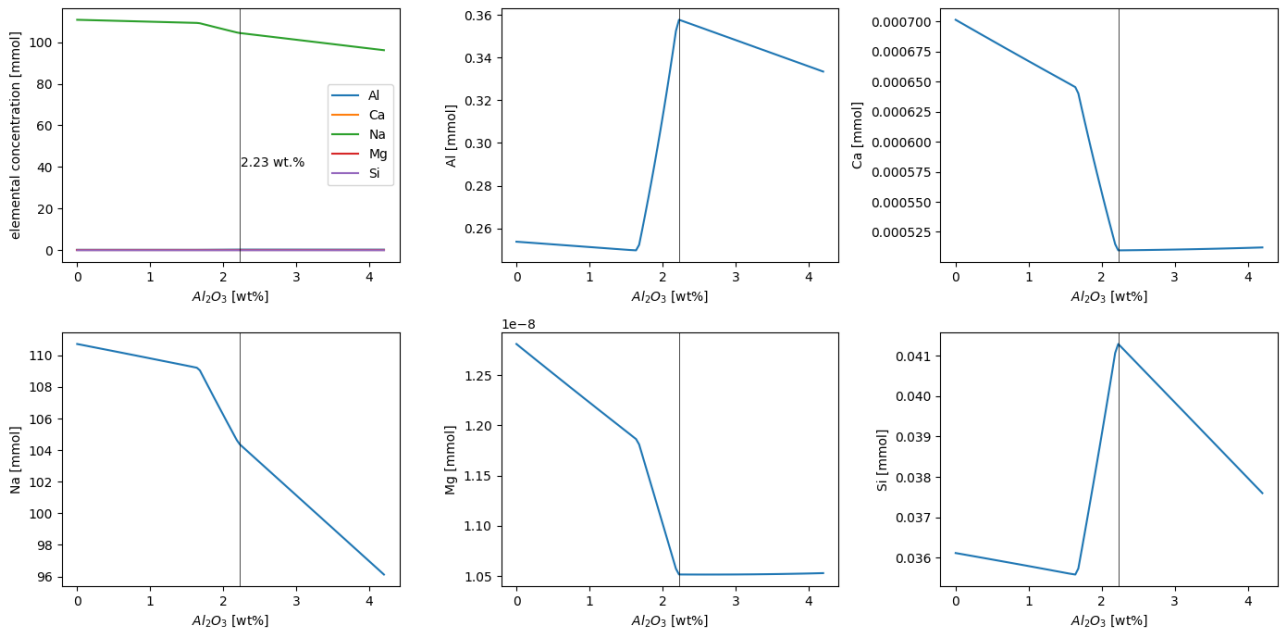

Figure 29: Elemental composition of the pore solution as a function of the Al_2O_3 content.

In the top-left plot, all elements are displayed collectively, with Na identified as the most significant component. Each element exhibits two breaking points that correspond to the formation of portlandite and natrolite. Na concentrations remain relatively stable until the disappearance of portlandite, as portlandite does not consume Na. Between Al_2O_3 levels of 1.68 and 2.23 wt.%, the uptake of Na by the C-(N-)A-S-H gel increases, leading to a reduction of Na in the pore solution. The second slope change for Na aligns with the onset of natrolite formation, a Na-containing mineral. Notably, while Na uptake by the C-(N-)A-S-H gel decreases after 2.23 wt.% Al_2O_3, Na levels in the pore solution continue to decline due to ongoing natrolite formation.

Other elements remain relatively stable prior to the first slope change, indicating that all dissolved species are adequately reacting to form solid phases. Following this initial slope change, Al concentrations increase significantly, suggesting insufficient dissolution of other elements to react with the excess Al. As Al_2O_3 content rises to 2.23 wt.%, natrolite begins to form, consuming Na, Al, and Si. Consequently, Ca concentrations in the pore solution start to increase, as natrolite does not incorporate Ca. The observed decline in Ca concentrations after 1.68 wt.% Al_2O_3 is attributed to the formation of Ca-containing phases, which reach their maximum at 2.23 wt.% Al_2O_3.

The composition of the C-(N-)A-S-H gel as a function of the weight percentage of Al_2O_3 in the activator can be seen in Figure 30.

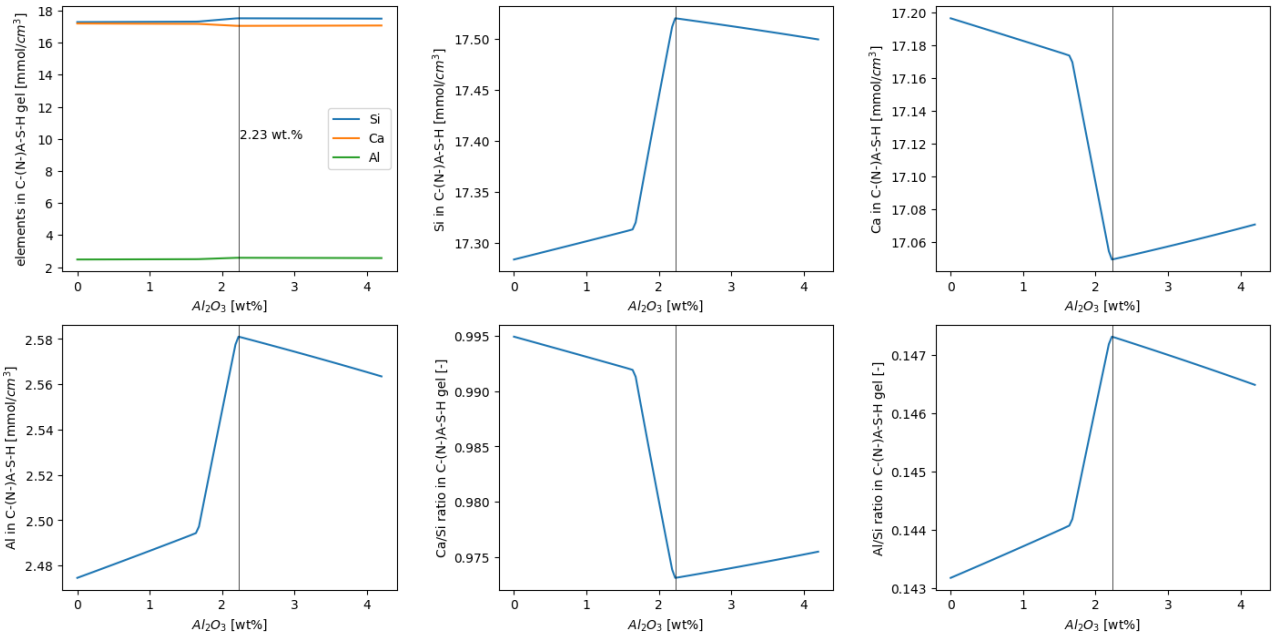

Figure 30: Composition of the C-(N-)A-S-H gel as a function of the Al_2O_3 content.

The first plot shows the Si, Ca and Al incorporation into the C-(N-)A-S-H gel in the same graph. The unit on the y-axis is moles/cm^3 C-(N-)A-S-H as the total volume of the C-(N-)A-S-H gel also changes with a change in weight percentage of Al_2O_3. The three elements are also plotted separately to see the influence on each element separately. In the last two plots, the ratio between Ca/Si and Al/Si can be seen. The Ca/Si ratio also experience a minimum value at an Al_2O_3 content of 2.23 wt.%, while having a maximum Al/Si ratio, showing a similar trend as for N6Ax. It can be seen that the Ca/Si ratio for the N8Ax mixture has the lowest range of values of all mixtures, while the Al/Si ratio has the highest range. This observation shows a relation of these ratios with Na_2O content, this being a decrease in Ca/Si ratio with an increasing Na_2O content and an increasing Al/Si ratio with an increase in Na_2O content.

4.2.4 Key findings

The modelling results clearly demonstrated the influence of Al_2O_3 content in the activator on the formation of reaction products. Some key findings are summarized here as the following: The standardized volume of the primary reaction products as a function of Al_2O_3 content indicated that diluting the activator with a NaOH solution to reduce Al_2O_3 content leads to increased volumes of C-(N-)A-S-H gel compared to solely diluting the etching solution with water. In addition to affecting the volume of C-(N-)A-S-H gel, the Al_2O_3 content in the activator also influences the gel's composition. A lower Ca/Si and higher Al/Si ratio was found for a mixture where the etching solution was diluted with a NaOH solution instead of solely water, potentially impacting the mechanical properties of the resulting material.

The volume of C-(N-)A-S-H gel was found to be the lowest in mixture N8Ax. This mixture not only exhibited a reduced volume of C-(N-)A-S-H gel but also required a greater amount of etching solution to achieve the desired Na_2O content, resulting in a lower overall yield of product. It is therefore concluded that creating mixtures with 8 wt.% Na_2O is not beneficial.

Based on the modelling results it is decided that mixture designs will focus on optimizing the standardized volume and composition of C-(N-)A-S-H gel for a Na_2O content of both 4 and 6 wt.%.

4.3 Mixture design

With the influence of the Al_2O_3 content in the activator on the reaction products investigated, mixture designs with guidance from the GEMS modelling were made. The variables in the mixture designs were chosen to be the Na_2O and Al_2O_3 content in the activator, both expressed in wt.% relative to the precursor. As mentioned before, mixtures with 4 and 6 wt.% of Na_2O are designed. These Na_2O levels were chosen as with lower levels of Na_2O, more product can be obtained from the waste streams. Besides the economic benefits, the amount of C-(N-)A-S-H gel that forms was shown to be higher for the mixtures with a lower weight percentage of Na_2O.

For both 4 and 6 wt.% Na_2O, a reference mixture was designed in which no Al_2O_3 is present in the activator. An additional mixture was prepared where the aluminium etching solution is diluted solely with water, ensuring that 100% of the Na_2O content originated from the etching solution. The etching solution used for this mixture was batch J.C., as discussed in Chapter 3. The composition of 1 kilogram of batch J.C. is provided in Table 13.

Batch J.C. has an aluminium modulus (M_a) of 0.31 or in other words, 0.31 moles of Al_2O_3 is introduced into the system for each mole of Na_2O present.

Table 13: Composition of one kilogram of batch J.C.

Solution	Na_2O [g/kg]	Al_2O_3 [g/kg]	SiO_2 [g/kg]	water [g/kg]
J.C.	168.5	85.3	0.6	745.6

The final mixture designs were informed by the modelling results presented earlier in this chapter, focusing on mixtures containing 4 wt.% and 6 wt.% Na_2O.

As discussed in the previous sections, the modelling results reveal a critical point across all graphs where the maximum yield of C-(N-)A-S-H gel is achieved by reducing the Al_2O_3 content in the activator through dilution of the etching solution with a NaOH solution. This critical point, indicated by the black line in previous sections, marked where the steepest decline in C-(N-)A-S-H gel volume is surpassed, indicating the maximum attainable yield through dilution.

Besides the amount of primary reaction product, it is also essential to consider the composition of the primary reaction product, C-(N-)A-S-H gel, as its composition can influence the mechanical properties of the material. Previous literature established a relationship between the Ca/Si and Al/Si ratios in C-A-S-H gel and its micromechanical properties (Wang et al., 2022). The study focused on two Ca/Si ratios, 1.2 and 0.8, with the latter exhibiting superior micromechanical performance. It was reported that his behavior is attributed to a lower volume of large gel pores (LGP) and a higher mean chain length (MCL), indicating fewer defects (Wang et al., 2022). The study also examined four Al/Si ratios (0, 0.1, 0.2, and 0.3) and found that the Al/Si ratio significantly affected the pore volume. For a gel with a Ca/Si ratio of 0.8, the lowest pore volume was found for an Al/Si ratio of 0.2, while for a Ca/Si ratio of 1.2, the lowest pore volume was found for an Al/Si ratio of 0.3. In both cases, an increase in the Al/Si ratio reduced the pore volume of C-A-S-H gel, suggesting a positive effect on micro-mechanical properties (Wang et al., 2022). The study however noted that the influence of the Ca/Si ratio was significantly higher than that of Al/Si.

Considering the ranges of the Ca/Si and Al/Si ratios in the plots in Figure 22 and 26, the peaks in the Ca/Si and Al/Si plots at the black line in these figures should have a positive influence on the properties as it shows a lower Ca/Si ratio and a higher Al/Si ratio. It should be noted that the peaks are yet based on modelling and it could be that in reality the ratios are different, but nonetheless, it is good guidance for a mixture design.

In other research the influence of the Ca/Si ratio in the C-(N-)A-S-H gel is researched as well, but the mixture designs consist out of 30 or 50% of BFS, leading to lower Ca/Si ratios as there is less Ca available compared to 100% BFS mixtures (Zhang et al., 2021). Besides that, waterglass was also used as activator, introducing more Si in the system which will again lower the Ca/Si ratio. In the paper, the range of Ca/Si ratios in the C-(N-)A-S-H gel vary from 0.4 to 0.9 roughly, where the crack tip toughness and fracture toughness were significantly higher for the higher Ca/Si ratios (Zhang et al., 2021).

Together, these studies demonstrate that the Ca/Si and Al/Si ratio of C-(N-)A-S-H gel can influence mechanical performance. Although data is still incomplete, the optimal mechanical properties appear to occur at a Ca/Si ratio of around 0.8-0.9, with a decrease in performance at both higher (1.2) and lower (0.4) ratios. Given that the Ca/Si ratio in the mixture is slightly above 1.0, it may be advantageous to design mixtures with the lowest Ca/Si and highest Al/Si ratio. For the mixture with 6 wt.% Na_2O, this corresponds to the black line in Figure 26, while for the mixture with 4 wt.% Na_2O, it is close to the minimum value.

Combining all these findings it seems that the mixtures would be optimal when the N4 mixture would be designed with an Al_2O_3 weight percentage of 0.66 wt% and the N6 mixture with an Al_2O_3 weight percentage of 1.73 wt%, which are both the percentages which correspond with the vertical black lines in the plots. In this way, the total volume of C-(N-)A-S-H would be optimal considering diluting costs and the composition of the C-(N-)A-S-H gel would indicate superior micro-mechanical properties.

Table 14 presents the mixture compositions, including reference mixtures where a standard NaOH activator is used. For both 6 wt.% and 8 wt.% Na_2O, two additional mixtures are included besides the reference mixtures. The Al_2O_3 content for these mixtures is derived either from the aluminium etching solution (N4A2.02 and N6A3.04) or based on the reasoning explained earlier in this section (N4A0.66 and N6A1.73). The table also provides the aluminium modulus, M_a, for each mixture.

Table 14: Mixture designs with M_a, the molar ratio of $\frac{Al_2O_3}{Na_2O}$ present in the activator.

Mixture	BFS [g]	$water$ [g]	Na_2O [g]	Al_2O_3 [g]	M_a [-]
REFN4	100	40	4	0	0
N4A0.66	100	40	4	0.66	0.10
N4A2.02	100	40	4	2.02	0.31
REFN6	100	40	6	0	0
N6A1.73	100	40	6	1.73	0.18
N6A3.04	100	40	6	3.04	0.31

The mixtures were checked if they satisfy the equations set in Table 1. The check of these ratios can be seen in Table 15.

Table 15: Check of the ratios of Table 1 including Al_2O_3. All equations satisfy the boundary conditions

Sample	$\frac{CaO+MgO+Al_2O_3}{SiO_2} \geq 1.4$	$\frac{CaO+MgO}{SiO_2+Al_2O_3} \geq 1.0$	$0.1 \geq \frac{Al_2O_3}{SiO_2} \geq 0.6$
REFN4	1.89	1.12	0.36
N4A0.66	1.91	1.11	0.38
N4A2.02	1.95	1.07	0.42
REFN6	1.89	1.12	0.36
N6A1.73	1.94	1.08	0.41
N6A3.04	1.98	1.05	0.45

The equations in the table are usually only applicable to the BFS. Given that there is an Al_2O_3 equivalent present in the activator, the equations are applied on the total mixture, thus including activator. It should be noted that the Al_2O_3 is already dissolved in the activator and therefore the equations are not completely accurate for the activator part, but for the sake of initial mixture designs it is assumed to be applicable for the Al_2O_3 equivalent in the activator as well.

Based on the mixture designs shown in Table 14 and the composition of the aluminium etching solution shown in Table 13, the mixing ratios of the activator for each mixture can also be determined. The activator designs can be seen in Table 16.

Table 16: Mixture designs of the activators for 100 grams of BFS.

Sample	**J.C. [g]**	**NaOH [g]**	**Added water [g]**	**Total volume [ml]**
REF-N4	0	5.16	38.84	40
N4A0.66	7.74	3.48	33.45	40.12
N4A2.02	23.73	0	22.30	40.38
REF-N6	0	7.74	38.26	40
N6A1.73	20.29	3.33	24.12	40.33
N6A3.04	35.59	0	13.46	40.56

4.4 Formation of reaction products over degree of reaction

The formation of reaction products as a function of the degree of reaction can be analyzed for the mixtures designed in the previous section. While the degree of reaction typically varies over time, for the purposes of this initial research, it is represented on the x-axis.

4.4.1 N4 mixtures

This section shows the formation of reaction products over reaction degree for the three mixtures with 4 wt% of Na_2O in the activator. The formation of reaction products over reaction degree for mixture N4REF can be seen in Figure 31.

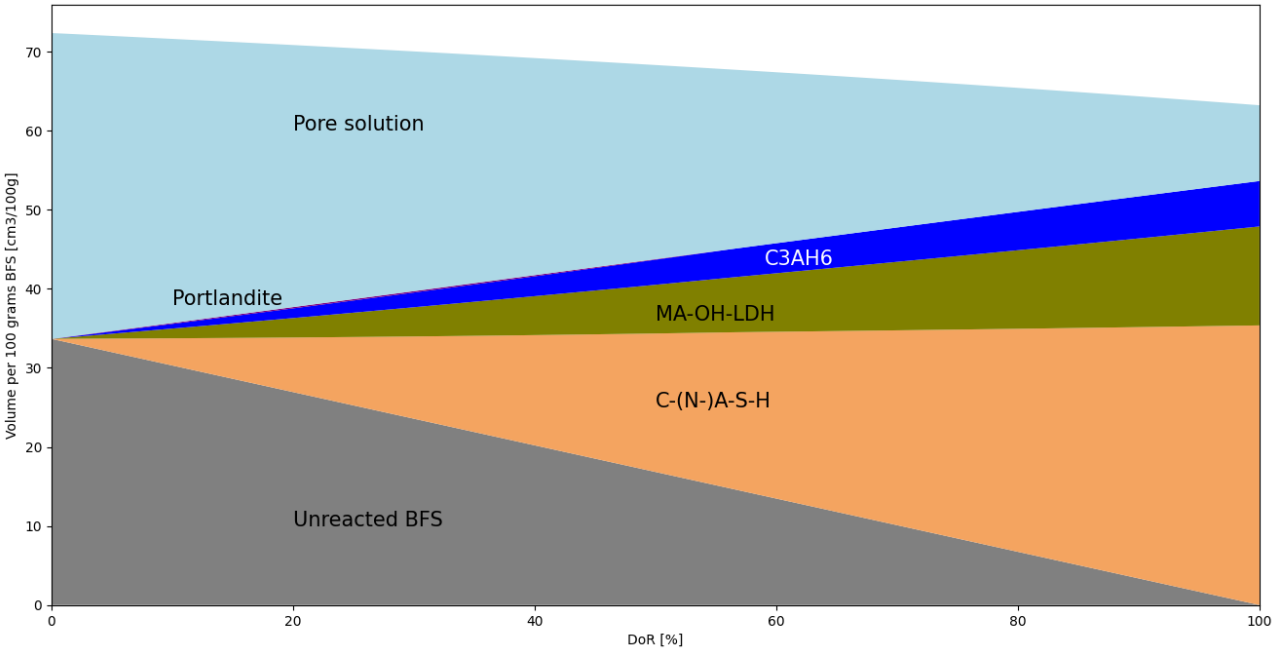

Figure 31: Reaction products over degree of reaction for mixture N4REF

The graphs shows that in the early stage, some portlandite forms, but other than that, only C-(N-)A-S-H, hydrotalcite and katoite (C3AH6) forms.

The formation of reaction products over reaction degree for mixture N4A0.66 can be seen in Figure 32.

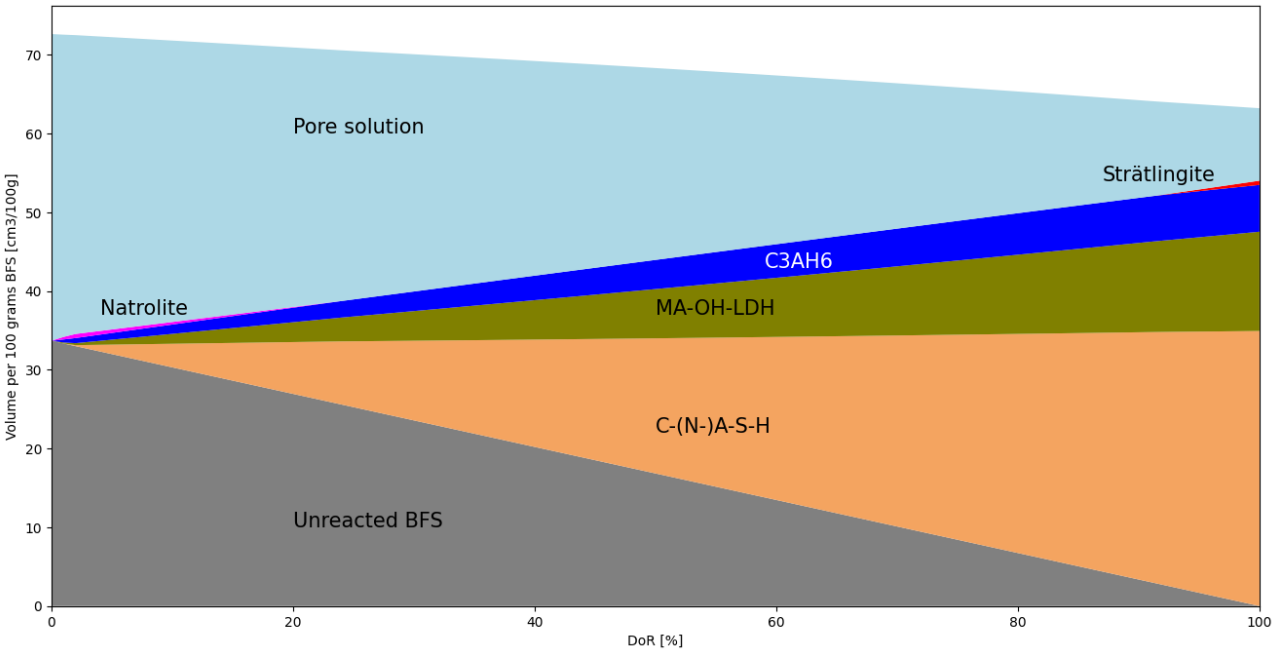

Figure 32: Reaction products over degree of reaction for mixture N4A0.66

The reaction products that form are almost identical to the reference mixture as well as their quantities. However, at a low reaction degree a small amount of natrolite forms instead of portlandite and in a later stage, strätlingite forms. Both natrolite and strätlingite form in small amounts indicating that the influence would be minimal.

The formation of reaction products over reaction degree for mixture N4A2.02 can be seen in Figure 33.

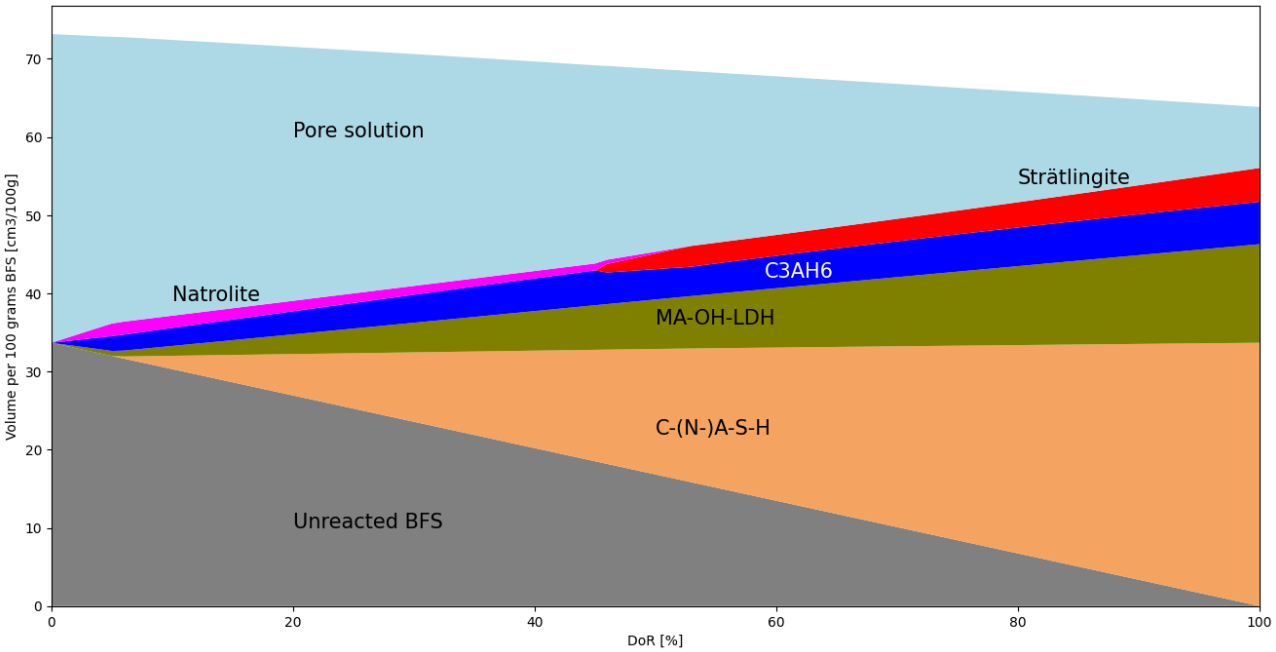

Figure 33: Reaction products over degree of reaction for mixture N4A2.02

Mixture N4A2.02 exhibits significant differences in the graphs compared to mixtures N4REF and N4A0.66. The data indicate that both the range and quantity of natrolite and strätlingite increase notably with higher Al_2O_3 content in the activator. Furthermore, it is observed that C-(N-)A-S-H gel begins to form at a higher degree of reaction, which coincides with a decreasing volume of natrolite, suggesting a consumption of natrolite into C-(N-)A-S-H gel. Additionally, the formation of strätlingite correlates with a decline in katoite, implying that katoite may be transforming into strätlingite. Literature reported that the formation of strätlingite can improve mechnical properties as it is a stable secondary phase complementary to the primary reaction products (Okoronkwo & Glasser, 2016).

4.4.2 N6 mixtures

This section shows the formation of reaction products over the degree of reaction for the three mixtures with 6 wt% of Na_2O in the activator. The formation of reaction products over reaction degree for mixture N6REF can be seen in Figure 34.

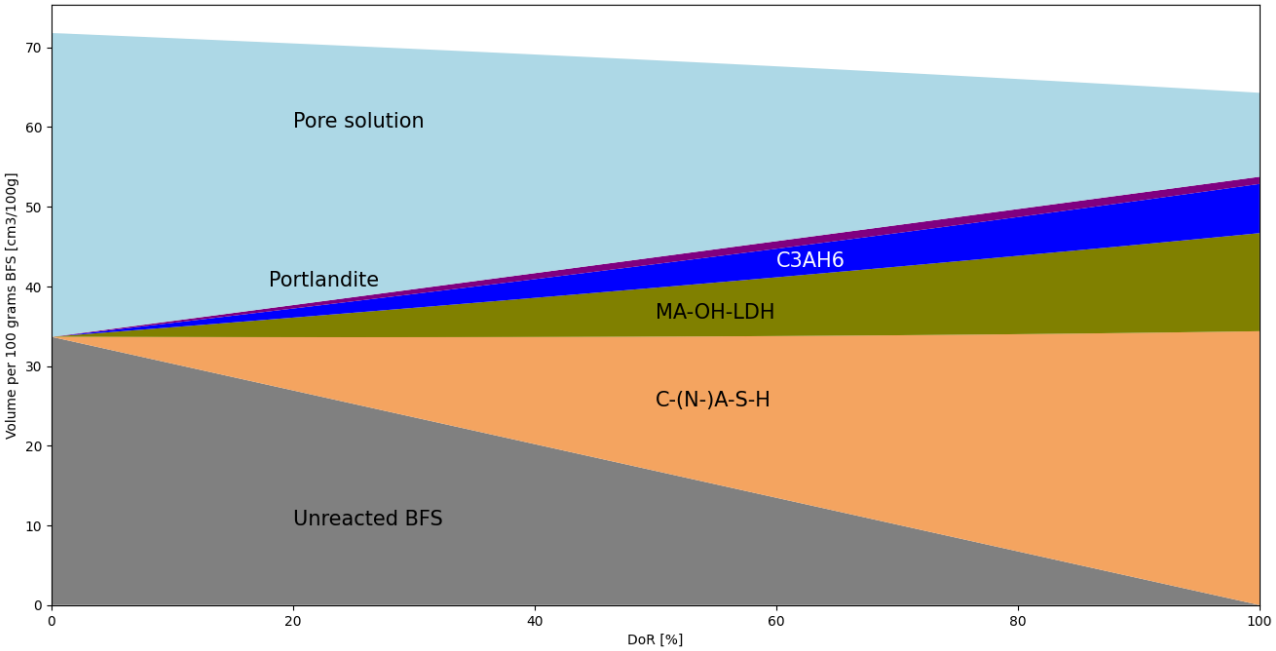

Figure 34: Reaction products over degree of reaction for mixture N6REF

Compared to mixture N4REF, there is an increased presence of portlandite, which is observed throughout the entire degree of reaction rather than being limited to a small interval. Given that the solubility of portlandite decreases with an elevated pH, it is logical that portlandite is more dominant in N6REF than in N4REF (Bouzouaid, Lothenbach, Fernandez-Martinez, & Labbez, 2021).

The formation of reaction products over the degree of reaction for mixture N6A1.73 can be seen in Figure 35.

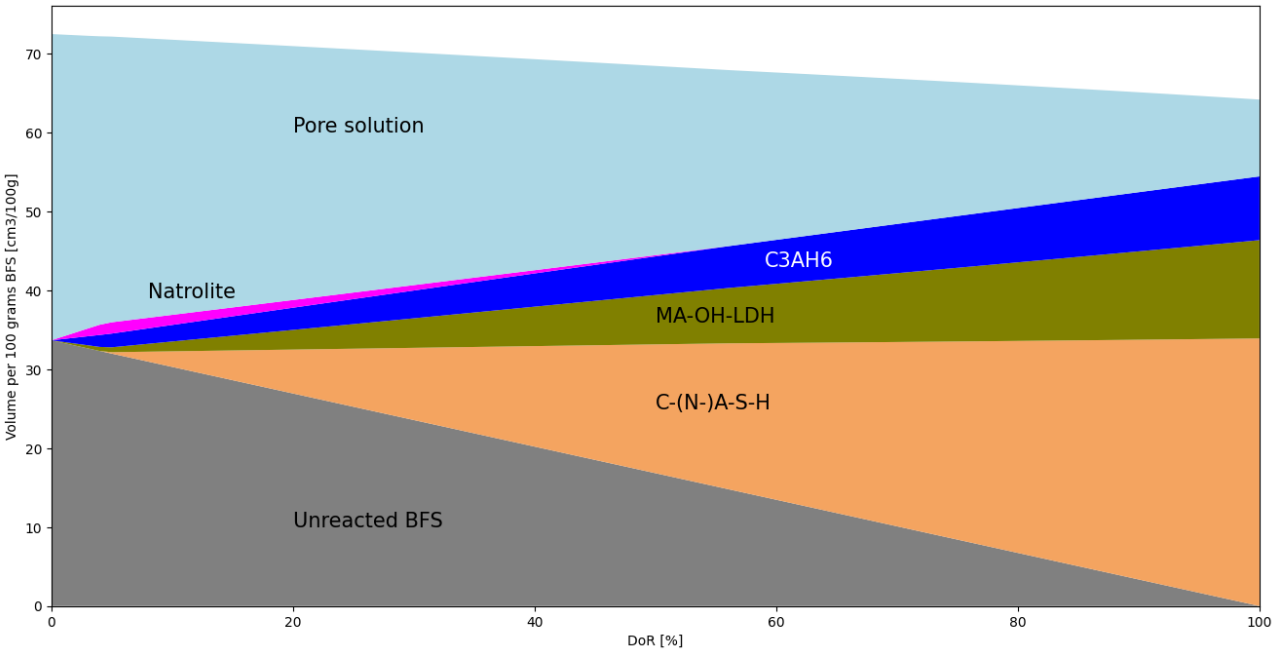

Figure 35: Reaction products over degree of reaction for mixture N6A1.73.

In contrast to mixture N6REF, portlandite is no longer present; however, natrolite is observed, which diminishes at a degree of reaction of 56%. Similarly to the N4A2.02 mixture, the formation of C-(N-)A-S-H gel begins at the point where the volume of natrolite starts to decrease.

The formation of reaction products over the degree of reaction for mixture N6A3.04 can be seen in Figure 36.

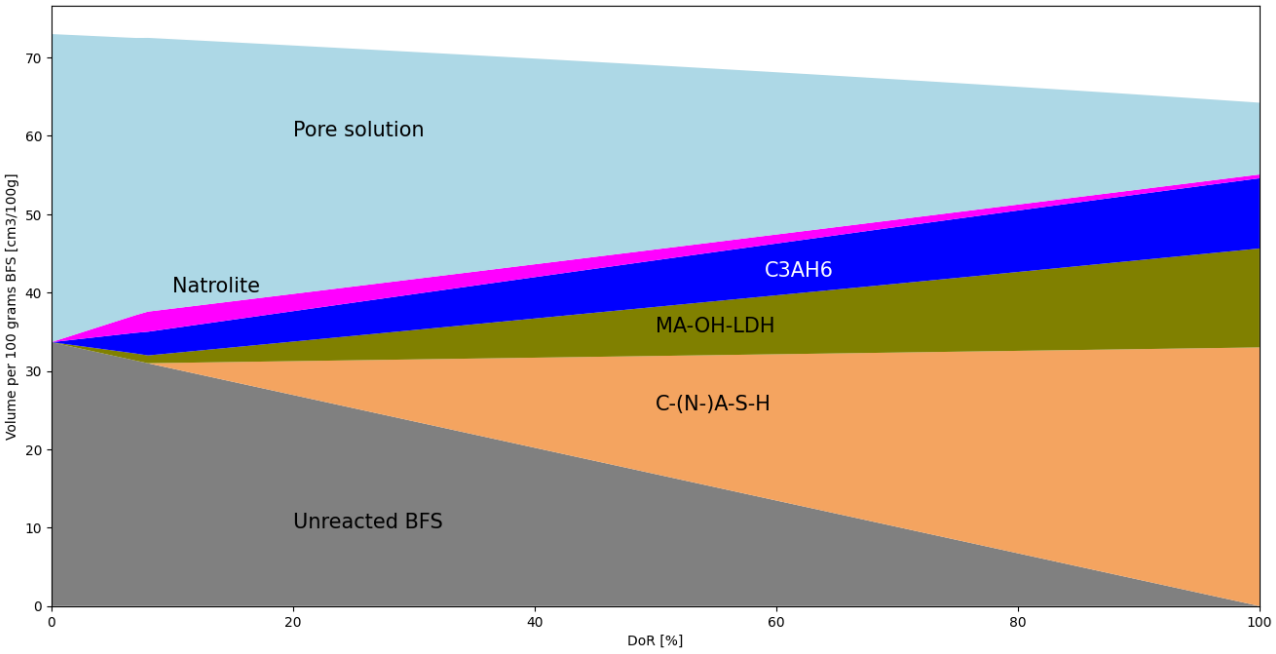

Figure 36: Reaction products over degree of reaction for mixture N6A3.04.

The graph resembles that of mixture N6A1.73; however, the quantity of natrolite is greater in N6A3.04. Rather than diminishing at higher degrees of reaction, natrolite persists throughout the entire reaction. Consequently, the increased presence of natrolite corresponds to a reduced amount of C-(N-)A-S-H gel in this mixture compared to N6A1.73. Compared to N4A2.02, no strätlingite formation occurs throughout the graph. The elevated Al_2O_3 content would suggest favorable conditions, but a too high alkalinity prohibits the formation of strätlingite (Okoronkwo & Glasser, 2016).

4.5 Conclusions

- Thermodynamic modelling using GEMS provided valuable insights for designing mixture compositions. Given that the key elements in the activator are Na_2O and Al_2O_3, the modelling concentrated on the impact of varying Al_2O_3 content while maintaining a constant Na_2O level.
- This approach clarified how different reaction products are formed, the volume percentages of the main reaction products, the pore solution chemistry, and the composition of C-(N)A-S-H, leading to the development of effective mixture designs.
- The mixture designs were then reintroduced into the model to examine the formation of reaction products as the degree of reaction (DoR) progressed. It was found that mixtures N4REF and N6REF, in addition to C-(N-)A-S-H, hydrotalcite and katoite, produced portlandite as well. Notably, N6REF exhibited a greater presence of portlandite due to the elevated pH.
- Mixtures N4A0.66 and N4A2.02 did not exhibit any formation of portlandite, unlike N4REF. Instead, these mixtures demonstrated natrolite formation at low degrees of reaction (DoR), transitioning to strätlingite at higher DoR. A similar trend was noted for N4A2.02, which featured both natrolite and strätlingite in more substantial quantities.
- Mixtures N6A1.73 and N6A3.04 did not show any formation of portlandite, as observed in N6REF. However, both mixtures developed natrolite at low degrees of reaction (DoR), with its volume decreasing as the DoR increased. Notably, N6A3.04 displayed larger volumes of natrolite and maintained the presence of this phase throughout the entire DoR.

5 Experimental study on the reaction process

This section presents experiments related to the reaction process, including the dissolution test, isothermal calorimetry, degree of reaction determination, and pore solution analysis. First, the materials and mixtures are described, followed by the methodology for each experiment. Subsequently, the results are presented and discussed, concluding with key findings.

5.1 Materials and methods

5.1.1 Materials and mixtures

The BFS used in the experimental study is the same as presented in Section 4.1, with an average particle size of 19 μm (Zuo, 2019). Analytical grade NaOH pellets ($\geq$ 98%), the aluminium etching solution as characterized in Chapter 3 and de-mineralized water were used to prepare the activators as shown in Table 16, in Section 4.3. The mixtures designs are also presented in Section 4.3, with details provided in Table 14.

5.1.2 Dissolution test

The dissolution test can be performed using different methodologies as there is not a standard for this experiment. A study in the literature reported a ratio of 1 gram of precursor to 10 ml of solution (Zhang, Keulen, Arbi, & Ye, 2017), while another study reported a ratio of 1 gram of precursor to 2000 ml of solution (Zuo, 2019). As the precursor in this research is similar to the latter study, the same precursor to solution ratio was used. Besides the precursor to solution ratio, the alkalinity of the solution and the time where measurements were made were also variables. As the precursor is similar, the alkalinity of the solution is the same as found in the literature, being a concentration of 3 mol/Liter of NaOH (Zuo, 2019). As the only purpose of the dissolution test is the investigate the influence of the dissolved aluminium in the activator on the dissolution of the precursor, only two different solutions were be investigated. As stated before a 3 mol/L NaOH solution was used as reference and a solution with the an equivalent NaOH concentration, obtained from the Al etching solution was used. The designs for the solutions can be seen in Table 17.

Table 17: Solution composition for the dissolution test

Solution	**Water [g]**	**NaOH pellets [g]**	**Waste solution [g]**
Reference	1000 g	120 g	0 g
Al. containing	579,8 g	0 g	551,7 g

The time increments of measurement are also variables which have to be determined. It is decided to have similar time increments as in the study with the similar precursor and solution (Zuo, 2019). However, the measurement is extended to 360 minutes instead of 120 minutes. The times of measurement was at 0, 10, 30, 60, 120 and 360 minutes. It should be noted that only for the Al. containing solution, a measurement at t=0 was made as the composition is already known for the reference mixture, but for the Al. containing activator, variation can be present in the Al etching solution.

In order to have a minimal impact of taking the samples out of the test set-up, a volume of 500 ml of solution is used, meaning that 0.25 grams of BFS has been added to the set-up. The entire solution is stirred continuously during the experiment in such a way that the solution can be assumed to be homogeneous. By extracting approximately 2-5 ml out of the test set-up each time, a total of 10-25 ml is removed out of the system. The liquid was taken out of the system by a filter syringe to guarantee that there are no solids in the samples in order to avoid any further dissolution after extraction. Once all the samples are extracted, an ICP-OES analysis was performed on the samples to measure Ca, Si and Al concentrations.

5.1.3 Isothermal Calorimetry

Isothermal calorimetry was conducted using a TAM Air calorimeter. For each mixture, 5 grams of paste was prepared and placed in an ampoule. A reference ampoule containing water with an adjusted volume was used to match the paste's specific heat capacity. The heat of reaction was recorded over a period of up to two weeks. This procedure is a modified version of NEN-EN 196-8, adjusted for the specific cementitious material used and a flexible duration, as the paste heat release profiles were initially unknown.

Upon analyzing the results, the maximum cumulative heat release was determined from the resulting graphs. An appropriate model was selected based on data fit, and the model parameters were evaluated. With the maximum cumulative heat release, the degree of reaction as a function of time can be calculated, enabling the modelling of reaction product formation over time using GEMS.

5.1.4 Pore solution chemistry

For the pore solution experiment, cylindrical samples of the paste were first cast and cured under sealed conditions for 1, 7, and 28 days. After the designated curing times, the samples were compressed within a steel cylinder to expel the pore solution through a slit at the bottom of the steel cylinder. The extracted pore solution was collected using a pipette and immediately filtered through a syringe filter to remove any solids. The pH of the filtered solution was measured promptly following extraction. The filtered solutions were then stored in a refrigerator until they could be analyzed using ICP to determine concentrations of Al, Ca, Si, and Na. The concentrations of these elements were also modelled in GEMS by simulating the amount of moles in the aqueous solution and the volume of the aqueous solution. By dividing the amount of moles by the volume of the aqueous solution, the theoretical concentrations were obtained. These theoretical concentrations and the trend of these concentrations over time could then be compared to the experimental results.

5.2 Results and discussion

5.2.1 Dissolution test

The results for the aluminium-containing solution are, unfortunately, not fully representative of the actual dissolution of BFS in the solution, as the measured increase in Al concentration exceeds the Al content introduced by BFS alone. This suggests that Al is being introduced into the system from a source other than BFS. A likely explanation is the presence of very small precipitates in the Al etching solution, which dissolve under the intense stirring conditions applied in the dissolution test.

This possible interference makes it challenging to accurately determine the BFS dissolution in the solution containing the Al etching solution. While filtering the waste solution prior to testing could remove any Al contributions from these precipitates, it would reduce comparability with the intended practical application, where the activator would contain unfiltered alkaline waste solution. Even with filtering, challenges would remain. The initial concentrations of Al, Si, and Ca in the etching solution containing sample are already above zero, promoting precipitate formation. Consequently, it would remain uncertain whether observed concentration variations stem from BFS dissolution or the dissolution of existing precipitates.

The results of the dissolution test for the aluminium containing solution are presented in Appendix A and the results of the reference sample can be seen in Figure 37, showing similarity with the dissolution test in the literature as shown in Appendix B (Zuo, 2019).

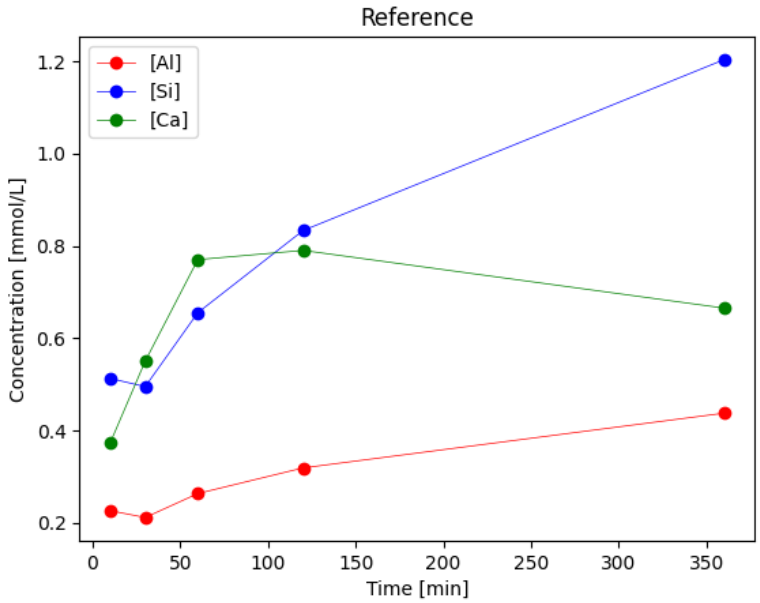

Figure 37: Concentrations of the elements over time for the solution without any initial dissolved aluminium

While the dissolution of BFS in the aluminium-containing solution is not the primary focus of this research as the results were invalid, it is essential to recognize that initial concentrations in this solution significantly impact the dissolution behavior of the precursor. Literature indicates that the dissolution rates of amorphous SiO_2 and Al_2O_3 are influenced by the presence of other elements, whereas the dissolution of CaO primarily depends on the pH of the environment (Zuo, 2019). It has been reported that the logarithmic forward dissolution rate of Ca from BFS increases with pH, as described by Equation 8 (Zuo, 2019).

$$log(r_{+,Ca}) = 0.1868pH - 8.7729 \tag{8}$$

The logarithmic forward dissolution rate of SiO_2 depends not only on pH but also on the reactivity of the aluminosilicate precursor, represented by the NBO/T ratio. This ratio describes the proportion of non-bridging oxygen atoms in tetrahedral coordination. The forward dissolution rate of SiO_2 can be expressed by Equation 9 (Zuo, 2019).

$$log(r_{+,Si}) = 0.0155pH * NBO/T + 0.0727pH + 0.6199NBO/T - 9.0309 \tag{9}$$

Finally, the logarithmic forward dissolution rate of Al_2O_3 is influenced by the molar ratio of Al to Si in the precursor and by the logarithmic forward dissolution rate of SiO_2. This relationship is expressed in Equation 10 (Zuo, 2019).

$$log(r_{+,Al}) = log(\frac{\nu_{Al}}{\nu_{Si}}) + log(r_{+,Si}) \tag{10}$$

Since all the equations describe logarithmic forward dissolution rates, a less negative value indicates a higher forward dissolution rate. As these rates are linearly related to the forward dissolution rate, they provide insight into how different parameters affect the dissolution of each element.

It's also noteworthy that the dissolution of CaO or portlandite ($Ca(OH)_2$), tends to decrease as pH increases (Bouzouaid et al., 2021; Provis & van Deventer, 2014), which contrasts with the equation mentioned above. During the reaction, conditions may initially promote portlandite formation; however, as the pH later decreases, this phase could dissolve, releasing Ca ions back into the pore solution. Additionally, the dynamic consumption and dissolution rates of ions can result in fluctuating ion concentrations within the pore solution throughout the reaction. The composition of the pore solution is investigated later in this chapter.

5.2.2 Isothermal Calorimetry

The normalized heat release and the cumulative heat release for the mixtures containing 4 wt.% of Na_2O can be seen in Figure 38.

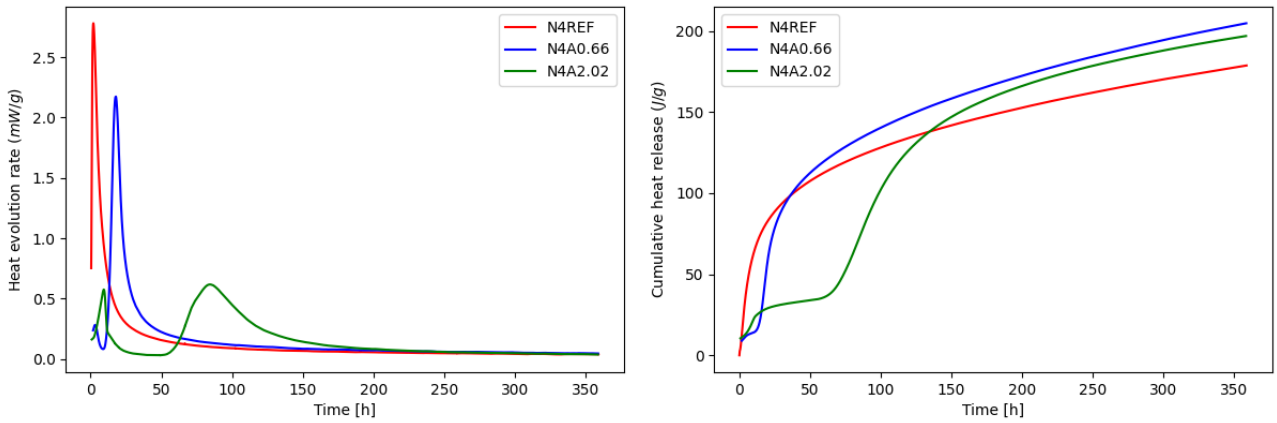

Figure 38: Heat evolution rate over time and cumulative heat release for the mixtures with 4 wt% of Na_2O

Both heat flow and cumulative heat are normalized to 1 gram of paste, and the heat released during the initial dissolution of the precursor is excluded from the data. Excluding the dissolution peak prevents an abrupt, steep incline at the beginning of the cumulative heat release graph. Since this peak is not directly related to the heat of reaction, it was decided to omit it from the results. This means that for N4REF, the first 20 minutes of data were excluded, while for N4A0.66, the first 100 minutes were omitted, and for N4A2.02, the initial 44 minutes were disregarded.

The normalized heat release and the cumulative heat release for the mixtures containing 6 wt.% Na_2O can be seen in Figure 39.

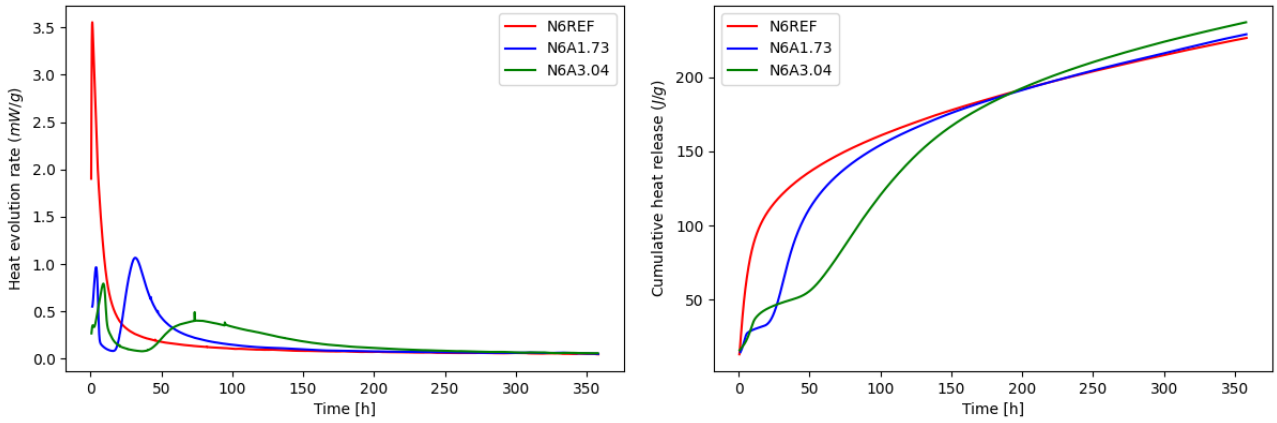

Figure 39: Heat evolution rate over time and cumulative heat release for the mixtures with 6 wt% of Na_2O

For the mixtures containing 6 wt.% Na_2O the data is also normalized to 1 gram of paste, with the initial dissolution peak omitted to maintain clarity of the reaction peaks. This means that for N6REF, the first 27 minutes of data were excluded, while for N6A1.73, the first 73 minutes were omitted, and for N6A3.04, the initial 39 minutes were disregarded.

The maximum cumulative heat release (Q_{max}) can be determined by fitting a curve to the data using different models, in which Q_{max} is a key parameter. By finding the best fit for the data, Q_{max} can be accurately estimated. Two commonly used models for curve fitting in calorimetry studies are the exponential- and Knudsen model. The exponential model, shown in Equation 11, includes a time parameter (τ), a shape parameter (β) and the time in hours (t) (Chithiraputhiran & Neithalath, 2013). The Knudsen model is shown in Equation 12, where K_T is the rate constant and t_0 is the time constant, marking the end of the induction period (Chithiraputhiran & Neithalath, 2013).

$$Q(t) = Q_{max} * exp(-\frac{\tau}{t})^{\beta} \tag{11}$$

$$Q(t) = Q_{max} * \frac{K_T * (t - t_0)}{1 + K_T * (t - t_0)} \tag{12}$$

The rate constant in the Knudsen model has been reported to be equivalent to $1/t_{50}$, where t_{50} is represents the time where a reaction degree of 50% is reached (Y. Sun et al., 2023), (Chithiraputhiran & Neithalath, 2013). This leads to a simplified form of Equation 12, as shown in Equation 13.

$$Q(t) = Q_{max} * \frac{(t - t_0)}{t_{50} + (t - t_0)} \tag{13}$$

Mixtures containing the Al etching solution exhibit multiple peaks in the normalized heat release, resulting in a cumulative heat release curve that is deformed compared to the reference mixtures. Due to these multiple slope changes, the exponential model does not fit the cumulative curves well. While one approach could involve applying multiple exponential models to different sections of the graph, this seems unnecessary, as the primary objective is to determine Q_{max}. It was found that the best method to estimate Q_{max} is to apply the Knudsen model to the latter half of the dataset, excluding the the sections with multiple slope changes. The parameters of the Knudsen model and the coefficient of determination (R^2) for all mixtures can be seen in Table 18. As all R^2 values are close to 1.0, it can be concluded that the model fits the data effectively.

Table 18: Parameters derived from the Knudsen model, with R^2 representing the coefficient of determination.

Mixture	**Qmax [J/g]**	**t_0 [h]**	**t_{50} [h]**	**R^2 [-]**
N4REF	225	0.37	95.13	0.995
N4A0.66	265	1.71	108.21	0.996
N4A2.02	256	0.76	108.08	0.999
N6REF	290	0.49	103.57	0.994
N6A1.73	299	1.25	113.73	0.994
N6A3.04	333	0.67	145.19	0.999

Using the Q_{max} value presented in Table 18, the degree of reaction can be calculated by dividing the cumulative heat release at time t by the maximum cumulative heat release. The degree of reaction is expressed in Equation 14.

$$\alpha(t) = \frac{Q(t)}{Q_{max}} \tag{14}$$

By integrating the calorimetry data with extrapolations from the Knudsen model, the degree of reaction during the first 28 days can be established for each mixture. Only the degree of reaction over the first 28 days was established as this research only focuses on the first 28 days, besides that most reaction occurs in the first 28 days, meaning that extending the time will give only limited extra insight. Combining this data with the GEMS model presented in Chapter 4, the formation of reaction products over time can be visualized.

The formation of reaction products during the first 28 days for mixture N4REF is presented in Figure 40.

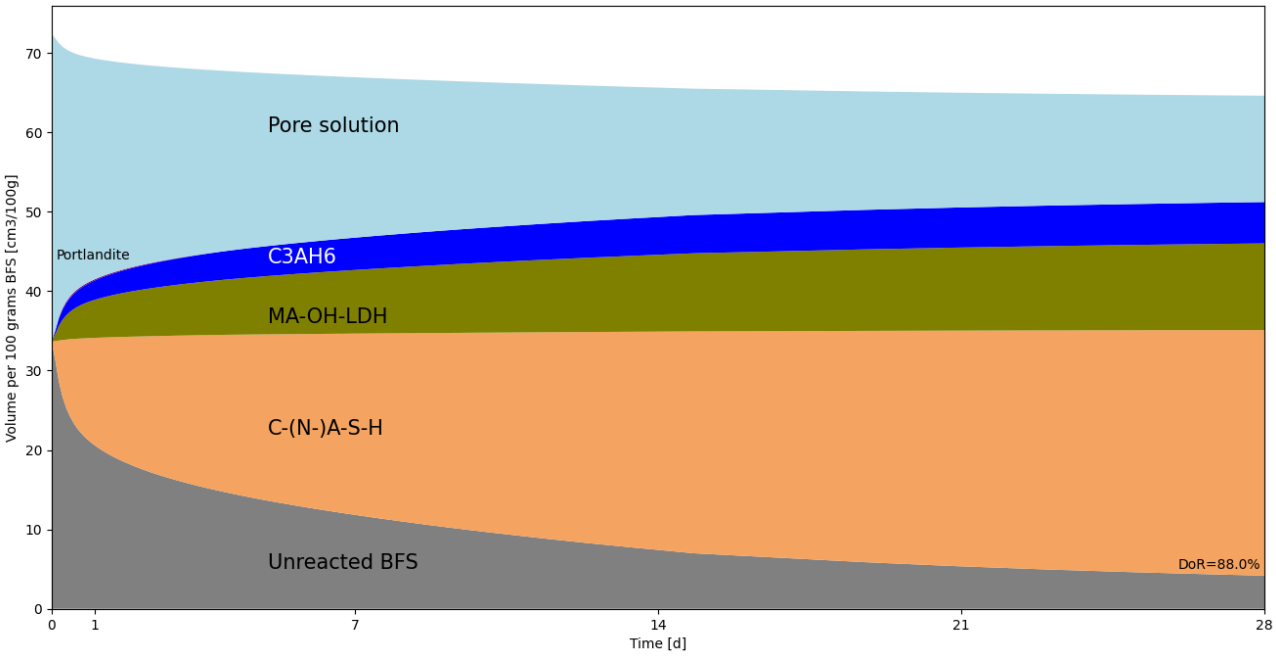

Figure 40: Formation of reaction products for mixture N4REF during the first 28 days

The graph shows that the unreacted blast furnace slag (BFS) decreases rapidly in the initial stages, reaching a relatively stable volume around 21 days. Within the first 10 hours, a small fraction of portlandite forms, which subsequently transforms into other phases after this period. This observation can be attributed to a significant decrease in the pH of the pore solution during the early stages, as hydroxide ions are consumed for dissolution. At lower pH levels, the solubility of portlandite increases (Bouzouaid et al., 2021), allowing it to dissolve into calcium ions that can then be incorporated into other phases. The formation of the other reaction products is straight forward. In the early stage, the vast majority of the reaction is taking place and the volume of the reaction products increase linearly with the degree of reaction.

The formation of reaction products during the first 28 days for mixture N4A0.66 is presented in Figure 41.

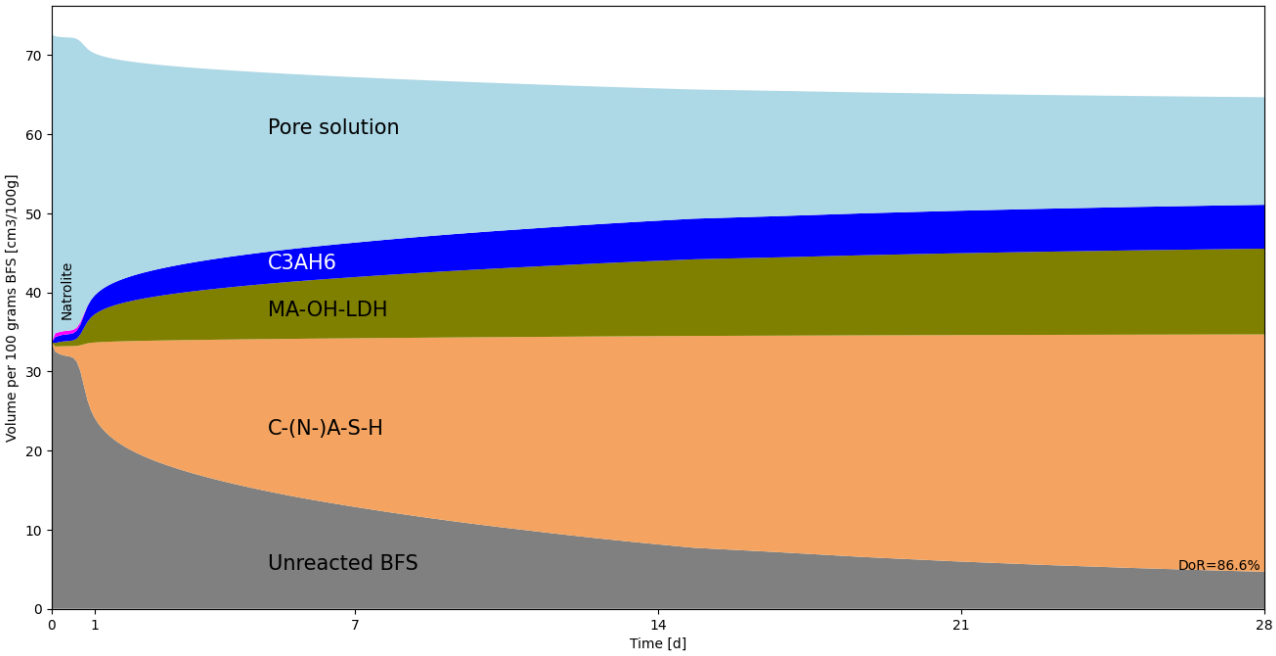

Figure 41: Formation of reaction products for mixture N4A0.66 during the first 28 days.

During the initial 20 hours, only a small fraction of natrolite is present. This natrolite subsequently transforms into C-(N-)A-S-H gel, as no other Na-containing phases are available and as demonstrated in 4.4, the formation of C-(N-)A-S-H gel commences only when the volume of natrolite begins to decline. Following the complete dissolution of natrolite, the reaction products are limited to C-(N-)A-S-H, hydrotalcite, and katoite until the 28 day mark. At 28 days, the degree of reaction for N4A0.66 is 86.6%, which is slightly lower than that of mixture N4REF.

The formation of reaction products during the first 28 days for mixture N4A2.02 is presented in Figure 42.

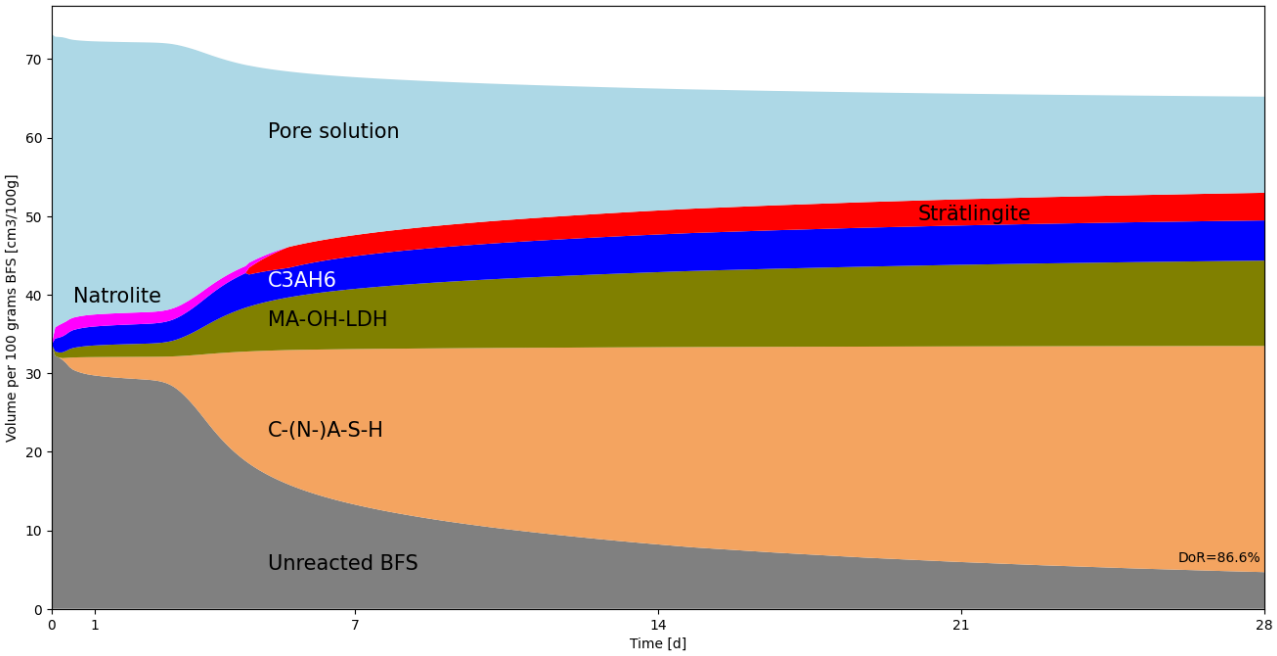

Figure 42: Formation of reaction products for mixture N4A2.02 during the first 28 days.

It is observed that natrolite remains present in the system for a longer duration compared to N4A0.66. In the first 6 hours, the volume of natrolite increases, after which it begins to decline, ultimately disappearing from the system at 131 hours. Notably, the formation of C-(N-)A-S-H gel initiates at 6 hours, precisely when the volume of natrolite starts to decrease, indicating that natrolite is being transformed into C-(N-)A-S-H.

At 101 hours, strätlingite begins to form, with its volume increasing until 131 hours, at which point it stabilizes at 2.65 cm^3/100 g BFS. This suggests that strätlingite and natrolite coexist in the system for approximately 30 hours. It can be observed that once natrolite is no longer present, the volume of strätlingite remains stable.

Between 101 and 131 hours, the volume of katoite decreases, but after 131 hours, it begins to increase again. This change indicates that a portion of katoite is being transformed into strätlingite. The increase in katoite after 131 hours correlates with the rise in the degree of reaction (DoR), as both exhibit a similar trend during this period. Throughout the entire 28-day period, the volumes of hydrotalcite and C-(N-)A-S-H increase linearly with the DoR. At 28 days, the degree of reaction is 86.6%, which matches that of mixture N4A0.66.

The formation of reaction products during the first 28 days for mixture N6REF is presented in Figure 43.

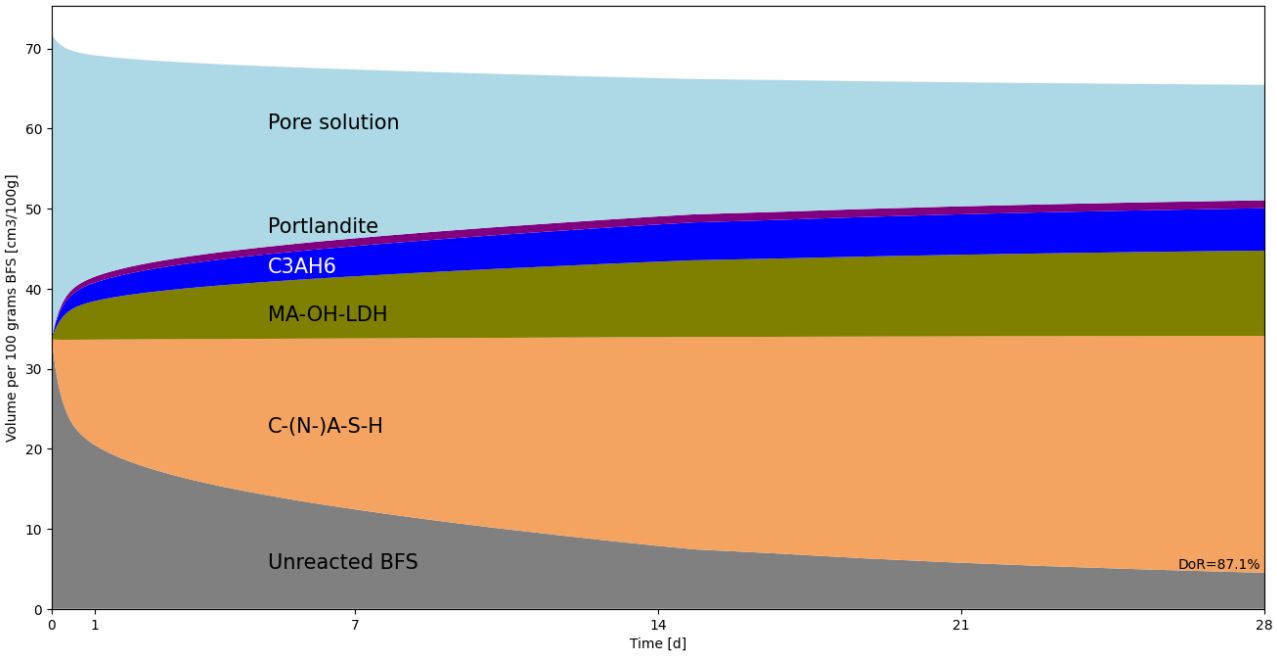

Figure 43: Formation of reaction products for mixture N6REF during the first 28 days.

In contrast to mixture N4REF, portlandite is present throughout the entire 28 days, rather than for only a few days. Its volume increases until 344 hours, after which it begins to decrease slightly. However, this decrease in portlandite volume after 344 hours is not significant, and it can be assumed to remain stable after 344 hours.

The prolonged presence of portlandite in this mixture, as opposed to its limited duration in N4REF, can be attributed to the increased pH of the activator. Since the solubility of portlandite decreases at higher pH levels (Bouzouaid et al., 2021; Provis & Bernal, 2014), it is reasonable to conclude that in the case of N6REF, portlandite dissolves only marginally and later in the reaction, once the hydroxide ions have been largely consumed by the ongoing reactions.

As for the other reaction products, their formation continues to increase linearly with the DoR, indicating that the increase in the volume of these products is solely dependent on the DoR and not influenced by the presence of other phases. After 28 days, the degree of reaction is determined at 87.1%, which is slightly lower than that of the N4REF mixture.

The formation of reaction products during the first 28 days for mixture N6A1.73 is presented in Figure 44.

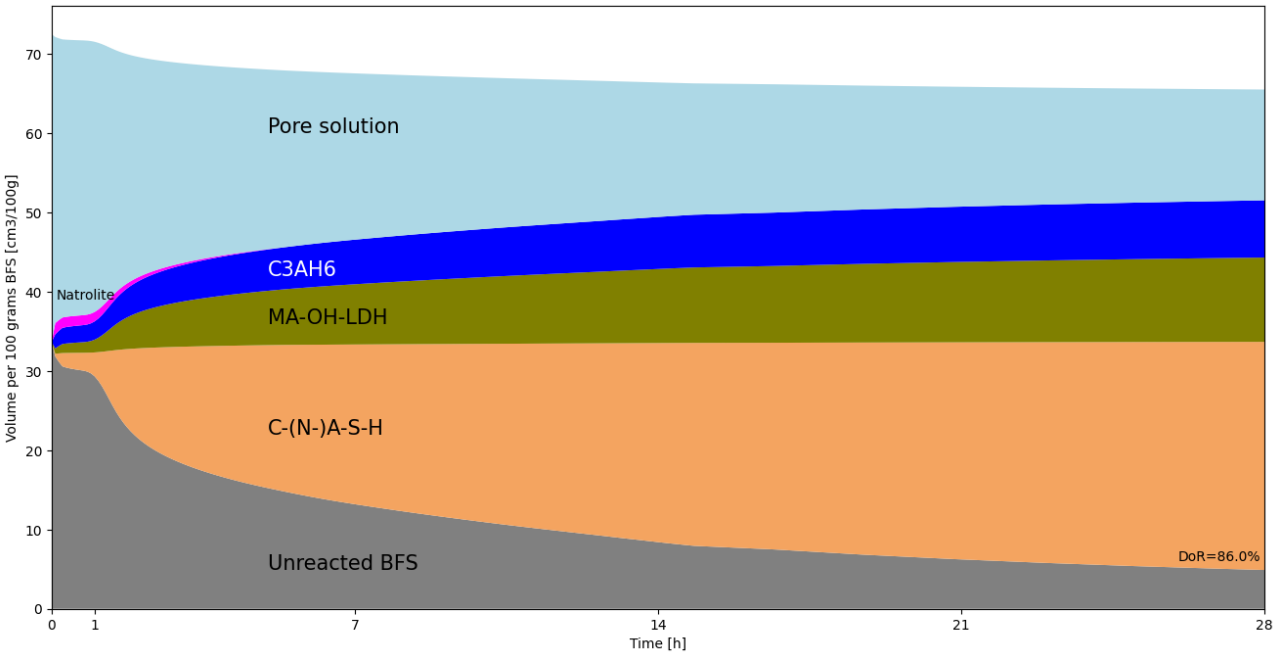

Figure 44: Formation of reaction products for mixture N6A1.73 during the first 28 days.

The trend for the degree of reaction in this mixture closely resembles that of N4A0.66, exhibiting slow reaction during the first day, followed by a noticeable acceleration. Similar to N4A0.66, natrolite is present in the early stages of the reaction. Its volume reaches a maximum after just a few hours, then begins to decrease in volume. natrolite is completely absent from the system after 129 hours.

Again the formation of C-(N-)A-S-H gel commences only when the volume of natrolite begins to decline, indicating that natrolite is being incorporated into the C-(N-)A-S-H gel. The increase in volume of the other reaction products is again solely correlated to the increase DoR. At the end of the 28-day period, the final DoR is determined at 86.0%, which is slightly lower than that of the previous mixtures.

The formation of reaction products during the first 28 days for mixture N6A3.04 is presented in Figure 45.

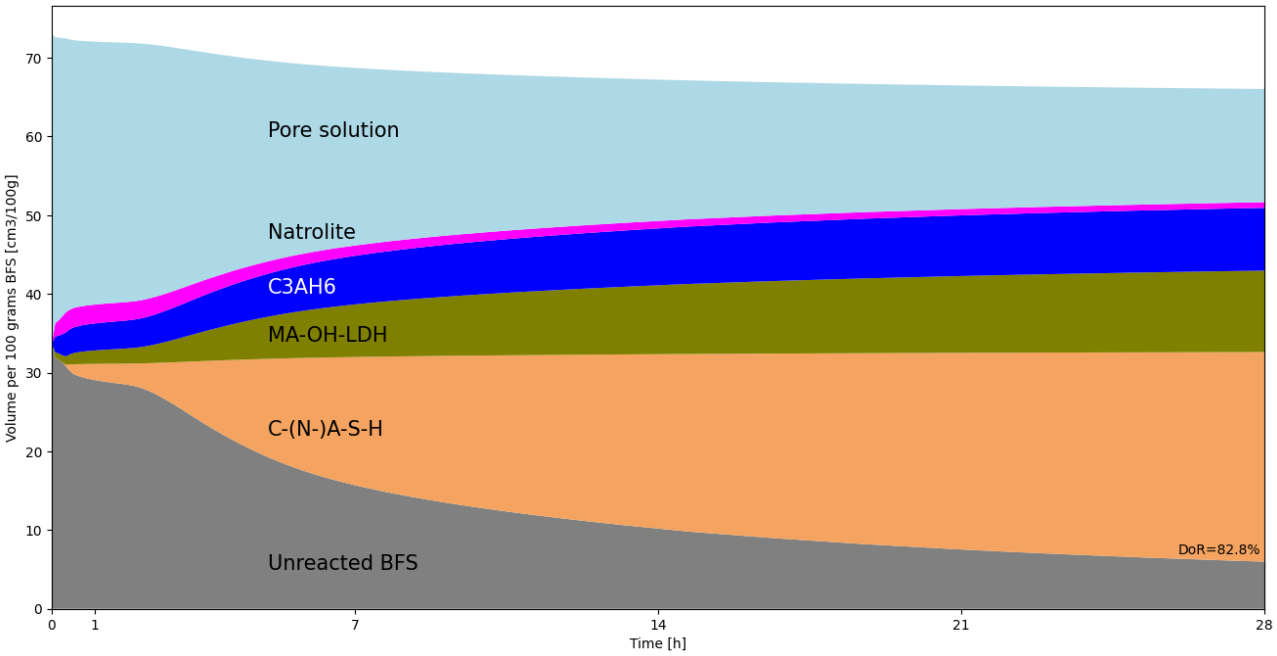

Figure 45: Formation of reaction products for mixture N6A3.04 during the first 28 days.

The trend of the DoR in this mixture resembles that of N4A2.02, displaying two distinct accelerations and a less steep curve compared to the reference mixtures, N4A0.66 and N6A1.73. Natrolite is present throughout the entire 28-day period, in contrast to its behavior in N6A1.73.

There is again a delay in the formation of C-(N-)A-S-H gel. The initiation of C-(N-)A-S-H formation coincides with the decrease in natrolite volume, occurring around 8 hours. At the conclusion of the 28-day period, the degree of reaction (DoR) for N6A3.04 is measured at 82.8%, the lowest DoR among all the mixtures.

The results indicate that the addition of dissolved Al to the activator has varying effects on the reaction process. When Al is introduced into the activator, a second peak is observable in the normalized heat evolution rate (see Figures 38 and 39). The presence of higher Al content in the activator influences these observed peaks in multiple ways.

Notably, the height of the first peak for N4A0.66 is considerably lower compared to the second peak, suggesting that minimal reaction occurs at this stage. In this context, the additional Al primarily retards the reaction, as evidenced by the cumulative heat release. Conversely, for mixtures with increased Al content, such as N4A2.02, N6A1.73, and N6A3.04, the total heat released is distributed more evenly over the entire time interval, rather than being concentrated in the early stages.

The time to the first peak (T_FP) and, when applicable, the second peak (T_SP), along with the corresponding peak heights (H_FP & H_SP) are shown in Table 19. Given that the Na_2O content varies among the mixtures, it is logical to assess the influence of Al based on the aluminium modulus (M_a) defined previously.

Table 19: Time to the first and second peak in hours and the height of the first and second peak in mW/g

Mixture	$\mathbf{M_a}$	$\mathbf{T_{FP}}$ **[h]**	$\mathbf{T_{SP}}$ **[h]**	$\mathbf{H_{FP}}$ **[mW/g]**	$\mathbf{H_{SP}}$ **[mW/g]**
N4REF	0	1.9	-	2.78	-
N4A0.66	0.1	3.1	17.8	0.28	2.17
N4A2.02	0.31	9.3	84.4	0.58	0.62
N6REF	0	1.3	-	3.55	-
N6A1.73	0.18	3.9	31.6	0.97	1.07
N6A3.04	0.31	9.1	73.8	0.79	0.41

The relationship between the aluminium modulus and the time to the first and second peaks is shown in Figure 46.

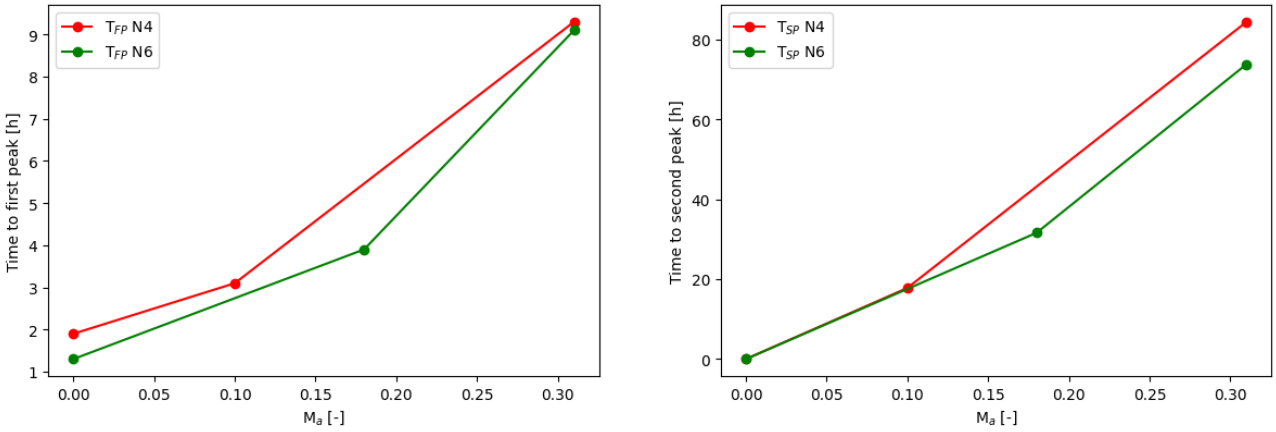

Figure 46: The time to the first and second peak of the mixtures against the aluminium modulus, M_a.

It is evident that the time to the first peak (T_{FP}) gets delayed when the Al_2O_3 content in the activator increases. Besides the Al_2O_3 content in the activator, the Na_2O content also influences the time to the first peak. As the Na_2O content increases, the time till the first peak decreases, as backed by literature (Liu et al., 2022). This explains that the T_{FP} for N6REF is lower than that for N4REF, and similarly, why N6A3.04 exhibits a lower T_{FP} compared to N4A2.02 while having the same value of M_a.

Furthermore, the time to the second peak (T_{SP}) is also correlated with the aluminium modulus of the activator. As the aluminium modulus increases, the T_{SP} correspondingly increases. Again, an increase in Na_2O content leads to lower values of T_{SP}, while having the same value of M_a.

Table 19 illustrates that the time interval between the peaks decreases with a lower M_a, suggesting a convergence of the two peaks into a single peak beyond a certain threshold value of M_a. Since the reference mixtures do not exhibit a second peak, both the time and peak height are recorded as zero. These data points are included to indicate that a threshold value of M_a likely exists between 0 and 0.1, where a second peak first appears.

In addition to affecting the timing of the first and second peaks, the Al content also influences the peak height of both. Figure 47 shows the heights of the first peak and, where applicable, the second peak plotted against the aluminium modulus (M_a).

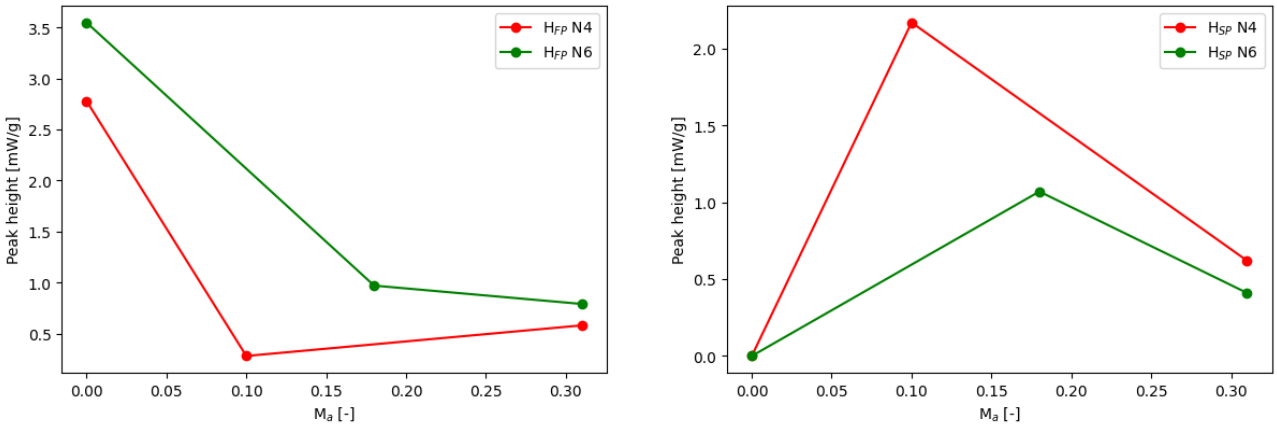

Figure 47: The height of the first and second peak of the mixtures against the aluminium modulus, M_a.

In the literature it is reported that the first peak could correspond to the formation of metastable phases, which later integrate into other reaction products (Liu, Tang, et al., 2024). Consequently, the first peak in mixtures with aluminium-containing activators does not directly correlate with the first peak in the reference mixtures, as no metastable phases are formed in the latter.

The metastable phase responsible for the additional peak in the calorimetry results can be identified through GEMS modelling. Natrolite appears to be the metastable phase, as it is the only phase that forms and subsequently disappears in mixtures with aluminium-containing activators. This suggests that a higher formation of natrolite, as indicated by GEMS results presented in this section, would correspond to a greater heat release during the first peak.

The higher first peaks for a higher Al content in Table 19 supports this correlation; however, mixture N6A1.73 exhibits a higher first peak magnitude compared to N6A3.04, despite GEMS indicating a greater early-stage natrolite formation for N6A3.04. An examination of the heat evolution rate in Figure 39 shows that the first peak for N6A3.04 is broader, suggesting a higher cumulative heat associated with this peak. The cumulative heat release further supports that the heat released in the first peak correlates with early-stage natrolite formation, as suggested by GEMS. This connection also serve as strong evidence that the first peak is related to the formation of metastable phases, identified as natrolite in the modelling.

The formation of natrolite in the early stages aligns with expectations, given that the dissolution rate is likely slowed by the presence of Al and low Si content in the activator. As natrolite comprises only elements already present in the activator, its formation is less dependent on rapid dissolution rates. These findings suggest that, beyond a specific threshold M_a value, metastable phases cease to form.

Following the first peak, an induction period begins, characterized by minimal reaction activity between the two peaks. During this phase, aqueous Al passivates the Si sites on the unreacted BFS, preventing hydroxide ions from accessing the BFS grains and thereby retarding the geopolymerization process (Zuo, 2019). Alongside Si passivation, a gel layer forms due to reactions between silicates and aluminates, creating an additional barrier around the BFS particles that restricts pore solution contact with the unreacted BFS, further inhibiting dissolution and the geopolymerization process (Liu, Tang, et al., 2024).

The induction period is followed by acceleration and deceleration phases, where the passivating layer and barrier gel around the slag particles begin to dissolve and become permeable again, allowing the pore solution to contact the anhydrous particles. As dissolution resumes, reaction products can form, marking the second peak, which reflects accelerated dissolution and subsequent reaction product formation.

The time required to transition through the induction period is not directly defined by, but correlates with, the interval between the first and second peaks. For mixtures with lower M_a values, this interval shortens, indicating less passivation due to a reduced concentration of aqueous Al. A lower M_a also results in a thinner gel layer, which, by decreasing the barrier effect, allows for an easier acceleration of reaction, thereby shortening the induction period. This reduced passivation and gel barrier also leads to a more rapid reaction acceleration after

the induction period, producing a sharper and narrower second peak. The relationship between M_a, passivation, and induction period length is supported by data in Figures 46 and 47, as well as in Table 19.

For mixtures with lower M_a values, this induction period between the first and second peak shortens, suggesting less passivation and a lower amount of natrolite forming in these mixtures due to a reduced concentration of aqueous aluminium. Reduced passivation leads to a more rapid reaction acceleration after the induction period, resulting in a sharper and narrower second peak. This relationship is confirmed by the data in Figures 38 and 39, as well as in Table 19.

Over time, the aqueous solution loses its capacity to overcome the activation energy barrier, as Na and OH ions are gradually consumed throughout the reaction. This consumption leads to a deceleration phase, eventually reaching a stable phase where no further dissolution occurs (Zuo, 2019; Liu, Tang, et al., 2024). In the follow-up section, this phenomenon is further examined by analyzing trends in elemental concentrations in the pore solution, which may provide additional confirmation of this progression.

5.2.3 Pore solution chemistry

The results for each element are presented individually, with Al, Si, and Ca displayed separately. Na and OH are plotted together due to their correlated behavior. Additionally, the mixtures containing 4 wt.% and 6 wt.% Na_2O are presented separately, as the variations in Na_2O content resulted in differing concentrations due to variations in alkalinity.

The experimental concentrations of Al, Si, Ca, Na and OH for the mixtures with 4 wt.% of Na_2O can be seen in Figure 48.

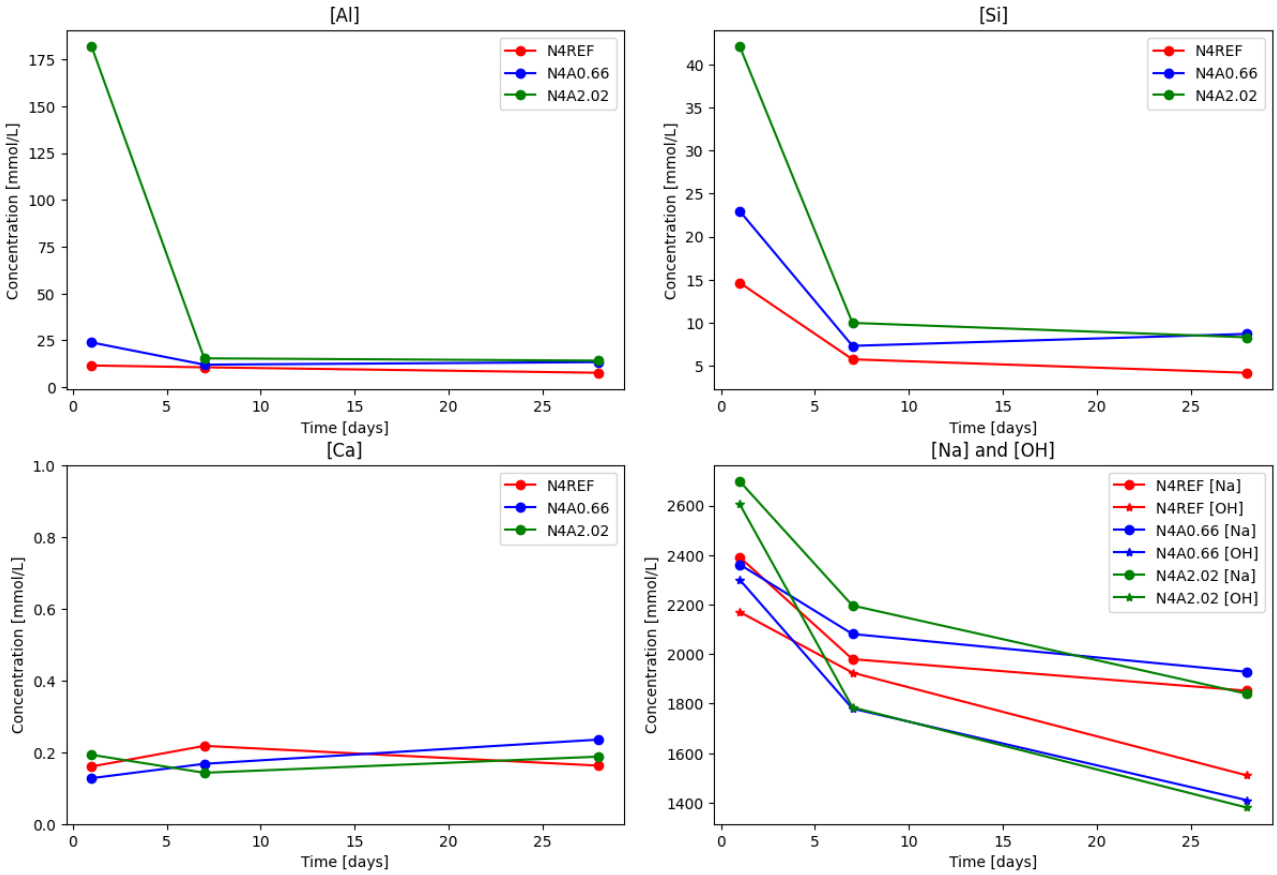

Figure 48: Experimental concentrations of the elements in the pore solution for the mixtures with 4 wt.% of Na_2O.

All elements showed a downward trend in concentration, with the steepest decline between 1 and 7 days as most of the reaction is concentrated in that time frame. The Ca concentration was very low during the entire reaction and little variation within this concentration can be observed.

The experimental concentrations of Al, Si, Ca, Na and OH for the mixtures with 6 wt.% of Na_2O can be seen in Figure 49.

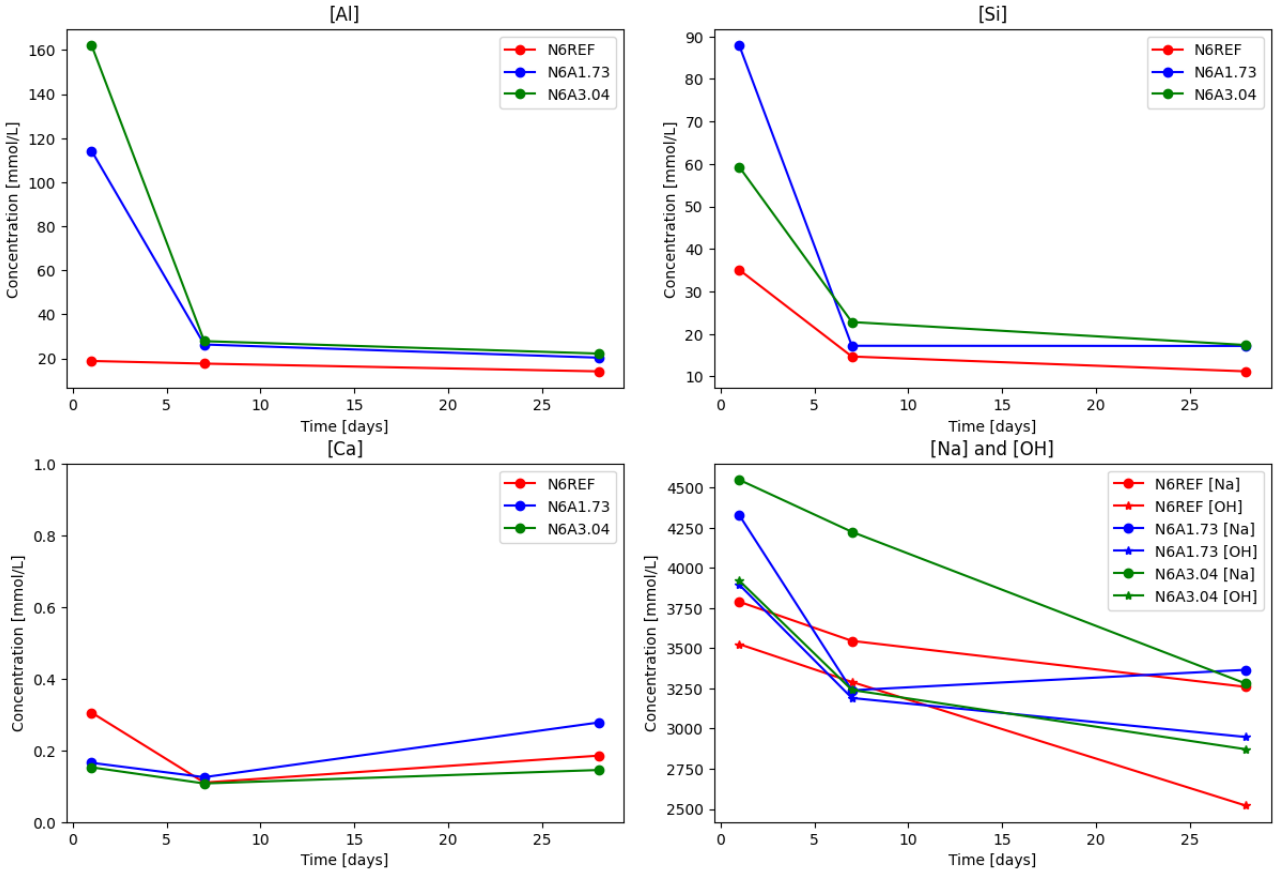

Figure 49: Experimental concentrations of the elements in the pore solution for the mixtures with 6 wt.% of Na_2O.

For all elements a downward trend in concentration can be observed, with the steepest decline between 1 and 7 days as most of the reaction happened in that time. Again, the Ca concentration was very low during the entire reaction and little variation within this concentration was observed. It has to be noted that for mixtures N6A1.73 and N6A3.04, there was too little pore solution extracted to perform both titration and ICP. Therefore, the hydroxide concentration is determined by measuring the Na content as there was a linear relationship between the two elements. The linear relationship can be seen in Appendix C.

Besides the experimental concentrations, the concentrations in the pore solution were also modelled using GEMS. As it was not possible to model the concentration of hydroxide ions in the pore solution, only the Na concentrations are modelled. The modelled concentrations for the mixtures with 4 wt.% of Na_2O can be seen in Figure 50.

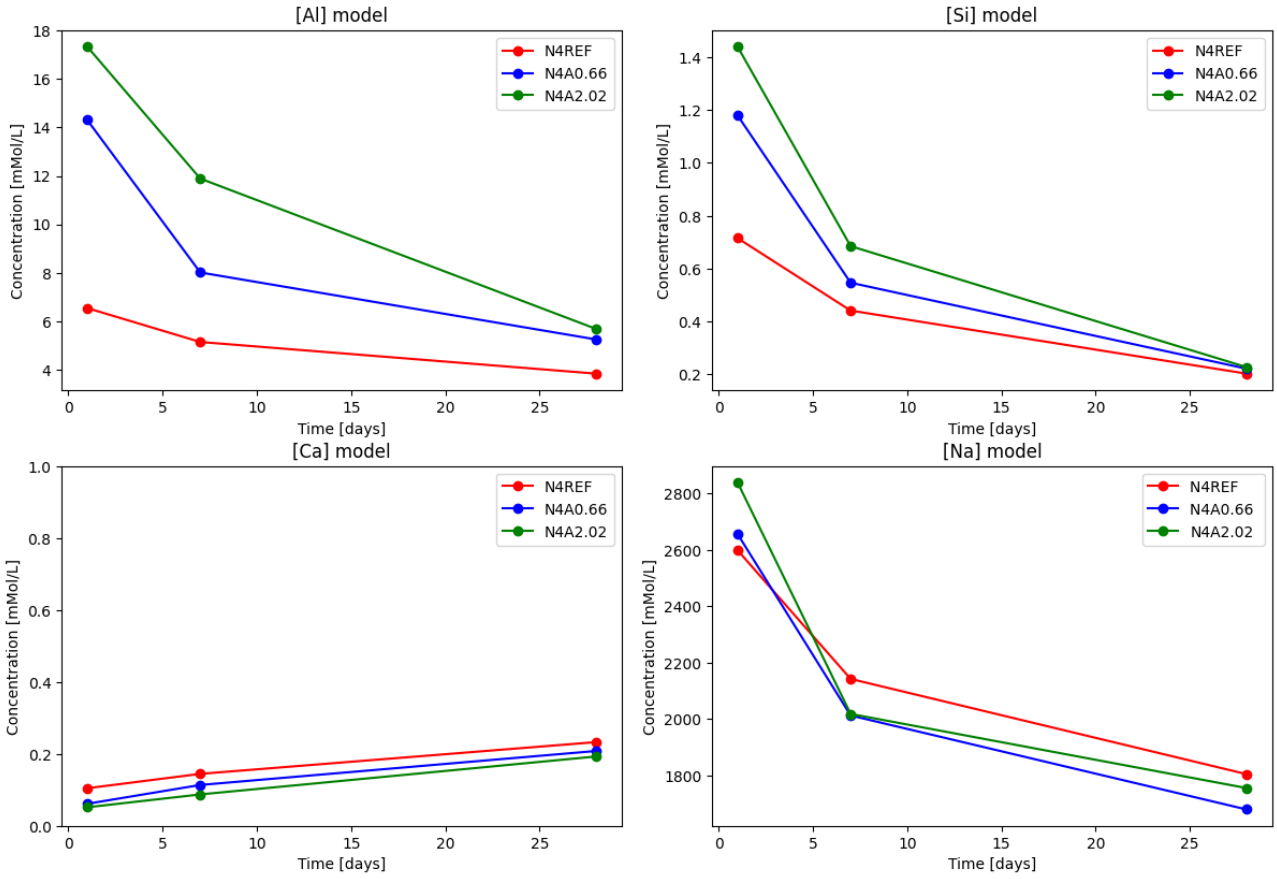

Figure 50: modelled concentrations of the elements in the pore solution of the mixtures with 4 weight percent of Na_2O.

In the model, decreasing trends for Al, Si, and Na concentrations in the pore solution are also observed, with Ca levels remaining consistently low throughout the reaction. While the overall trends in the model agree well with the experimental data, there are some differences in the concentration magnitudes between the model and experimental results.

The modelled concentrations for the mixtures with 6 wt.% of Na_2O can be seen in Figure 51.

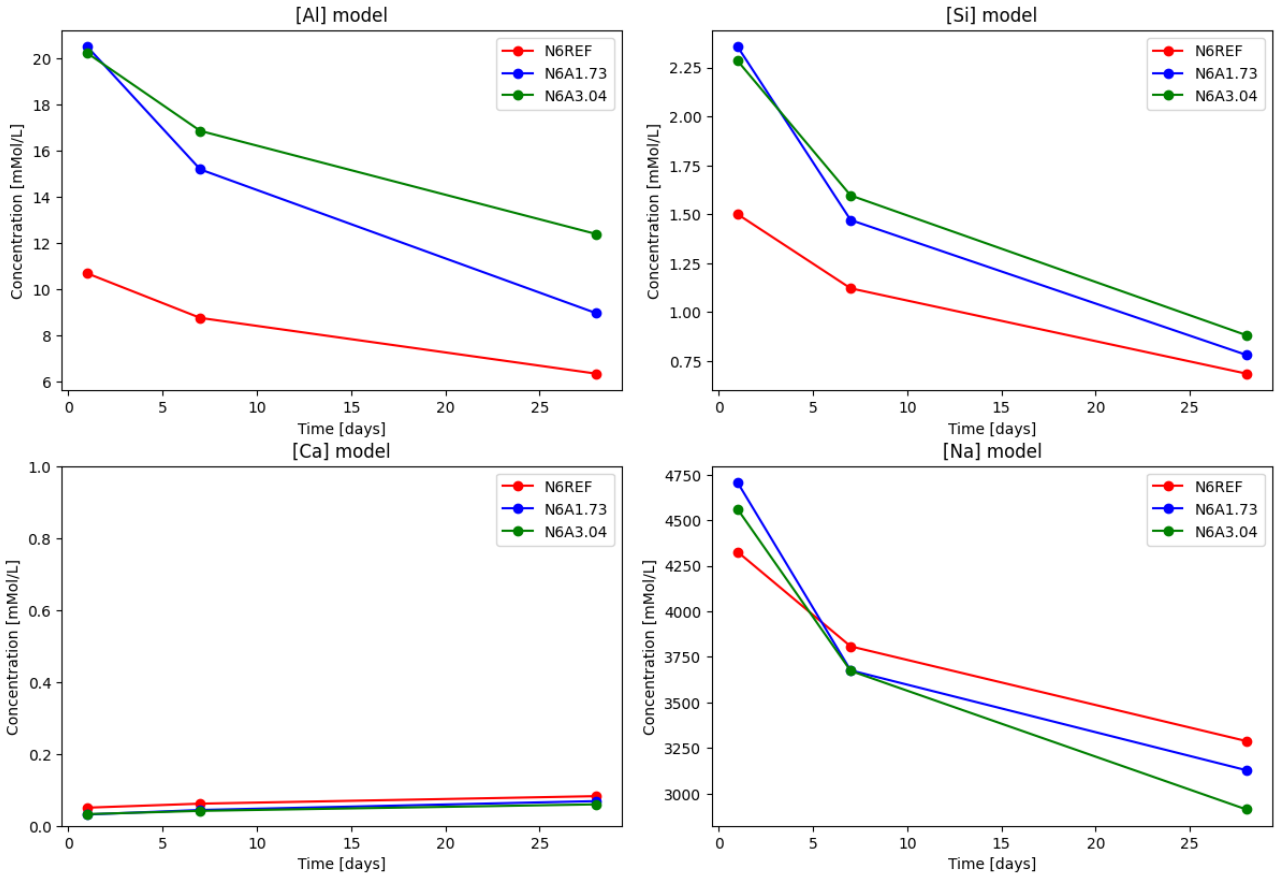

Figure 51: Modelled concentrations of the elements in the pore solution of the mixtures with 6 weight percent of Na_2O.

Again, a decreasing trend for Al, Si and Na can be seen and the concentration of Ca is also very low during the entire reaction. Also for these mixtures, the element concentration following GEMS modelling are similar to the experimental data, but the magnitude of the concentrations show differences from the experimental data.

The results indicate that the trends in elemental concentrations in the pore solution over time are quite similar between the experimental and modelling data, although the concentration magnitudes differ significantly. Given that the model assumes ideal reaction conditions and complete precursor dissolution, some variation from the experimental data is expected.

An explanation for the significant higher Al concentration for N4A2.02 and N6A3.04 after 1 day between the experimental and modelling data is that the model always has 100% perfect theoretical precipitation of reaction products based on the input that is presented to the model. Initially there is a lot of Al, Na and Si available as it is present in the activator so the model predicts natrolite formation that consumes those elements. However, in reality the aluminium rich alkaline solution also contains additives which prohibits the crystallization of zeolites, such as natrolite.

Another imperfection of the model which could influence the outcome is that the dissolution of blast furnace slag is always assumed to be similar for all components within the slag. In reality the dissolution of the different components of the blast furnace slag happens in different degrees as the dissolution of Ca, Al and Si are all dependent on different parameters as discussed in section 5.2.1. However, as the trend of the model is similar as that of the experimental data, the model can be used to explain certain observations.

The experimental concentrations of the mixtures containing 4 wt.% of Na_2O show that after 1 day, the mixture N4A2.02 has the highest concentrations of Al, Si and Na. Given that that this mixture has the lowest degree of reaction after 1 day, the elevated concentrations after 1 day are expected. Al, Si and Na are already present in the aqueous solution due to the addition of the Al etching solution and remain in a dissolved state due to low reaction rate at this stage.

5.2.4 Discussions

Now that the results and discussions of each experiment have been presented, this section discusses connections between them regarding the reaction process.

Dissolution - Isothermal calorimetry
The dissolution test in this research was not able to quantify the influence of the Al etching solution on the dissolution of BFS. However, the literature indicates that the presence of Al and Si in this solution slows the dissolution rate of both Al_2O_3 and SiO_2 of the BFS.

Together with the assumption above, the isothermal calorimetry provided some evidence of the slow dissolution rate of the BFS. The normalized heat release of the etching solution containing mixtures showed an additional peak, related to the formation of metastable phases which create a gel barrier around BFS particles, preventing further dissolution of the precursor. The formation of the metastable phases was confirmed by using the DoR data in the GEMS model.

Besides the formation of a gel barrier, an overall retardation of the dissolution was observed due to the passivation of the BFS particles by the dissolved Al in the solution, originating out the etching solution. This retardation led to a delay in achieving the first peak and overall the heat of reaction was more evenly distributed over time, leading to less intense, but broader peaks.

Isothermal calorimetry - Pore solution chemistry
In the results of the pore solution chemistry it was found that mixture N4A0.66 has a relatively low concentration of Al after 1 day compared to N4A2.02, considering the content of Al in the activator. This significant difference in Al concentration can be explained by the results found in the isothermal calorimetry.

In the isothermal calorimetry the time required to reach both the first and second peak were described. For mixture N4A0.66, the time till the second peak (T_{SP}) is reached at 17.8 hours. This means that the acceleration of the reaction happened within the first day. In contrast for mixture N4A2.02, T_{SP} takes 84.4 hours, meaning the reaction acceleration occurs after 1 day, but before the 7 day mark. The reaction acceleration will consume elements in the pore solution, explaining why the concentrations are lower for N4A0.66 compared to N4A2.02 after 1 day.

Since the reference mixture contains no Al or Si in the activator, it understandably shows the lowest concentrations of these elements after one day. Additionally, the reference mixture has the highest degree of reaction after one day, corresponding with the concentrations of OH and Na. As Na and OH are consumed in the reaction, it follows that the mixture with the highest degree of reaction has the lowest concentrations, or biggest decrease, of these elements.

By 7 days, the concentrations of Al, Si, and Na have dropped significantly across all mixtures, with the steepest decreases observed in N4A2.02 and N4A0.66. This aligns with the calorimetry results, where the second peak appears between days 1 and 7 for N4A2.02, indicating accelerated reaction during this period and consequent consumption of these elements. Beyond 7 days, minimal reaction occurs, leading to relatively stable concentrations and suggesting the mixtures are entering the stable phase. The concentration of Ca remains consistently low and stable throughout, as dissolved Ca readily reacts with abundant elements in the pore solution.

For the mixtures containing 6 wt.% of Na_2O, similar observations can be made. After 1 day the concentrations of Al are the highest for the mixtures which contain the Al etching solution.

An interesting observation after the first day is that the concentration of Si is higher in N6A1.73 compared to N6A3.04. Given that a small amount of Si is present in the etching solution, one might expect N6A3.04 to have a higher Si concentration after one day due to the greater initial Si content. However, the measured degree of reaction (DoR) after one day is slightly higher for N6A3.04, indicating that more reaction has occurred, which explains the lower Si concentration in this mixture. Since the magnitude of Al concentrations is significantly higher than that of Si, this slight increase in DoR does not bring the Al concentrations of N6A3.04 below those of N6A1.73.

In the modelled data, both Al and Si concentrations are lower for mixture N6A3.04 than for N6A1.73. Without a complexing agent in the model, a higher number of metastable phases can form compared to actual conditions. Along with the higher degree of reaction observed in N6A3.04 after one day, this leads to reduced Al and Si concentrations in the model for N6A3.04.

After one day the degree of reaction is highest for N6REF, which also has the lowest Na and hydroxide concentrations after 1 day. When time proceeds, the Na and hydroxide keep decreasing for the mixtures and N6A1.73

and N6A3.04 showed a great decrease in those elements between 1 and 7 days, which correspond with the reaction acceleration described in the calorimetry. It can be observed that the concentration of Na increases after 7 days for N6A1.73. As the reaction consumes the Na, it would be expected to observe a decrease of these elements, as shown in the model. As the hydroxide concentration is dropping and the model also predicts a decrease of Na it could be the case that this value is a measurement error or error due to extraction.

5.3 Conclusions

The experimental study of the reaction process revealed several key findings regarding the influence of the etching solution on the material's performance. This section presents the key findings discussed in this chapter.

- It was found that the etching solution influences the dissolution of BFS by passivating the particles and likely by creating a gel barrier around the particle which exist out of a metastable phase, which the modelling indicates to be natrolite.
- The amount of etching solution added to the mixture significantly influenced its heat release profile. The introduction of the etching solution resulted in an additional peak in the normalized heat release, likely attributed to the formation of these metastable phases as indicated by the literature.
- The contents of both Na_2O and Al_2O_3 influenced the characteristics of the peaks in the normalized heat release. A higher Na_2O content accelerated the heat release, reducing the time to reach both the first and second peaks. In contrast, an increased Al_2O_3 content resulted in a higher heat release in the first peak. The addition of Al_2O_3 also extended the time required to achieve the first peak, likely due to the passivation of BFS particles, as well as the time to the second peak because of the increased gel barrier formation as indicated by the literature.
- The maximum cumulative heat released increased with higher M_a values, indicating greater potential heat release and, consequently, enhanced formation of reaction products of these mixtures.
- The pore solution chemistry supported these observations, confirming the delayed reaction in mixtures containing the etching solution, as well as the significant reaction acceleration that occurred between days 1 and 7 for these mixtures.

6 Experimental study on fresh and hardened properties

This chapter explores the fresh and hardened properties of the mixtures, focusing on setting time and mechanical strength development. Understanding these properties is crucial for assessing the practical performance and durability of the material in structural applications. The setting time is evaluated to determine how the activator composition influence the materials handling and application. Hardened properties, including compressive and flexural strength, are studied at different curing ages to assess the development of mechanical stability over time. This chapter aims to link activator composition with observed performance, providing insights into optimizing alkali-activated systems for practical use.

6.1 Materials and methods

6.1.1 Materials and mixtures

The slag and activator components used in this chapter are the same as used in Chapter 5. The mixtures designed in Section 4.3 were also used in this chapter to investigate the fresh and hardened properties. A recap of the mixture designs that were used is shown in Table 20.

Table 20: Recap of the mixture designs.

Mixture	BFS [g]	$water$ [g]	Na_2O [g]	Al_2O_3 [g]	M_a [-]
REFN4	100	40	4	0	0
N4A0.66	100	40	4	0.66	0.10
N4A2.02	100	40	4	2.02	0.31
REFN6	100	40	6	0	0
N6A1.73	100	40	6	1.73	0.18
N6A3.04	100	40	6	3.04	0.31

6.1.2 Setting time

The setting time was measured by performing the Vicat needle test. The apparatus is an automated version of the Vicat needle test. For a defined time interval, the Vicat needle dropped into the mixture in a conical mold and sealed with thin plastic foil to avoid drying of the mixture. The height of the conical mold is 40 mm in total and thus the maximum penetration is 40 mm. The initial setting time is defined by the time that is needed to achieve a penetration of 36.5 mm and the final setting time is achieved when there is only a penetration of 1 mm. The experiment is a slight adjusted version of NEN-EN 196-3 as there is standard error on the set-up as the penetration does not start from exactly the top of the mold, meaning there is always a penetration bigger than 0.5 mm.

6.1.3 Strength

Both flexural and compressive strength tests were performed in accordance with NEN-EN 196-1. For the flexural test, the samples were subjected to a 3-point bending setup with a span of 100 mm and a load increment of 50 N/s until failure. It is important to note that while the prism length is 160 mm, the correct span length for calculations is 100 mm. The testing machine calculates stress using the incorrect length, and this discrepancy must be accounted for in the results.

Following the flexural test, the broken halves of the prisms were used for the compressive strength test. The samples were placed on a 40 mm by 40 mm plate and compressed by an identical plate. The loading rate was 2400 N/s, and the compressive strength was determined by dividing the failure load by the area of the loading/supporting plate.

6.2 Results and discussion

6.2.1 Setting time

The initial and final setting time of the mixtures can be seen in Figure 52. The blue bar represents the initial setting and the orange bar represents the final setting time.

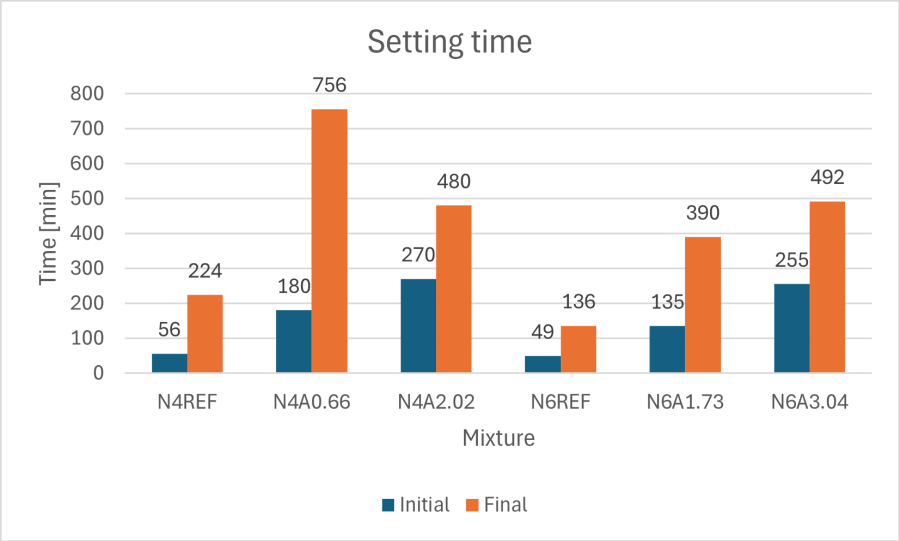

Figure 52: Setting time of the different mixtures

The mixtures that contain the etching solution have significantly higher setting times compared to the reference mixtures. Overall, the mixtures with a higher content of Na_2O, experience shorter setting times. It can be concluded that the initial setting time increases with an increase of M_a. However, the influences of Na_2O and Al_2O_3 on the initial setting time are not equal. The content of Na_2O seems to have a higher effect on the initial setting time than the aluminium content as mixture N6A1.73 has a shorter initial setting time, but a higher M_a compared to N4A0.66, indicating that the Na_2O content has more influence on the initial setting time.

For the mixtures containing 6 wt.% of Na_2O, a similar trend is found for the final setting time. The final setting time increases with the content of etching solution in the mixtures. However, for the mixtures containing 4 wt.% of Na_2O, the final setting time for N4A0.66 is significantly higher compared to N4A2.02, which is deviating from the trend observed in the initial setting time and final setting time for mixtures with 6 wt.% of Na_2O. The explanation for this deviating trend is discussed in the discussion in the follow-up section.

6.2.2 Strength

The compressive strength of the mixtures at 1, 7 and 28 days is shown in Figure 53.

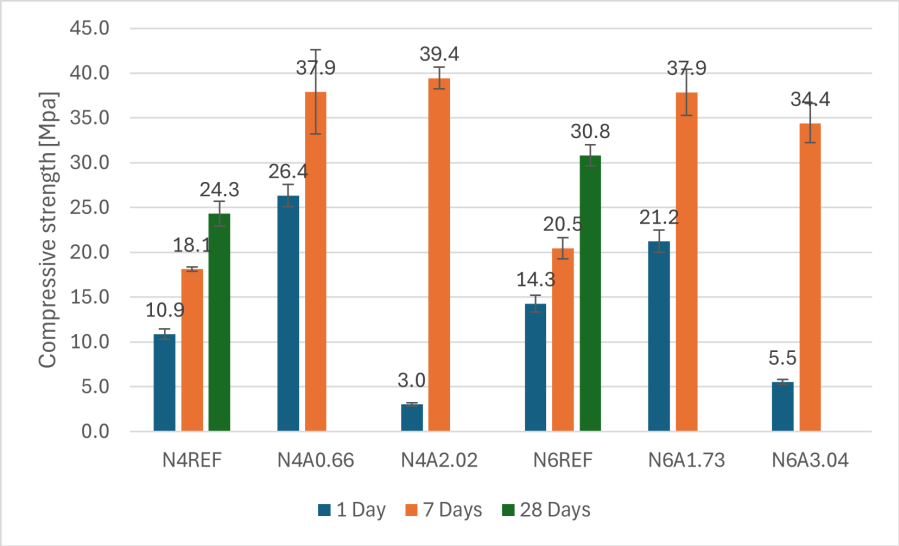

Figure 53: Compressive strength of the mixtures with the standard deviation as errorbar

The results show that the content of aluminium in the activator has a significant impact on the strength development of the mixtures. It can be seen that for mixtures which are designed based on the thermodynamic modelling in GEMS (N4A0.66 and N6A1.73), the compressive strength is significantly higher after just one day compared to the other mixtures. Mixtures N4A2.02 and N6A3.04 to the contrary show extremely low compressive strength after just one day. After 7 days, all the mixtures containing etching solution show superior compressive strength compared to the reference mixtures, indicating that the aluminium in the activator benefits the strength development.

The flexural strength of the mixtures at 1, 7 and 28 days is shown in Figure 54.

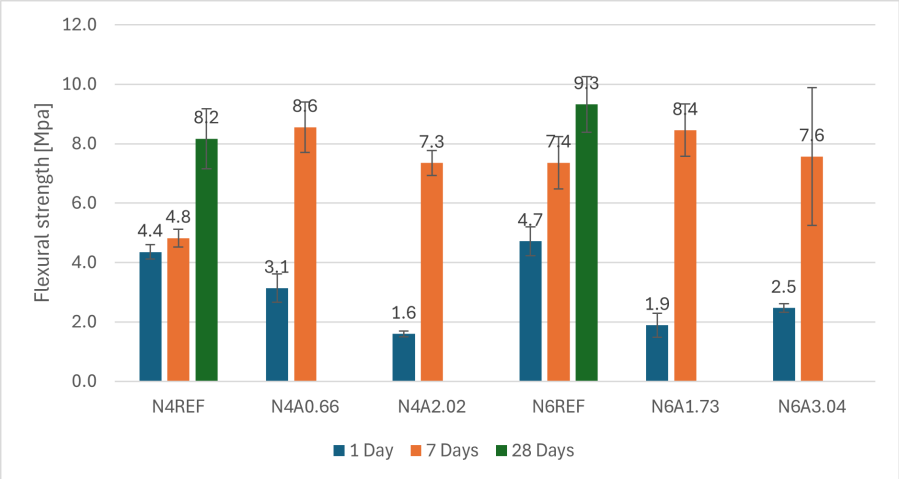

Figure 54: Flexural strength of the mixtures with the standard deviation as errorbar

The flexural strength results follow a trend similar to the compressive strength outcomes. However, unlike the compressive strength, the flexural strength of N6A3.04 is slightly higher than that of N6A1.73. This could be due to the rapid strength gain after the first day, which may have induced tensile stresses in the material due to shrinkage, reducing the tensile strength achieved in mixtures with the etching solution.

The 28 day strength is missing for the mixtures that contain the etching solution. As the specimens were curing, the specimens cracked spontaneously somewhere between 7 and 28 days. As the specimens cracked before 28 days, it was not possible to test the specimens on strength for at this time.

6.2.3 Discussion

The results regarding the fresh and hardened properties allow for a connection to be established with the reaction process. This section discusses the relationships between both the setting time and strength in relation to the findings from the experimental study of the reaction process.

Setting time - Reaction process
The results of the setting time indicated that mixture N4A0.66 deviated from the expected relationship between setting time and M_a. By analyzing the heat evolution rate of the mixtures during the early stages, it may be possible to establish a connection that explains the extended final setting time observed for N4A0.66.

Appendix E, illustrates the setting times as vertical lines in the heat evolution rate graphs for the corresponding mixtures. For the reference mixtures, the initial setting time is observed just before the first peak, while the final setting time occurs shortly after. An increase in Na_2O content shifts this first peak to the left, resulting in earlier setting times for both stages. In the cases of mixtures N4A0.66 and N6A1.73, the initial setting time also occurs just before the first peak. Notably, the height of the first peak for N4A0.66 is significantly lower than that of N6A1.73. However, this difference does not substantially affect the initial setting time. As with the reference mixtures, an increase in Na_2O content leads to a shorter initial setting time for N6A1.73.

The first peak is significantly higher for N6A1.73 than for N4A0.66, indicating that the final setting time for N6A1.73 is reached immediately after the first peak, similar to the reference mixtures. In contrast, the final setting time for N4A0.66 is attained only when the induction period has passed and reaction accelerates again.

The mixtures N4A2.02 and N6A3.04 exhibit similar curves, with the increase in Na_2O content causing the graph for N6A3.04 to shift to the left. In both mixtures, the initial and final setting times occur before the first peak. This is attributed to the wide nature of the first peaks for both N4A2.02 and N6A3.04, resulting in a high cumulative heat release despite a relatively low peak height.

Strength - Reaction process
The results of the strength development, showed that mixture N4A2.02 and N6A3.04 have a significantly slower strength development and the mixtures N4A0.66 and N6A1.73 showed faster strength development compared to the reference mixtures. The strength development is strongly related to the results found in the experimental study of the reaction process, presented in Chapter 5.

The normalized heat release showed that for mixture N4A0.66, both the first and second peaks occur within the first day. In contrast, for mixture N6A1.73, the time to reach the second peak is 31.6 hours, with an increase toward this peak beginning around 20 hours. This suggests that the acceleration of the reaction following the induction period is also achieved within the first 24 hours for mixture N6A1.73. For mixtures N4A2.02 and N6A3.04, only the first peak was reached within the first day, which is associated with the formation of metastable phases. After one day, both N4A2.02 and N6A3.04 entered the induction period, characterized by minimal reaction activity. The absence of reaction acceleration during this phase, results in a low degree of reaction, explaining the reduced compressive strength observed after one day. In contrast, mixtures N4A0.66 and N6A1.73 experienced a higher DoR after 1 day due to the reaction acceleration, explaining the higher strength development at this stage.

After 7 days, all the mixtures have reached their second peak and the reaction starts to slow down. The mixtures have a similar DoR at this point of around 61%, except for N6A3.04, which has a lower DoR of 53%. This reduced DoR in N6A3.04 corresponds to its lower compressive strength compared to other mixtures containing the etching solution. The reference mixtures show a DoR of approximately 63-65%, comparable to the other mixtures. The lower compressive strength in the reference mixtures, despite similar DoR values, likely results from differences in the reaction products or microstructure formed.

Besides the relation between the strength and the normalized heat release, the strength can also be related to the consumption of elements in the pore solution, shown in Section 5.2.3. The acceleration of the reaction for mixtures N4A2.02, N6A1.73 and N6A3.04 between 1 and 7 days can also be validated by the high decrease of elements between 1 and 7 days.

The consumption of Na and OH in the pore solution shows a connection to strength development. For mixtures with 4 wt.% of Na_2O, both N4REF and N4A0.66 exhibit similar Na and OH concentrations after 1 day, which are notably lower than those in N4A2.02. At this point, N4REF and N4A0.66 also have higher compressive strengths compared to N4A2.02. By 7 days, N4A2.02 has undergone the reaction acceleration, resulting in a significant decrease in OH concentration. The OH concentrations in N4A0.66 and N4A2.02 are now similar and lower than in N4REF, suggesting greater reaction progress. This reduction in OH correlates with the higher

compressive strengths observed in N4A0.66 and N4A2.02, indicating a link between OH concentration in the pore solution and compressive strength.

For mixtures containing 6 wt.% of Na_2O, a similar relation to Na and OH concentrations is observed. A sharp decline in concentration of the elements occur between 1 and 7 days. However, the trend described for mixtures with 4 wt.% of Na_2O, doesn't fully hold here. Unlike the consistent decrease in OH concentration after 7 days across all 4 wt.% Na_2O mixtures, the OH concentrations for mixture N6REF decrease significantly more after 7 days compared to N6A1.73 and N6A3.04. It's important to note that the OH levels for N6A1.73 and N6A3.04 at 28 days are based on linear extrapolation, so this trend cannot be fully confirmed. While the Na trend is broadly similar to that of the 4 wt.% Na_2O mixtures, N6A1.73 shows an increase in Na concentration after 7 days, likely indicating Na release into the pore solution, most probably due to natrolite dissolution.

Crack formation
The presence of cracks in the mixtures containing the Al etching solution raises questions about the mechanisms driving their development. Based on the results and prior studies, several contributing factors have been identified. A broken sample due to the crack formation after 28 days is shown in Figure 55.

Figure 55: Prism samples after 28 days, showing severe cracking.

In the experiments it was observed that the mixtures containing the Al etching solution experienced severe shrinkage compared to the reference mixtures. The shrinkage was observed upon collecting the samples for the pore solution. The samples of the reference mixtures were stuck in the plastic cup, while the Al rich mixtures were very loose in the cup and could even be shaken around.

Besides that it was observed that mixture N4A0.66 did not crack after 28 days once submerged. Combining these two observations, which were not part of an experimental program, suspicion that the crack formation is shrinkage related grew. The main suspicion is that the crack formation is autogenous shrinkage related and thus related to the reaction kinetics. In the literature it is reported mixtures containing higher contents of fly ash (FA) in a sodium silicate activated BFS/FA mixture, showed less autogenous shrinkage (Z. Li, Zhang, Liang, & Ye, 2020). As FA is less reactive compared to BFS, it indicated that the autogenous shrinkage is higher for more reactive mixtures. Besides the lower autogenous shrinkage, the elastic modulus of mixtures containing FA, develop more slowly over time (Z. Li et al., 2020). This means that internal stress build up, related to autogenous shrinkage develops more slowly in the early age. This research indicates that the high reactivity of BFS could lead to an increased autogenous shrinkage and thus stresses which can cause cracks.

As the reference mixtures in this research don't show any cracking, it is expected that an increase of the Al etching solution increases the reactivity of the mixture, which is in line with the strength results shown as well as the maximum cumulative heat release shown in Section 5.2.2.

In another study where an Al etching solution is used as activator as well, mixtures with a mix of FA and BFS as precursor were used (Nugteren, 2010). One of the most similar mixtures that was used is shown in Table 21. This mixtures equals a water to binder ratio of approximately 0.39, a Na_2O content of 6.38 wt.% and an Al_2O_3 content of 3.78 wt.%, which is roughly equal to N6A3.04.

Table 21: Mixture used in the research of Nugteren.

FA [g]	**BFS** [g]	**water**[g]	**NaOH** [g]	**Rinse bath solution** [g]
30	15	1.25	2.1	17.5

As no crack formation was reported for the mixture shown in Table 21, it seems that replacing BFS with FA could prevent the crack formation as the total reactivity of the solid precursor is decreased and thus the stresses related to autogenous shrinkage.

This would mean that the total reactivity of the mixture is determined based on the BFS content in the precursor and the content of Al etching solution in the activator. When the reactivity becomes too high, autogenous shrinkage could lead to stresses which cause cracks.

As the literature reported that a mixture with a precursor with high FA content didn't crack, Chapter 8 validates if a mixture with a 100% BFS precursor and an activator with lower Al etching solution won't show cracks.

6.3 Conclusions

The experimental study of fresh and hardened properties revealed key insights into the impact of the etching solution and its relation to the reaction process. This section presents the key findings discussed in this chapter.

- The aluminium modulus, M_a, was found to impact both initial and final setting times, with initial setting times increasing as M_a increased. The Na_2O content had a stronger influence on both initial and final setting times as mixture N6A1.73 exhibited shorter setting times compared to N4A0.66, despite a higher M_a. This increase in setting time with added Al in the activator aligns with findings in the literature (Chen et al., 2021).
- The deviating final setting time of N4A0.66 can be explained by the normalized heat release profile of the mixture. the aluminium modulus by modifying either the Na_2O or Al_2O_3 content allows for control over setting times. However, as setting times are closely tied to specific reaction stages, designing a mixture based solely on desired setting times can be challenging, as illustrated by the final setting time of N4A0.66.
- The addition of the etching solution can lead to improved strength after 1 day compared to the reference mixtures. However, excessive amounts of etching solution can significantly slow strength development, resulting in minimal strength gains after 1 day. Nonetheless, higher etching solution content did demonstrate enhanced strength development after 7 days, indicating that the Al_2O_3 content in the activator contributes positively to long-term strength.
- In terms of tensile performance, mixtures containing the etching solution exhibited lower flexural strength compared to compressive strength when compared to the reference mixtures. This disparity may be attributed to tensile stresses that develop in the samples due to their too high reaction.
- Additionally, the samples with the etching solution showed spontaneous crack formation between 1 and 7 days. This crack formation is suspected to result from elevated autogenous shrinkage, which is likely caused by the increased reactions of these mixtures.

7 Experimental study on the reaction products

This section considers different experimental techniques to characterize the reaction products formed. With the results, the model can be validated and the influence of the activator composition on the microstructure can be evaluated. The techniques that were employed are TGA, XRD, FTIR, and SEM-EDS.

7.1 Materials and methods

7.1.1 Materials and mixtures

The slag and activator components used in this chapter are the same as used in Chapter 5. The mixtures designed in Section 4.3 were also used in this chapter to investigate the reaction products formed for each mixture.

After the strength experiments which are shown in Chapter 6, residue of the broken specimen was collected, and stored in isopropanol. As the same samples are used for the strength tests and characterization, a good relation between the properties can be made. After sample collection, the samples were ground down to a powder while being submerged in the isopropanol and the hydration was stopped according to the procedure defined by RILEM (Snellings et al., 2018). The powder samples were then stored in a vacuum oven with a constant temperature of 25°C to avoid carbonation.

Initially, all mixtures were analyzed. However, if the TGA results indicate similar trends for the mixtures containing 6 wt.% Na_2O compared to those with 4 wt.% Na_2O, further testing focused only on the 4 wt.% mixtures to optimize time and resources. Additionally, as the final mixture design prioritizes a Na_2O content of 4 wt.%, this concentration is key to maximizing the potential application volume of the aluminium etching solution. For this reason, a greater emphasis is placed on the mixtures containing 4 wt.% Na_2O in subsequent investigations. Furthermore, if the experimental results align with the modelling predictions, the outcomes for the 6 wt.% Na_2O mixtures may be simplified, assuming the modelling results hold true.

7.1.2 TGA

Thermogravimetric Analysis (TGA) is conducted to assess the thermal stability and decomposition behavior of the alkali-activated binder samples. TGA measures the weight changes of a material as it is heated, allowing for the identification of various decomposition stages, such as water loss, carbonation, and the breakdown of reaction products. This technique is particularly useful for understanding the hydration and reaction mechanisms in alkali-activated binders

TGA is performed using a STA 449 F4 Jupiter. Alumina crucibles were used to hold the sample during the TGA with a sample mass of approximately 50 mg of paste sample. The analysis was conducted over a temperature range of 40°C to 1000°C, with a heating rate of 10 K/min. The experiment was carried out under an argon atmosphere to prevent oxidation, with a purge gas flow rate of 50 mL/min and a protective gas flow rate of 20 mL/min. These parameters were chosen to ensure a controlled and stable environment during the analysis, allowing for accurate measurement of mass loss and thermal stability of the samples.

7.1.3 XRD

X-ray Diffraction (XRD) analysis was performed to investigate the crystalline phases present in the alkali-activated binder samples. For the reasons explained before, only the mixtures N4REF, N4A0.66 and N4A2.02 were investigated further from this point onward.

The analysis was conducted using a Bruker D8 ADVANCE diffractometer. The powder samples were scanned over a 2θ range of 5-70°, with a step size of 0.02°and a time interval of 1 second per step. A qualitative analysis was performed to identify the crystalline phases present in the samples, serving to validate both the TGA and the results from the reaction modelling.

7.1.4 FTIR

Fourier Transform Infrared Spectroscopy (FTIR) is utilized to investigate the chemical bonding and molecular structure of the alkali-activated binders activated by the new activators. By analyzing the absorption of infrared radiation at different wavelengths, it becomes possible to track the evolution of key chemical species during the activation process, particularly silicate and aluminate phases, as well as the presence of bound water or other hydration products.

The FTIR spectra provides insights into the development of the C-(N-)A-S-H gels and other reaction products, highlighting the influence of aluminium content in the activators. Each sample was subjected to FTIR analysis at different curing times, allowing for a comparison of the structural changes over time. This method serves as a complementary tool to TGA and XRD, further elucidating the chemical and structural properties of the alkali-activated binders.

The powdered samples of N4REF, N4A0.66 and N4A2.02 are analyzed using FTIR over a wavelength range of 600 to 2000 cm^{-1}. By examining the location of the peaks and comparing them with those reported in the literature, specific phases can be identified. These identified phases provide additional validation for the results obtained from TGA and XRD analyses.

7.1.5 SEM-EDS

Scanning Electron Microscopy coupled with Energy Dispersive X-ray Spectroscopy (SEM-EDS) is utilized to analyze the chemical composition of the reaction products formed in the different mixtures. EDS provides elemental analysis at specific points or areas, helping to identify the distribution and composition of key elements such as Si, Al, and Ca. This data offered insights into the chemical characteristics of C-(N-)A-S-H phases and other reaction products. The results complement the findings from TGA, XRD, and FTIR, enhancing the understanding of the influence of activator composition on the reaction mechanisms.

For the SEM-EDS analysis, only the 28-day samples of N4REF, N4A0.66 and N4A2.02 were considered. Sample preparation is done similarly to the method described in Chapter 8.4.1 of the book A Practical Guide to Microstructural Analysis of Cementitious Materials. (Scrivener, Snellings, & Lothenbach, 2015) Each sample was first impregnated with epoxy to ensure structural stability and to fill any pores. Following impregnation, the samples were carefully ground and polished to reveal a smooth surface suitable for analysis.

The polished samples were then examined under the scanning electron microscope (SEM) at a magnification of 1000. A total of 60 distinct spots were selected for energy-dispersive X-ray spectroscopy (EDS) to perform a chemical analysis of the reaction products. The chosen spots were distributed across the surface to ensure a representative analysis of the elemental composition within the sample.

7.2 Results and discussion

7.2.1 TGA

This section presents the results of the thermogravimetric analysis (TGA) are presented. Six figures are included, each displaying the thermogravimetric (TG) and derivative thermogravimetric (DTG) curves of the mixtures with corresponding weight percentages of Na_2O at the specified curing ages. This arrangement allows for a detailed investigation of the influence of activator composition on the thermal behavior and thus reaction product formation of the mixtures. In Appendix F, the evolution of TG and DTG over time for each mixture can be seen.

The TGA results for mixtures containing 4 wt.% Na_2O at 1, 7, and 28 days can be seen in Figures 56, 57 and 58. Each figure has a corresponding table with the total weight losses, weight losses from 40-100 °C and the weight losses in the range of 200-400 °C for each mixture.

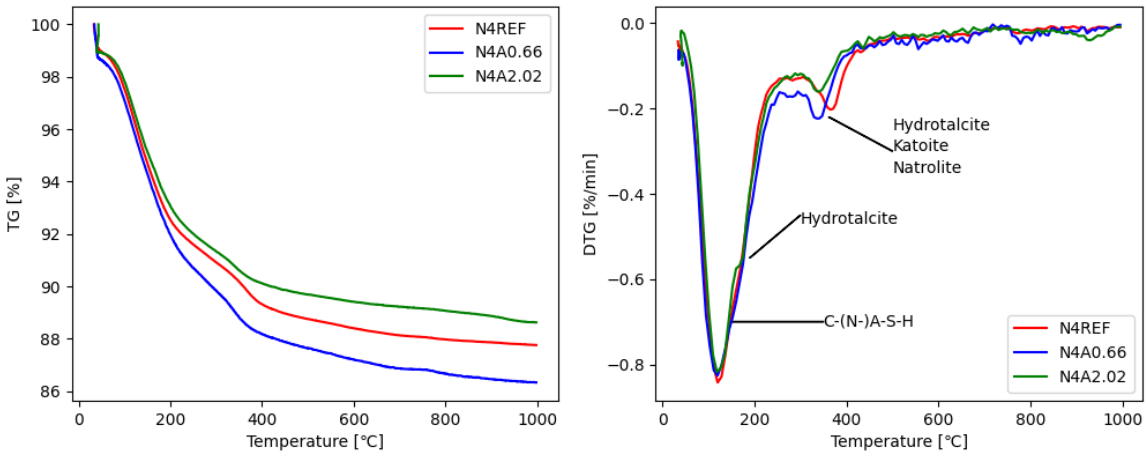

Figure 56: TGA of the mixtures containing 4 weight percent of Na_2O after 1 day of curing.

Table 22: Weight loss of the mixtures at 1 day, expressed in percent.

Mixture	Total weight loss	Weight loss 40-200°C	Weight loss 200-400°C
N4REF	12.21	7.46	3.22
N4A0.66	13.66	8.02	3.80
N4A2.02	11.37	6.93	2.95

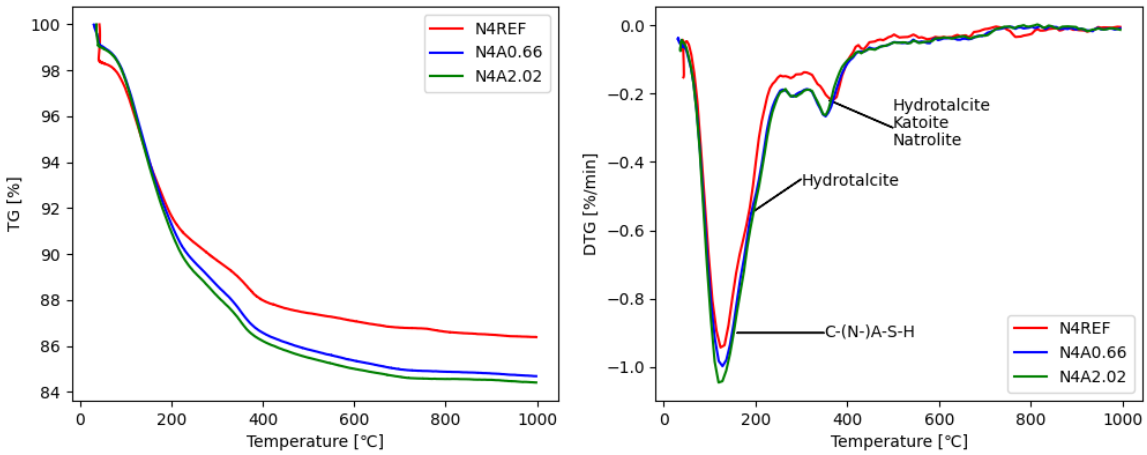

Figure 57: TGA of the mixtures containing 4 weight percent of Na_2O after 7 days of curing.

Table 23: Weight loss of the mixtures at 7 days, expressed in percent.

Mixture	Total weight loss	Weight loss 40-200°C	Weight loss 200-400°C
N4REF	13.62	8.32	3.69
N4A0.66	15.32	8.67	4.75
N4A2.02	15.60	9.02	4.77

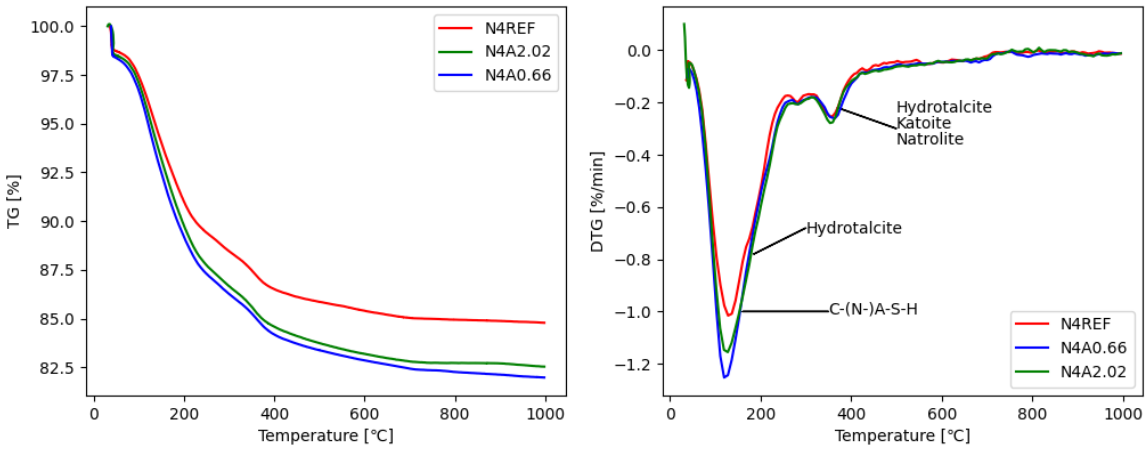

Figure 58: TGA of the mixtures containing 4 weight percent of Na_2O after 28 days of curing.

Table 24: Weight loss of the mixtures at 28 days, expressed in percent.

Mixture	Total weight loss	Weight loss 40-200°C	Weight loss 200-400°C
N4REF	15.22	9.02	4.48
N4A0.66	18.03	10.84	4.98
N4A2.02	17.47	10.25	5.18

The TGA results for mixtures containing 4 wt.% Na_2O at 1, 7, and 28 days can be seen in Figures 59, 60 and 61. Each figure has a corresponding table with the total weight losses, weight losses from 40-100 °C and the weight losses in the range of 200-400 °C for each mixture.

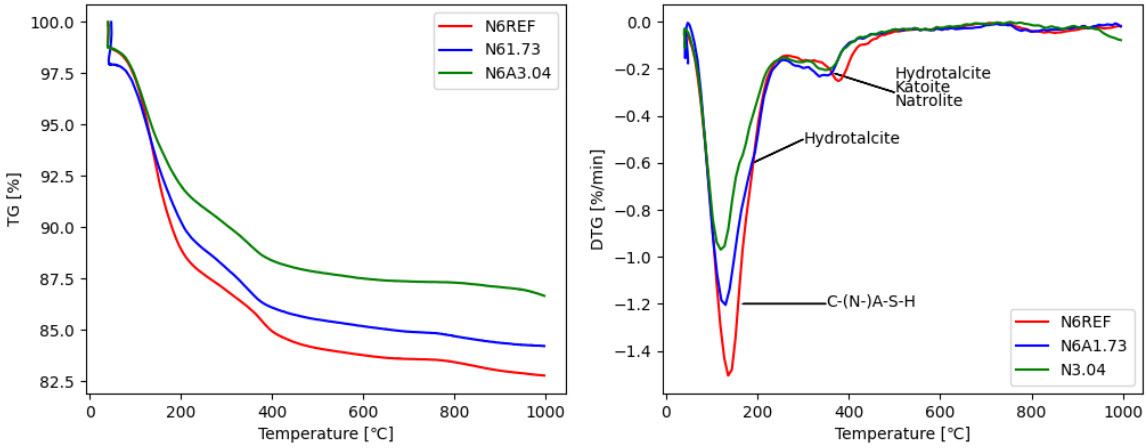

Figure 59: TGA of the mixtures containing 6 weight percent of Na_2O after 1 day of curing.

Table 25: Weight loss of the mixtures at 1 day, expressed in percent.

Mixture	Total weight loss	Weight loss 40-200°C	Weight loss 200-400°C
N6REF	17.23	11.04	4.02
N6A1.73	15.80	9.72	4.19
N4A3.04	13.35	7.96	3.66

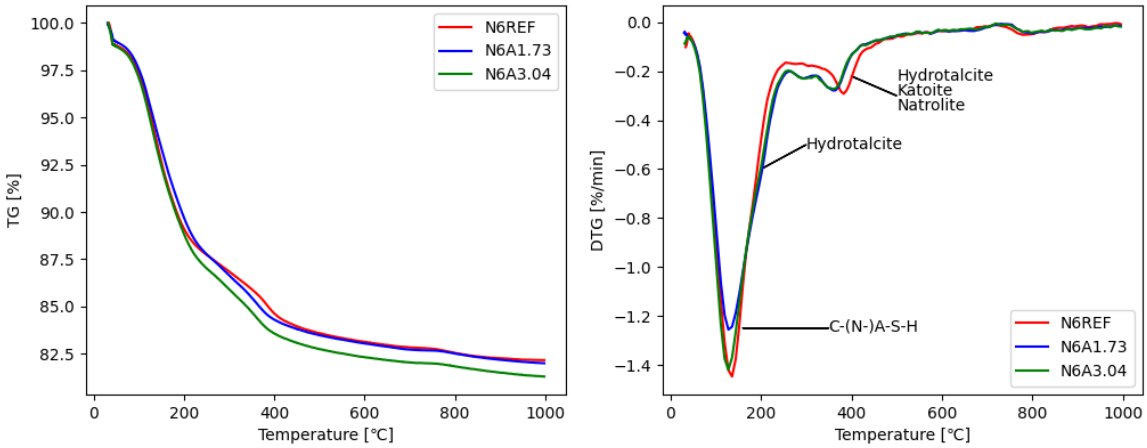

Figure 60: TGA of the mixtures containing 6 weight percent of Na_2O after 7 days of curing.

Table 26: Weight loss of the mixtures at 7 days, expressed in percent.

Mixture	Total weight loss	Weight loss 40-200°C	Weight loss 200-400°C
N6REF	17.84	10.92	4.47
N6A1.73	18.01	10.33	5.37
N4A3.04	18.71	11.20	5.23

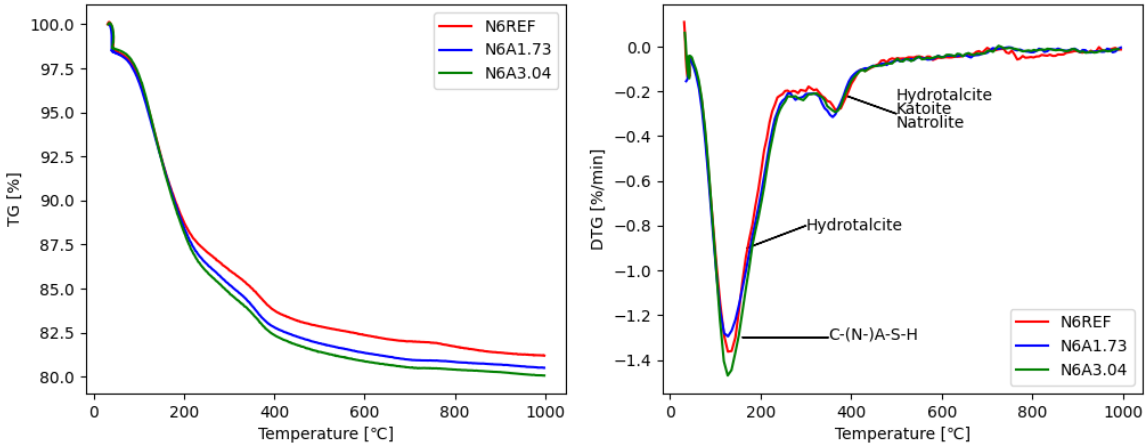

Figure 61: TGA of the mixtures containing 6 weight percent of Na_2O after 28 days of curing.

Table 27: Weight loss of the mixtures at 28 days, expressed in percent.

Mixture	Total weight loss	Weight loss 40-200°C	Weight loss 200-400°C
N6REF	18.80	11.26	4.97
N6A1.73	19.49	11.53	5.66
N4A3.04	19.93	11.81	5.83

The results presented above, show a similar general trend for all curves. A prominent weight loss peak occurs just before 200°C, which corresponds to the decomposition of the C-(N-)A-S-H phases. The position of this peak varies slightly, influenced by the Ca/Si ratio in the C-(N-)A-S-H gels. Gels with a higher Ca/Si ratio exhibit peaks shifted toward lower temperatures, while those with a lower Ca/Si ratio display peaks at higher temperatures (Scrivener et al., 2015). Following this first peak, a slight slope change is observed, attributable to the evaporation of interlayer water in hydrotalcite around 270°C (Scrivener et al., 2015).

Between 300-400°C, multiple phases are expected to decompose, including katoite (≈320°C), hydrotalcite (≈400°C), and natrolite (≈385°C) (Scrivener et al., 2015; Kónya & Földvári, 2008). Due to the overlapping decomposition temperatures of these phases, identifying the presence of each specific phase becomes challenging. Notably, the second peak for the reference mixture shifts further to the right, suggesting that hydrotalcite is more dominant in this sample as it decomposes at the highest temperature. This observation aligns with the model predictions, which indicate that N4REF contains the largest quantity of hydrotalcite at 1, 7, and 28 days compared to N4A0.66 and N4A2.02.

In addition to peak position, the magnitude of weight loss also provides insights into phase quantities. According to Table 22, N4A0.66 exhibits the greatest weight loss between 40-200°C, indicating the highest concentration of C-(N-)A-S-H gels after 1 day. Similarly, N4A0.66 shows the most significant weight loss between 200-400°C, pointing to a greater presence of hydrotalcite, katoite, and natrolite. Although N4A0.66 contains more of these combined phases, it is likely that N4REF has a higher proportion of hydrotalcite, as suggested by the rightward shift of the second peak and modelling results.

After 7 days, N4A2.02 displays the largest weight loss in both the 40-200°C and 200-400°C ranges, although N4A0.66 shows comparable values. The peak locations for both N4A0.66 and N4A2.02 are similar, suggesting that they form comparable reaction products. Once again, the second peak for N4REF is shifted slightly to the right, indicating a higher hydrotalcite content. By 28 days, the second peak appears at similar positions and magnitudes for all mixtures. However, Appendix F shows a shift of the second peak to the left over time for N4REF, while for N4A0.66 and N4A2.02, the peak shifts to the right, suggesting increased hydrotalcite formation in N4A0.66 and N4A2.02 and increased katoite formation in N4REF after 7 days.

The first peak's magnitude increases for all mixtures over time, as does the weight loss in the 40-200°C range, indicating an overall increase in C-(N-)A-S-H gels. Notably, the increase in C-(N-)A-S-H content for N4A2.02 after 1 day is significantly higher than for N4REF and N4A0.66, while having the lowest C-(N-)A-S-H content after 1 day.

For mixtures containing 6 wt.% Na_2O, similar trends are observed. After 1 day, N6A3.04 shows the lowest weight loss, while N6REF exhibits the highest weight loss which deviates from the results of the mixtures containing 4 wt.% of Na_2O. By 7 days, N6A3.04 demonstrates the largest total weight loss and the highest weight loss attributed to C-(N-)A-S-H gels. The second peak for N6REF is also shifted to the right compared to N6A1.73 and N6A3.04, although the peaks converge again by 28 days.

As with the 4 wt.% Na_2O mixtures, N6A1.73 and N6A3.04 show a rightward shift in the second peak, suggesting that natrolite is incorporated into other phases such as C-(N-)A-S-H over time, while hydrotalcite continues to form. Interestingly, the total weight loss for N6REF remains relatively unchanged after the first day indicating most of the reaction takes place in the first day. Consistent with previous observations, the undiluted N6A3.04 mixture exhibits the largest increase in weight loss over time, in line with the trends seen in mixtures containing 4 wt.% Na_2O.

7.2.2 XRD

For mixture N4REF, the same phases are consistently present throughout the reaction. The identified phases include C-S-H-like phases, hydrotalcite, katoite, and strätlingite. As shown in Appendix G, all the peaks correspond to these phases, with the only deviation from the modelling results being the presence of strätlingite.

In the case of mixture N4A0.66, the same phases as those in N4REF are present during the entire reaction. However, after 1 day, the presence of strätlingite is not as pronounced as in N4REF. The detected phases include C-S-H-like phases, hydrotalcite, katoite, and strätlingite. Again, all peaks are accounted for by these phases, as shown in Appendix G, with the only deviation from the modelling results being the presence of strätlingite.

For mixture N4A2.02, the XRD pattern shows a notable deviation from N4REF and N4A0.66, particularly in the 1-day sample, where very few intense peaks are observed. After 1 day, natrolite, hydrotalcite, katoite, and some C-S-H-like phases are detected. By 7 days, the peaks become more distinct. For both the 7-day and 28-day samples, natrolite is no longer detected, with the remaining phases being C-S-H-like phases, hydrotalcite, katoite, and strätlingite, all of which are covered as shown in Appendix G.

The phases identified in the XRD and GEMS for N4REF are presented in Table 28 The phases identified in

Table 28: Identified phases in XRD and GEMS for N4REF

	XRD	**GEMS**
1 Day	CSH like phases Hydrotalcite Katoite Strätlingite	Portlandite C-(N-)A-S-H Hydrotalcite Katoite
7 Days	CSH like phases Hydrotalcite Katoite Strätlingite	C-(N-)A-S-H Hydrotalcite Katoite
28 Days	CSH like phases Hydrotalcite Katoite Strätlingite	C-(N-)A-S-H Hydrotalcite Katoite

the XRD analysis align closely with the modelling results. For N4REF, all model-predicted phases are present, with the addition of strätlingite throughout the entire 28 days.

The phases identified in the XRD and GEMS for N4A0.66 are presented in Table 29.

Table 29: Identified phases in XRD and GEMS for N4A0.66

	XRD	**GEMS**
1 Day	CSH like phases Hydrotalcite Katoite	C-(N-)A-S-H Hydrotalcite Katoite
7 Days	CSH like phases Hydrotalcite Katoite Strätlingite	C-(N-)A-S-H Hydrotalcite Katoite
28 Days	CSH like phases Hydrotalcite Katoite Strätlingite	C-(N-)A-S-H Hydrotalcite Katoite

The modelling predicted that natrolite would no longer be present after 1 day, which aligns with the XRD results. The identified phases match the model, with the exception of strätlingite, which is observed at both 7 and 28 days.

The phases identified in the XRD and GEMS for N4A2.02 are presented in Table 30

Table 30: Identified phases in XRD and GEMS for N4A2.02

	XRD	**GEMS**
1 Day	Natrolite CSH like phases Katoite Hydrotalcite	Natrolite C-(N-)A-S-H Katoite Hydrotalcite
7 Days	CSH like phases Katoite Hydrotalcite Strätlingite	C-(N-)A-S-H Katoite Hydrotalcite Strätlingite
28 Days	CSH like phases Katoite Hydrotalctie Strätlingite	C-(N-)A-S-H Katoite Hydrotalcite Strätlingite

The XRD results after 1 day show less distinct peaks, indicating the presence of fewer crystalline phases and reflecting the lower reaction observed in previous experiments. The detection of natrolite after 1 day is consistent with the model. By 7 days, the reaction has accelerated, which is reflected in the clearer XRD peaks. After 7 days, the same phases are identified as in the other mixtures. Unlike N4REF and N4A0.66, strätlingite is predicted in N4A2.02 at both 7 and 28 days.

Overall, the XRD results validate the model and align with previous observations, particularly regarding the reaction acceleration in N4A2.02. Since N4A0.66 experiences this acceleration within the first day, its XRD pattern does not show significant deviations at this time point. The lower strength observed in N4A2.02 at 1 day is consistent with the lower amount of crystalline phases formed, further confirming the calorimetry results.

7.2.3 FTIR

The FTIR results of mixtures N4REF, N4A0.66 and N4A2.02 after 1, 7 and 28 days of curing can be seen in Figures 62 and 63. Each plot, identifies different peaks related to reaction product characteristics.

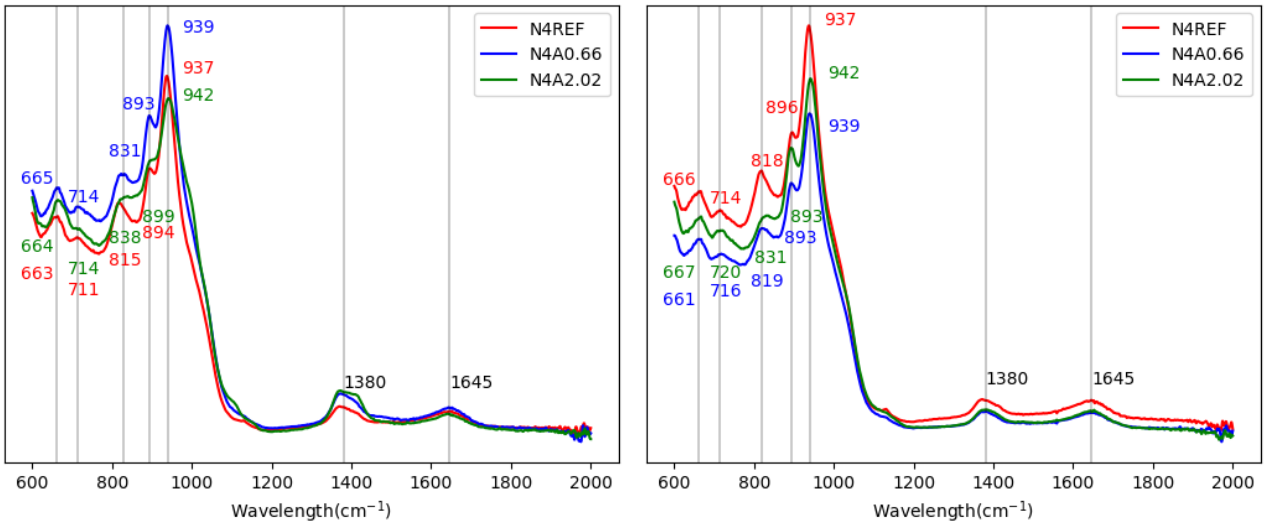

Figure 62: FTIR results of the samples after 1 day (left) and 7 days (right) of curing

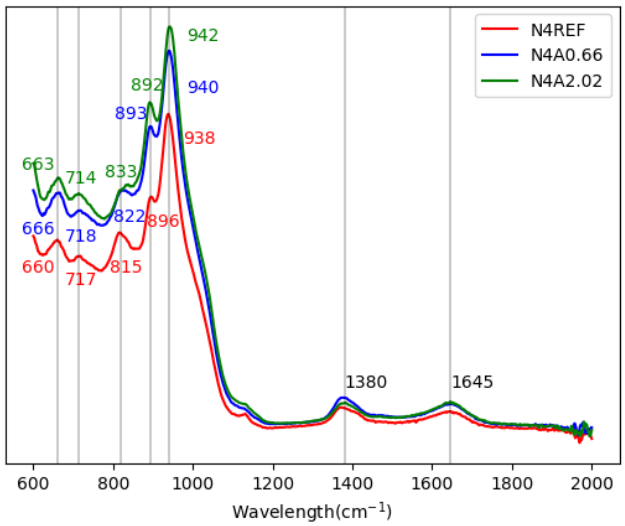

Figure 63: FTIR results of the samples after 28 days of curing

The peak around 660 cm^{-1} is attributed to the symmetrical stretching of $Si-O-T$ bonds due to the presence of C-(N-)A-S-H gel, where T can either be Al or Si (Liu, Chen, et al., 2024). The peak around 710 to 720 cm^{-1} is attributed to $Si-O-Si, Al$ bonds which are related to C-(A-)S-H phases (Wang et al., 2022). The peak around 820 to 820 cm^{-1} is related to the Q_1 tetrahedron in C-(A-)S-H gel and the peak around 890 cm^{-1} is related $Al-O$ bonds which again can be related to C-(A-)S-H gels (Wang et al., 2022). The main band around 940 cm^{-1} is related to the $Si-O$ bonds or $Si-O-M$ bonds, where M is an alkali or earth alkali metal (Zhang et al., 2021), which can again be linked to the presence of C-(N-)A-S-H type gels. Another paper suggests that this peak should be assigned to the asymmetrical stretching vibration of $Si-O-Al$ bonds, which would also be related to the presence of C-(N-)A-S-H gels (Liu, Chen, et al., 2024). Finally some peaks can be observed around 1400 cm^{-1} and 1645 cm^{-1}. These peaks are related to presence of carbonates and the symmetric stretching of $O-H$ bonds respectively (Zhang et al., 2021). The peak around 1400 cm^{-1} related to the carbonates, indicates the presence of hydrotalcite (Liu et al., 2022).

In the results presented, it is evident that all mixtures form C-(N-)A-S-H-like phases, as indicated by the identified peaks. In addition to C-(N-)A-S-H-like gels, hydrotalcite is observed in all mixtures, confirmed by

the presence of a peak around 1400 cm^{-1}. As the identification of these phases was already performed by both TGA and XRD, further investigation of the structure of the C-(N-)A-S-H-like phases is performed.

It can be observed that mixture N4REF consistently shows the lowest wavenumber for the main band around 940 cm^{-1} throughout the reaction, while N4A0.66 exhibits a slightly higher wavenumber, and N4A2.02 shows the highest wavenumber for this peak over the entire duration. The variations in wavenumber between the mixtures can be explained by different physical factors. One reported explanation is that a lower wavenumber corresponds to a greater substitution of Si by Al in Si-O-Si bonds (Zhang et al., 2021). This would suggest that, contrary to expectation, the reference mixture (N4REF) contains more Al incorporated into its C-(N-)A-S-H-like phases than the aluminium-containing mixtures.

Another factor that may influence the shift in the main band is the degree of polymerization. Higher degrees of polymerization are associated with shifts to higher wavenumbers (Zhang et al., 2021)(Liu, Chen, et al., 2024). Since the wavenumbers of the mixtures either increase over time or remain constant, it seems likely that the shift in wavenumber is indeed related to the degree of polymerization.

Additionally, the mixtures N4A0.66 and N4A2.02 exhibit a significant shift between 1 and 7 days from wavenumber 831 to 819 cm^{-1} and from 838 to 831 cm^{-1} respectively. This wavenumber is associated to the Q_1 tetrahedron, which is related the the silica chain end. A shift in this indicates changes of this site, which could be a result of a change in MCL of the C-(N-)A-S-H gel like phases (Wang et al., 2022). Besides the shift around 830 cm^{-1}, another shift occurs for N4A2.02, this being a shift between 1 and 7 days from 899 to 893 cm^{-1}. As this wavenumber is associated to the Al-O bonds in the C-(N-)A-S-H gel like phases and a shift towards lower wavenumber indicates higher Al incorporation(Kapeluszna, Łukasz Kotwica, Rózycka, & Łukasz Gołek, 2017), it indicates an increase in Al incorporation in the C-(N-)A-S-H gel like phases between 1 and 7 days for N4A2.02. It is expected that a similar shift will be observed when performing FTIR for N4A0.66 within the first day, but as the acceleration of N4A0.66 occurs within the first day, most of the Al will already be incorporated in the C-(N-)A-S-H gel like phases as also the pore solution concentrations after 1 day indicate.

7.2.4 SEM-EDS

The average atomic ratios between certain elements within the reaction products can be seen in Table 31. The ratios are based on the average values determined by averaging a total of 60 data points for each mixture.

Table 31: Atomic ratios within the reaction products of the mixtures at 28 days.

Mixture	Ca/Si	Al/Si	Ca/(Al+Si)
N4REF	1.28 ± 0.19	0.39 ± 0.06	0.92 ± 0.14
N4A0.66	1.2 ± 0.12	0.41 ± 0.08	0.85 ± 0.08
N4A2.02	1.27 ± 0.13	0.46 ± 0.05	0.87 ± 0.09

The ternary diagram with the normalized composition of the reaction product expressed in CaO, Al_2O_3 and SiO_2 can be seen in Figure 64.

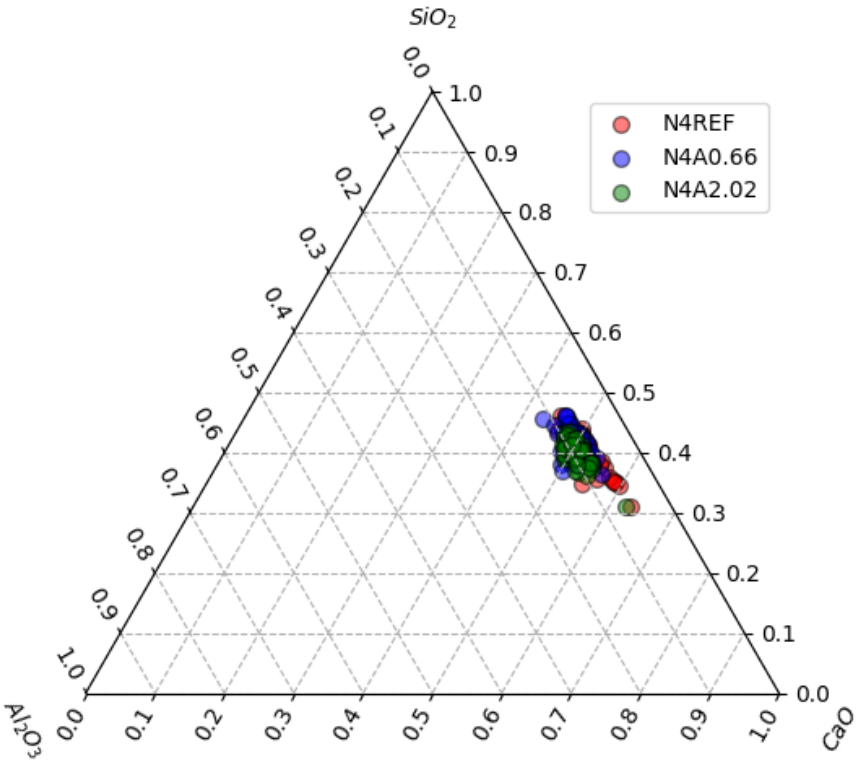

Figure 64: Ternary diagram of the composition of the reaction product, expressed in CaO, Al_2O_3 and SiO_2

When investigating the Al/Si ratio related to the aluminium modulus it can be found that a very good linear relationship can be found between an increase in M_a and an increase in Al/Si ratio as can be seen in Figure 65.

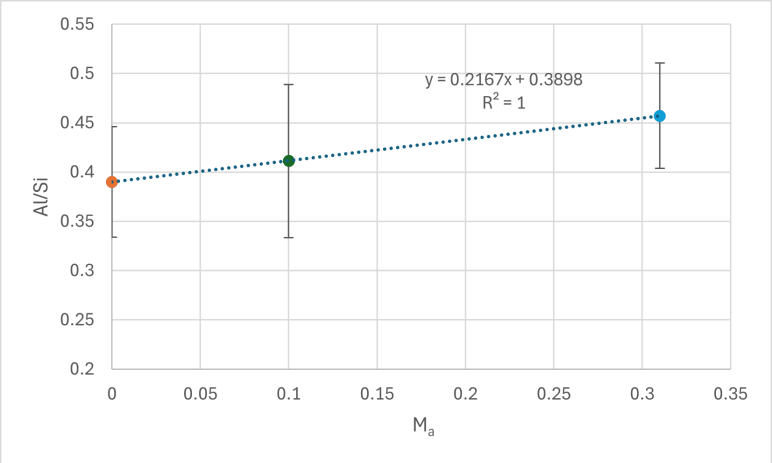

Figure 65: Relation between the aluminium modulus and Al/Si ratio in the reaction products.

The normalized composition of the reaction products expressed in CaO, Al_2O_3 and MgO can be seen in Figure 66. A shift towards higher Al_2O_3 contents for the mixtures containing the aluminium rich activator is observed. Another observation is that the reference mixture has the highest normalized composition of MgO, followed by N4A0.66 and N4A2.02, indicating a higher content of hydrotalcite for mixture N4REF.

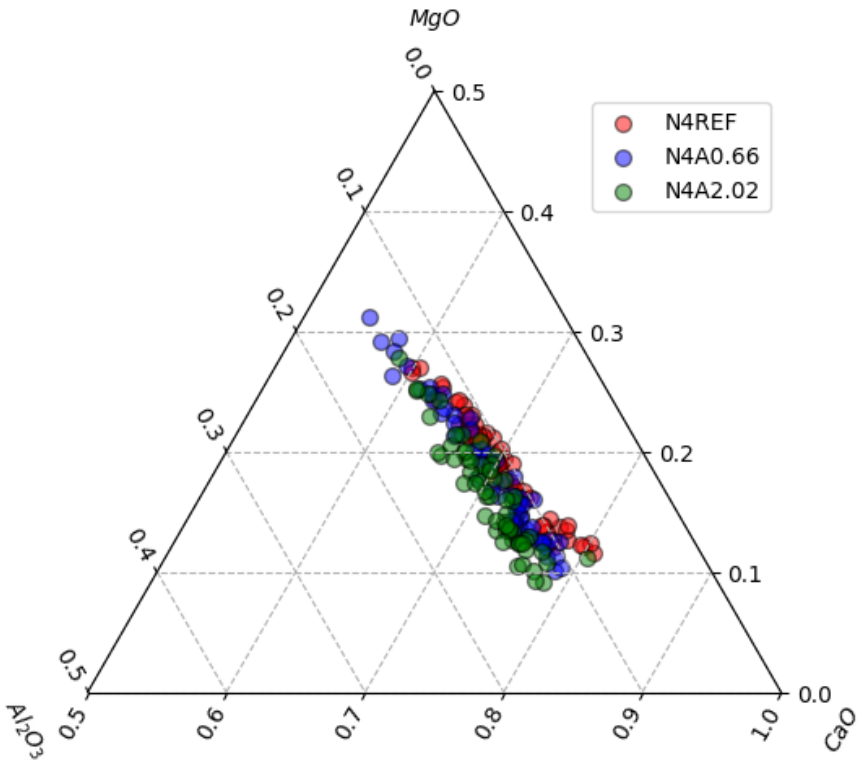

Figure 66: Ternary diagram of the composition of the reaction products, expressed in CaO, Al_2O_3 and MgO

Upon analyzing the images of the SEM, cracks appeared which were not visible for the naked eye. In Figure 67, the SEM images can be seen for mixture N4A0.66. When zooming in with different magnifications in becomes clear that the cracks in the aluminium rich mixtures are present on every scale investigated.

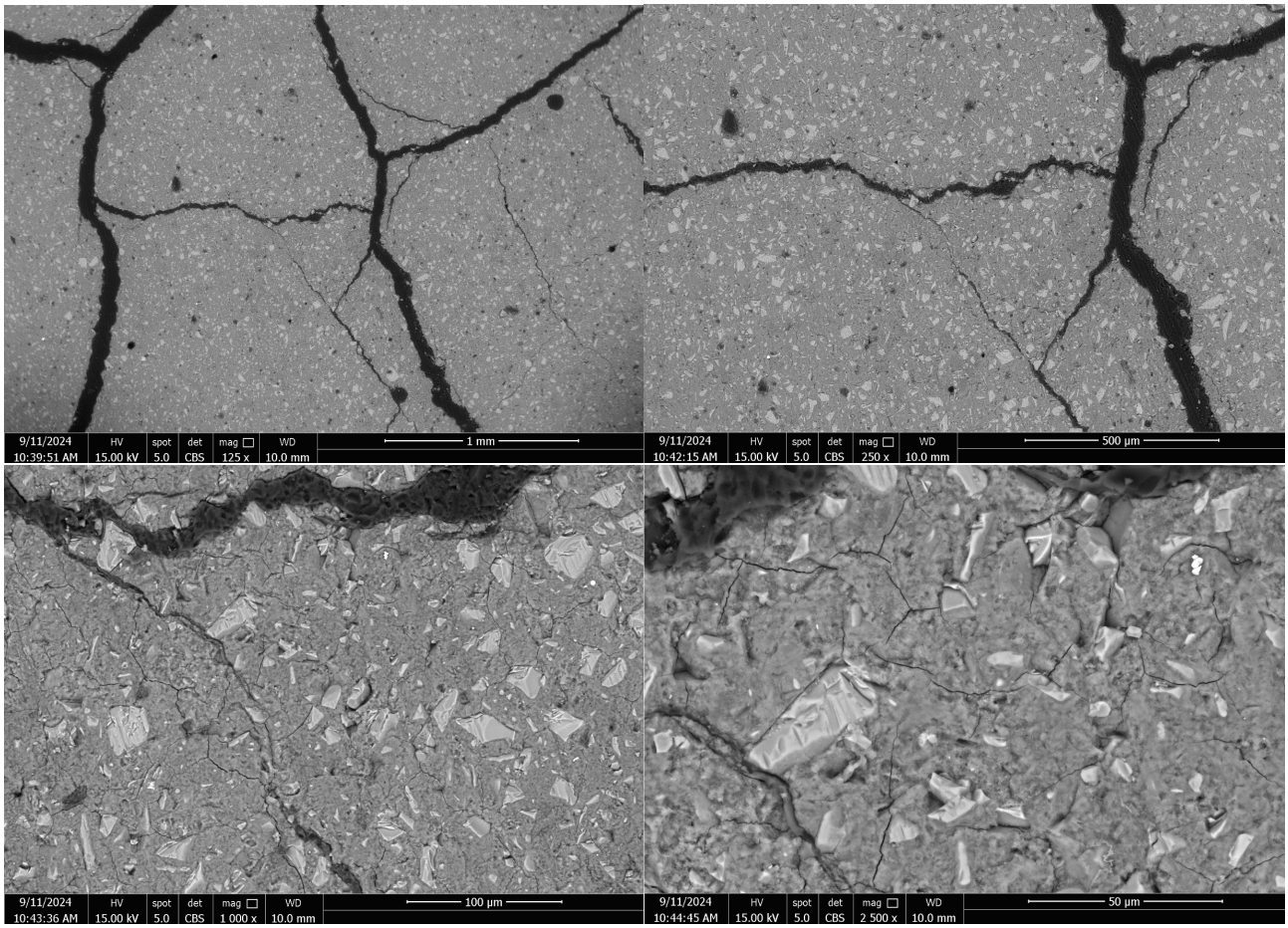

Figure 67: SEM images of N4A0.66 at different magnifications

In Appendix H, the SEM images at 250 and 1000 magnification can be seen for both N4REF and N4A2.02. For N4A2.02, again cracks can be detected, but less obvious compared to N4A.066.

The literature suggests that both mean chain length (MCL) and basal spacing in C-(N-)A-S-H gels increase with an decrease in the Ca/(Al+Si) ratio. A longer MCL is known to enhance the micro-mechanical properties of C-(N-)A-S-H gels, leading to improved mechanical performance (Wang et al., 2022). Based on the results presented in Table 31, it can be concluded that mixtures with a lower Ca/(Al+Si) ratio, such as N4A0.66 (0.85) and N4A2.02 (0.87), are expected to demonstrate superior mechanical properties compared to the reference mixture, N4REF (0.92). This aligns with the compressive strength results, where the aluminium-containing mixtures (N4A0.66 and N4A2.02) exhibit enhanced strength after 7 days, likely due to their longer silicate chains and more polymerized structures.

Furthermore, it is reported that an increase in the Ca/Si ratio corresponds with a lower position of the main T-O band in FTIR spectra (Zhang et al., 2021). This trend roughly matches the experimental results observed in the mixtures, where a higher Ca/Si ratio, as seen in N4REF (1.28), corresponds with a lower wavenumber in the FTIR spectra. This relationship between the Ca/Si ratio and the main T-O band indicates a less polymerized silicate network in the reference mixture compared to the aluminium-containing mixtures, which exhibit higher wavenumbers and therefore more polymerized structures.

In addition, the Mg content from the SEM-EDS analysis validates that N4REF contains the highest amount of hydrotalcite compared to the aluminium-containing mixtures, which the TGA data and modelling suggested.

7.2.5 Discussion

Reaction products - Reaction process
The XRD and TGA results indicated that the Al containing mixtures form natrolite in the early stage of the reaction. Later the natrolite would be incorporated in C-(N-)A-S-H gels as the shift in the TGA curves indicate as both the first peak becomes deeper over time, indicating more C-(N-)A-S-H gel like phases and the second peak shifts to the higher decomposition temperatures which would indicate less natrolite compared to hydrotalcite and katoite. In the XRD curves, there are no traces of natrolite for the mixtures at ages of 7 days or older, while for N4A2.02 natrolite was detected at 1 day, which corresponds with the modelling presented in Section 5.2.2.

The higher concentration of Al in the pore solution in the early phases retarded the polymerization of C-(N-)A-S-H like phases as it inhibits the dissolution of Si and therefore prohibit the formation of reaction products. The slow development of C-(N-)A-S-H gel is shown by the lower weight loss at 1 day of the mixtures containing the Al etching solution, presented in the TGA results. Eventually the Al concentration in the pore solution achieves similar values for the 28 days samples, which would indicate that the reaction products for the mixtures containing high initial Al concentrations would have more Al incorporated in them compared to the NaOH activated mixtures. The SEM-EDS analysis confirms a higher Al/Si ratio for both N4A0.66 and N4A2.02 compared to the reference mixture which validates the higher Al incorporation in the reaction products.

The TGA results showed that mixture N4A2.02 experienced the lowest weight loss related to C-(N-)A-S-H gel. Notably, this mixture experienced the greatest weight loss related to C-(N-)A-S-H gel after 7 days, supporting the accelerated reaction observed in Sections 5.2.2 and 5.2.3.

Reaction products - Strength
A critical observation from the compressive strength tests is that while mixtures containing the Al etching solution exhibited slower early strength development, they achieved higher strengths after 7 days.

The enhanced long term strength can be linked to the evolving chemistry in the pore solution and the gradual formation of C-(N-)A-S-H phases. The combination of calorimetry, pore solution, TGA, XRD, and FTIR analysis demonstrated that Al not only slows the reaction in the early stages but also contributes to the formation of more cross-linked gel structures with a higher mean chain length (MCL). The increase of the MCL is indicated by the shift of the peak related to the Q^1 tetrahedron and by the higher bandwidth of the main peak of the Al etching solution containing mixtures in FTIR. The identification of the phases in TGA and XRD further support the findings.

In the TGA analysis, the weight loss associated with the formation of C-(N-)A-S-H gel-like phases, was shown to increase significantly more after 1 day in the aluminium-rich mixtures compared to the reference mixtures. In contrast, the reference mixtures exhibited the greatest weight loss after 1 day, indicating that C-(N-)A-S-H-like phases develop more gradually in the aluminium-rich mixtures.

The SEM-EDS analysis complements these findings by providing direct evidence of the chemical composition and phase distribution within the samples. The EDS data revealed a higher concentration of Al in the C-(N-)A-S-H gels in mixtures N4A0.66 and N4A2.02 compared to N4REF. This increased Al incorporation is also shown by the pore solution chemistry which showed similar final concentrations Al for all mixtures, indicating a higher Al incorporation for N4A0.66 and N4A2.02. This is also consistent with the higher Al/Si ratios observed in the reaction products, which contribute to the enhanced cross-linking and polymerization of the silicate network (J. Li et al., 2019). Additionally, the presence of higher magnesium concentrations in N4REF, confirmed through SEM-EDS, validates the higher formation of hydrotalcite in this mixture, which aligns with the location of the second peak in the TGA results.

This long-term strength gain is especially evident in the mixtures N4A2.02 and N6A3.04, where delayed early reactions eventually led to the formation of more durable phases, characterized by a lower Ca/(Al+Si) ratio. This lower ratio results in a longer MCL due to a higher degree of geopolymerization, the shift of wavenumber at the Q_1 site in FTIR results also indicates a change in MCL for the aluminium rich mixtures. Besides the increase in MCL, the lower Ca/(Al+Si) ratio also leads to an increase in basal spacing. The longer MCL indicates fewer structural defects, and combined with the increase in basal spacing, this leads to improved micro-mechanical properties (Wang et al., 2022). Overall, the combination of these factors—higher Al incorporation, increased polymerization, and the resulting structural modifications—explains the superior mechanical properties observed in the aluminium-rich mixtures after 28 days.

7.3 Conclusions

he experimental study of the reaction products revealed key insights into the impact of the etching solution and its relation to the reaction process and fresh and hardened properties. This section presents the key findings discussed in this chapter.

- XRD and TGA analyses revealed that aluminium-containing mixtures initially formed natrolite, which was progressively incorporated into C-(N-)A-S-H gels as the reaction advanced. This transition is evidenced by deeper first peaks in TGA and a shift in the second peak, indicating a reduction in natrolite and an increase in hydrotalcite and katoite phases.
- In mixture N4A2.02, natrolite remained visible on the first day but disappeared by day 7, aligning well with the modeled reaction kinetics.
- Mixtures containing the aluminium etching solution showed higher aluminium incorporation into reaction products, as confirmed by SEM-EDS data and supported by FTIR results.
- The lower Ca/(Al+Si) ratios observed in SEM-EDS and the higher wavenumber of the main FTIR peak in these mixtures suggest a greater degree of geopolymerization and longer mean chain length (MCL), potentially enhancing the micro-mechanical properties of the C-(N-)A-S-H phases.
- TGA results further support the slower strength development in aluminium-rich mixtures, showing that weight loss associated with C-(N-)A-S-H gel formation accelerated after one day, while the reference mixtures exhibited high weight loss at one day, indicating a more gradual formation of C-(N-)A-S-H phases in the aluminium-containing mixtures.

8 Validation of mixture with lower content of aluminium etching solution

As there is the suspicion that the increase of the aluminium etching solution in the mixtures increases the total reactivity of the mixtures which in turn can lead to an increased autogenous shrinkage and crack formation, a single mixture with a lower content of this solution was cast and tested on the fresh and hardened properties and crack formation. As only the fresh and hardened properties were tested, the same methodology can be used as shown in Section 6.1. The new mixture can be seen in Table 32, which replaces 10% of the fresh Na_2O by Na_2O out of the etching solution.

Table 32: Final mixture design, replacing 10% of the fresh Na_2O with Na_2O originating out of aluminium etching solution.

Mixture	**BFS** [g]	**water** [g]	Na_2O [g]	Al_2O_3 [g]	M_a [-]
N4A0.2	100	40	4	0.2	0.03

8.1 Results

In Figure 68 and 69, both the compressive and flexural strength of mixture N4A0.2 can be seen compared to the other mixtures.

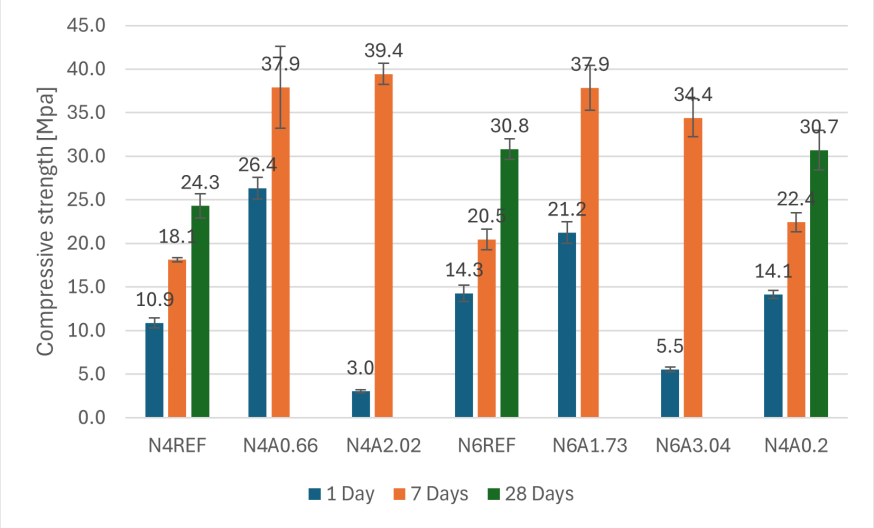

Figure 68: Compressive strength over time for the new mixture compared to the previous mixtures

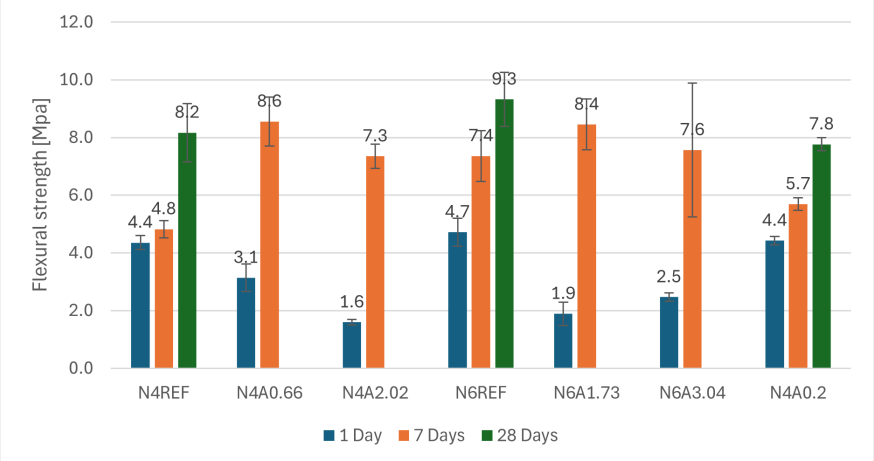

Figure 69: Flexural strength over time for the new mixture compared to the previous mixtures

In Figure 70, the initial and final setting time of Mixture N4A0.2 can be seen compared to the other mixtures.

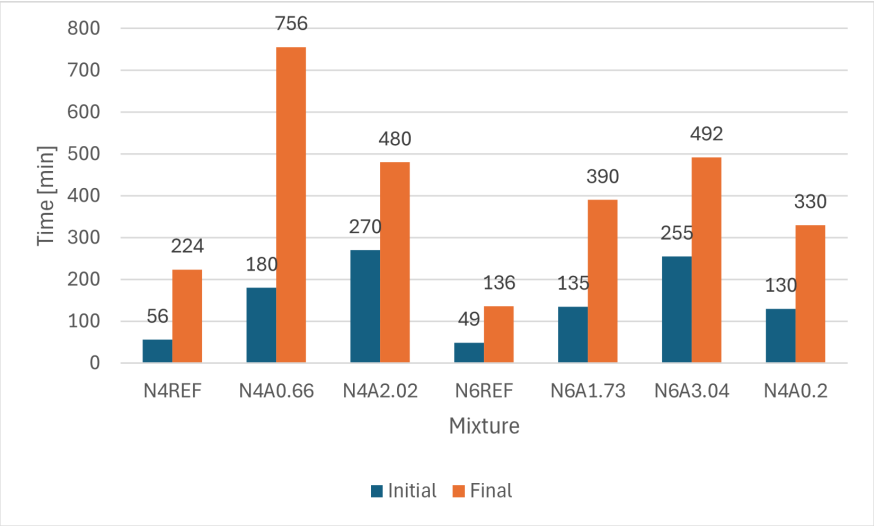

Figure 70: Setting time for the new mixture compared to the previous mixtures

8.2 Discussion

The new mixtures did not show cracks during the entire 28 days of curing, which indicates that by lowering the aluminium etching solution content in the mixture, the total reactivity of the mixture is reduced and less stress induced by autogenous shrinkage is experienced. Besides the observation that no cracks were formed, it can be seen that N4A0.2 shows superior strength development compared to N4REF and very similar strength development to N6REF, showing that the presence of Al has a positive influence on the strength development. The flexural strength however, is very similar to N4REF. When lowering the aluminium content in the activator, the retarding effect on the setting time is also reduced. The initial setting time is roughly doubled compared to N4REF and final setting time is roughly 50% extended. The results in this chapter are in line with the findings shown throughout the research and validating that a decrease in etching solution prevents the cracks formation.

9 Concluding remarks

9.1 Key Findings

- Within the Al etching solution, the $[Al_2O_3]$ is relatively stable across all batches, having a COV of 8.9%. The Al etching solution can become even more stable by either allow precipitation to happen over time or by increasing the Na_2O content in the solution.
- Using GEMS, a prediction of the influence of the activator composition on the reaction products can be made. By different experimental procedures, the model was proved to be accurate. However, the model has limitations which are mostly related to the dissolution behavior of the precursor in the medium. As a result the influence of the activator composition on degree of reaction over time had to be determined by an experimental procedure which leads to a less reproducible modelling procedure as experimental work is incorporated.
- Determining the influence of the aluminium content on the dissolution process was not achieved as the complexity of the aluminium etching solution resulted in extreme variations in ion concentrations which could not originate from slag dissolution. However, in literature it was reported that the aluminium concentrations had an inhibiting effect on the silica dissolution.
- The aluminium content in the activator significantly impacts the reaction process by slowing early reaction mechanisms and passivating slag particles. This effect is evident in the isothermal calorimetry results, where an additional peak appears alongside an overall delay with increasing aluminium content. In addition to delaying the onset of the first peak, higher aluminium content extends the induction period, likely due to the formation of metastable phases that create a gel barrier around the particles, inhibiting further dissolution and reaction. Reducing the aluminium modulus (M_a), and thereby the aluminium content, shortens the induction period. At a critical threshold of M_a, the first and second peaks will likely merge into one, suggesting minimal formation of metastable phases and reduced gel barrier formation at the early stage..
- Overall a higher maximum heat release was predicted for the mixtures containing the aluminium rich activators, indicating that Al etching solution facilitates a higher amount of reaction compared to the reference mixture.
- By combining the isothermal calorimetry data and the GEMS model, it was shown that the meta stable phase Natrolite could be the origin of the first peak observed in the calorimetry data, while the second peak is related to the acceleration of the reaction.
- The pore solution chemistry shows very high concentration of aluminium after 1 day for N4A2.02, N6A1.73 and N6A3.04, as the reaction acceleration has not taken place for these mixtures and the aluminium is not yet incorporated into the reaction products.
- The GEMS model accurately describes the trend of pore solution chemistry, but the magnitudes can vary significantly due to limitations of the model and simplified assumed composition of the etching solution.
- The amount of aluminium in the activator greatly influences the setting time. Overall it can be observed that an increase in aluminium in the activator extends both the initial and final setting time. The longer final setting time of N4A0.66 compared to N4A2.02 can be explained by the calorimetry data, showing that the induction period starts after achieving the initial setting time.
- The aluminium in the activator enhances strength development; however, excessive aluminium can lead to shrinkage-induced stresses, causing cracks. Decreasing the BFS content in the precursor or lowering the aluminium content in the activator, helps to minimize shrinkage and prevent crack formation.
- The aluminium content in the activator has influence on the formed reaction products over time and the composition of those reaction products. Higher aluminium incorporation in the reaction products is and a lower Ca/(Al+Si) ratio is observed which indicates a longer MCL, which could benefit the micro-mechanical properties.

9.2 Recommendations

Even though quite some findings are made, the use of the aluminium etching solution as a possible alkali activator is not fully understand. Therefore it is important that additional research is performed. In this section some recommendations will be made for this further research.

- In this research the influence of aluminium on the dissolution of BFS was not succeeded. In hindsight, different adjustments on the experiment could possibly give another outcome to this experiment, which would be useful. A recommendation is to further investigate the influence of the aluminium etching solution on the dissolution of the precursor. More specific recommendations for this experiment include performing titration of the etching solution and diluting the solution with sodium hydroxide to lower the aluminium content. As the exact pH of the etching solution is most probably not completely constant within a batch it is also recommended to perform titration of both the reference and etching solution containing medium to ensure the same pH for both liquids, excluding the possible influence of the pH on dissolution. It should be noted that the comparing the dissolution behavior of different solutions is already quite difficult as a lot of different parameters could influence the dissolution. The uncertainty of the composition of the aluminium etching solution adds another challenge to this experiment.
- A more detailed research on the influence of the aluminium etching solution on the reaction products forming and exact composition is recommended as in this research relatively easy experiments for the characterization were performed. A more detailed SEM-EDS study could give better insight in the influence of the aluminium etching solution. In this research only the 28 day samples were considered in the SEM-EDS as due to too high temperatures in the MIP room, my 1 and 7 day samples were inaccessible. By investigating the elemental composition of the reaction products over time, more evidence for the reaction mechanism can be gathered.
- In this research, the standard times of measurement of 1, 7 and 28 days are used. For some mixtures it can be seen that certain phenomena already occurred before the first measurement. An example of this is the occurrence of the first and second peak in the isothermal calorimetry which explained lower concentrations of Al after 1 day in the pore solution. By adding measurements within the first day and for example at 3 days and 14 days, a more complete overview can be created about the evolution of strength and formation of reaction products.
- A more detailed investigation into the formation of metastable phases and their role in creating a gel barrier, which may contribute to delayed reactions, is recommended. Currently, the gel barrier theory is supported by observed influences and existing literature. Further in-depth research could provide direct evidence of this phenomenon.
- For future application, more fresh and hardened properties should be investigated. Currently only strength and setting time are included, but if the goal is to really use the aluminium etching solution in practical applications, more fresh and hardened properties should be known and the research should be scaled up from past to mortar and concrete. A specific focus on the relation between the M_a and the autogenous shrinkage is recommended, where an analogy could be made to standard activators and its activator modulus M_s.
- In the research of Nugteren, significant compressive strengths were achieved with a relatively high amount of FA as precursor. Besides that, no cracks were observed. In this research, it was determined to only use BFS for the good and well-known properties. It turned out that the combination of BFS and the aluminium rich activator showed too high reactivity which is a reason to focus on hybrid precursors where BFS is combined with FA or even MSWI bottom ash.

The aluminium etching solution shows great potential and with further research and understanding, it could replace a part of the industrially produced activators, resulting in a even further reduction in emissions for geopolymer concrete and simultaneously removing the need for treatment of this solution in order to discard it.

A Appendix: Dissolution test of Al. containing solution

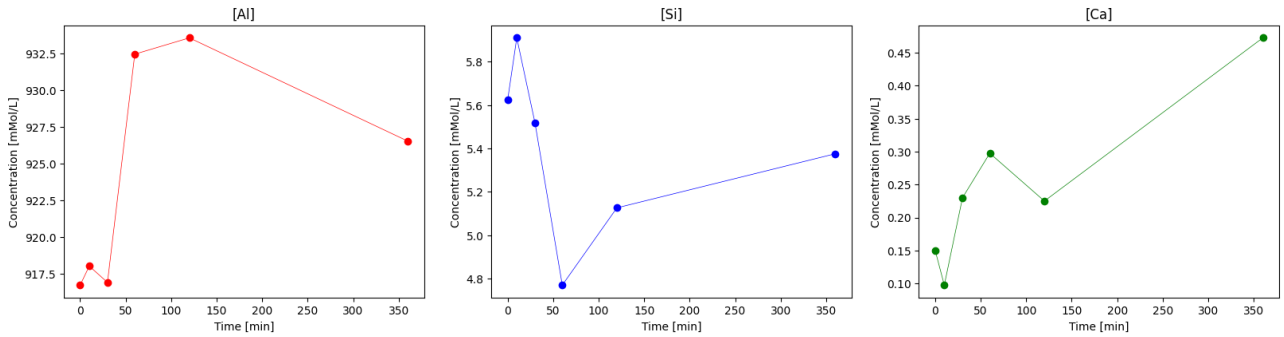

Figure 71: Concentrations of the elements over time for the alkaline waste containing solution

B Appendix: Dissolution test Zuo - Hesselmans

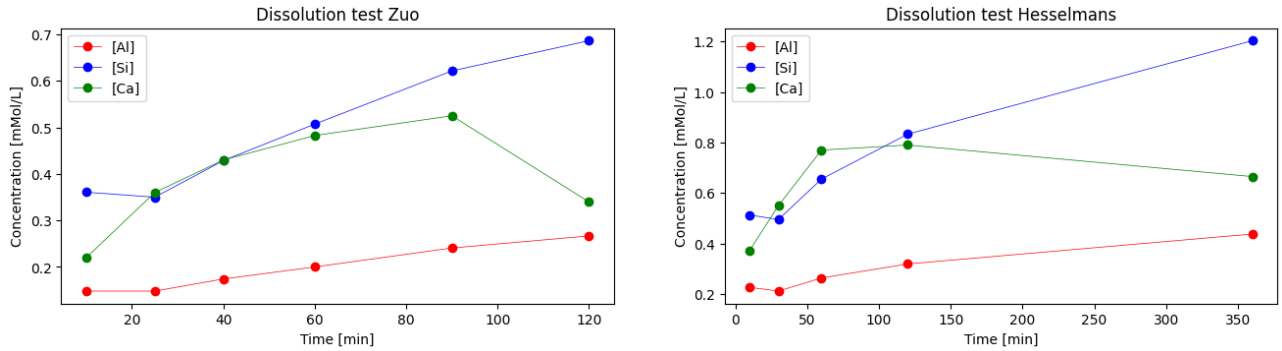

Figure 72: Concentrations of the elements over time compared between this research and that of Y. Zuo (Zuo, 2019).

C Appendix: Relation OH and Na in pore solution

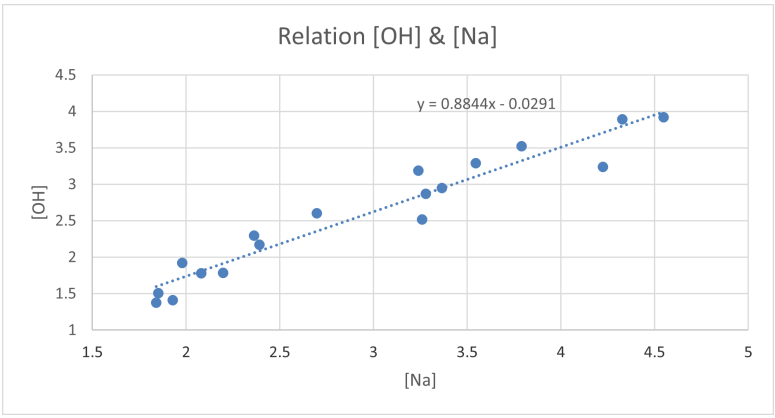

Figure 73: Relation between the hydroxide and sodium concentration of all the measured datapoints.

D Appendix: Knudsen model fitted to latter part of the data

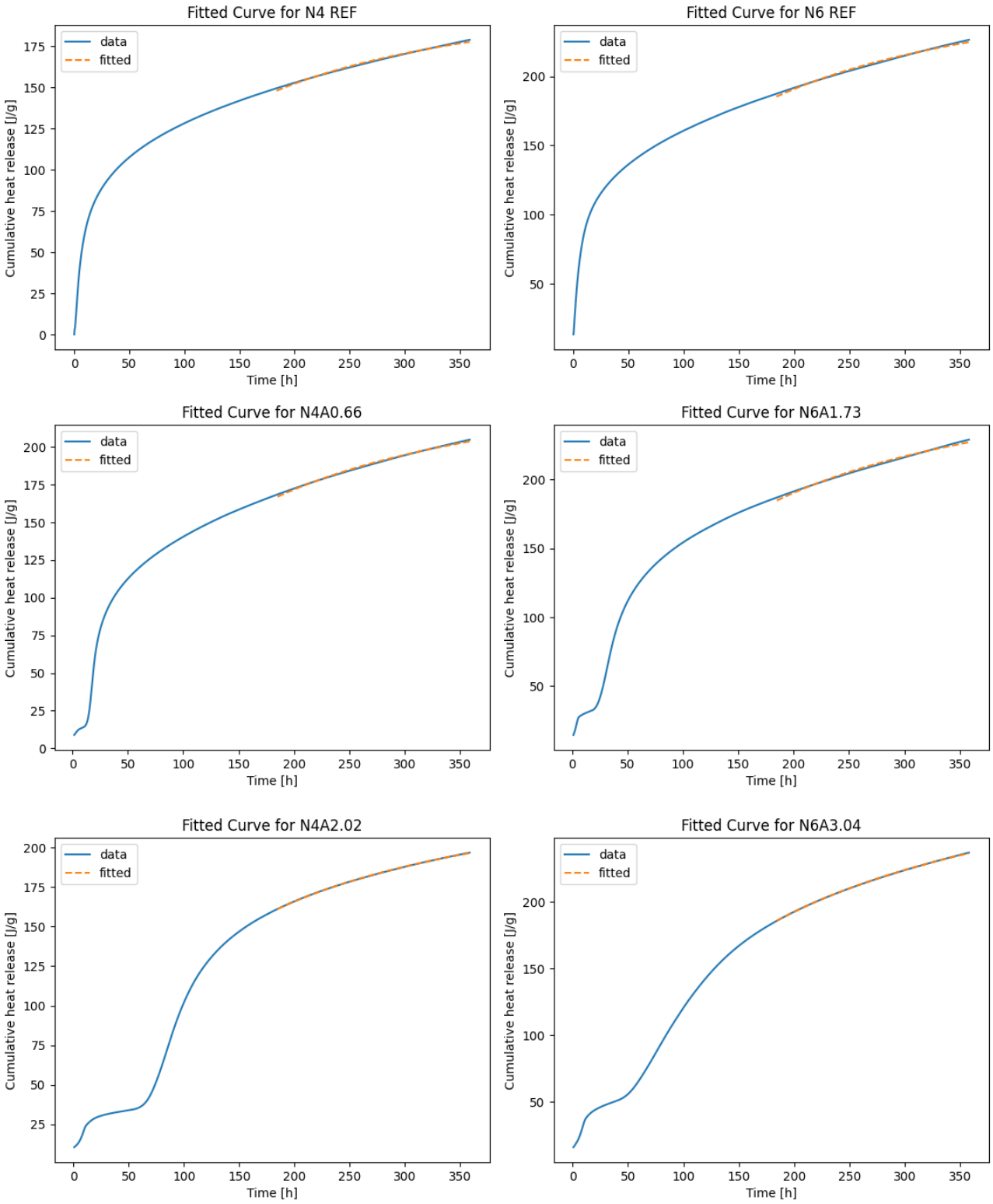

Figure 74: Creating subfigures in LaTeX.

E Appendix: Setting time related to calorimetry

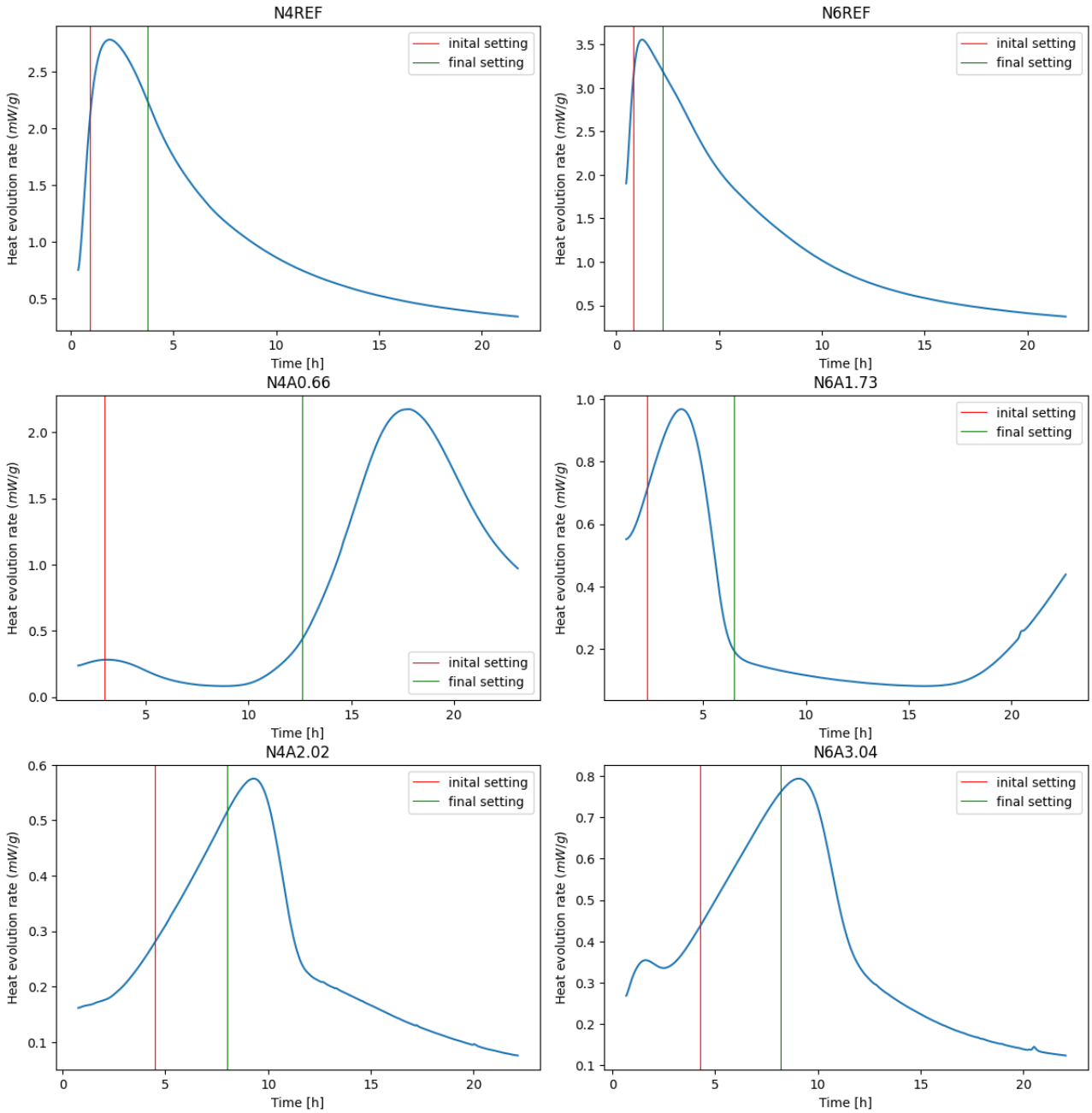

Figure 75: Setting times plotted in the heat of reaction plots

F Appendix: TGA results per mixture over time

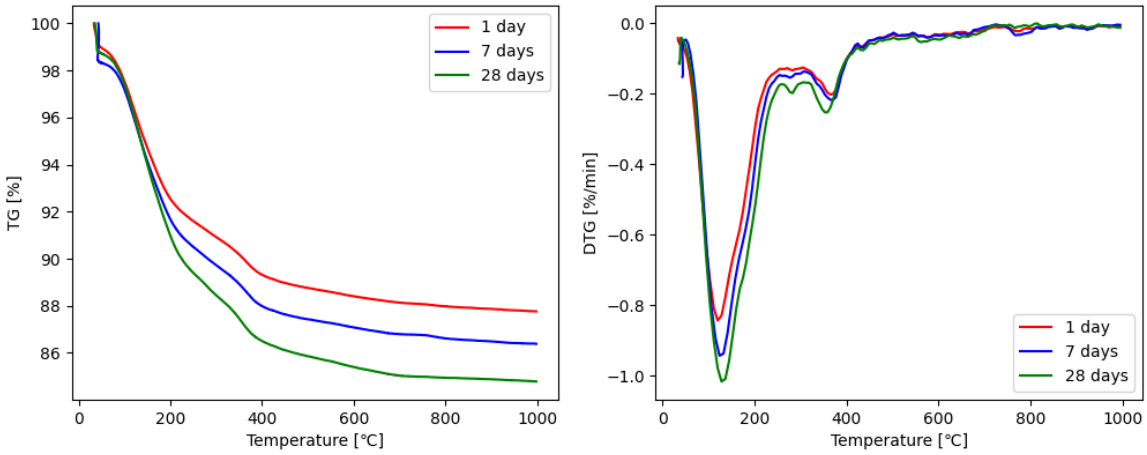

Figure 76: N4REF

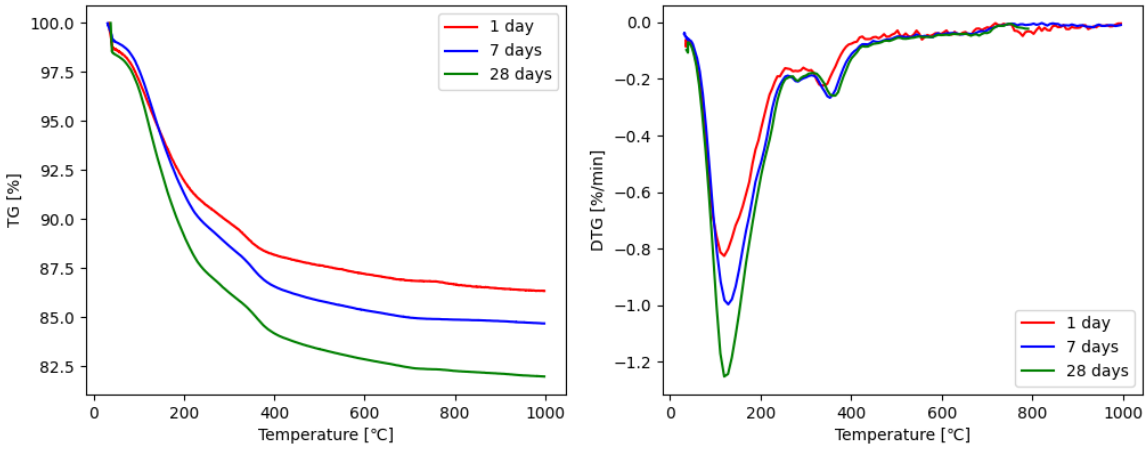

Figure 77: N4A0.66.

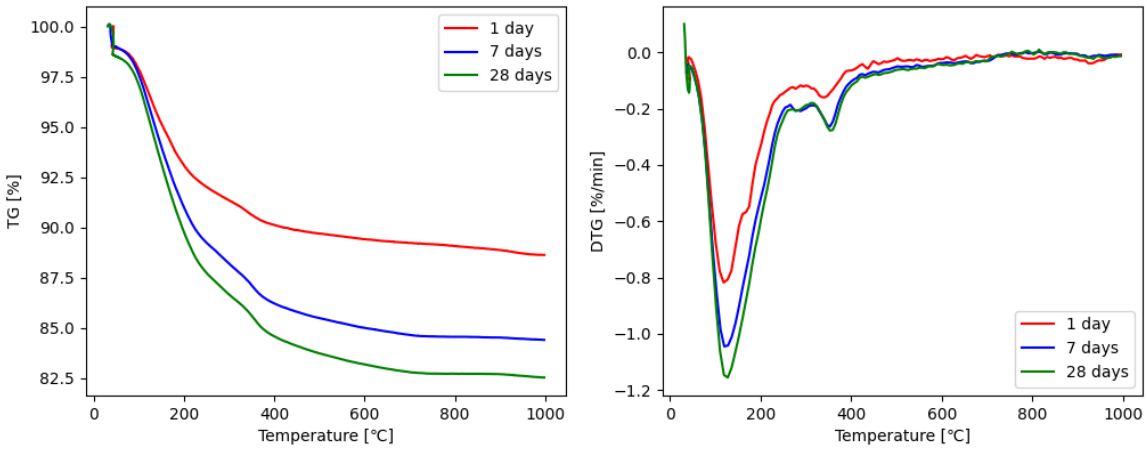

Figure 78: N4A2.02

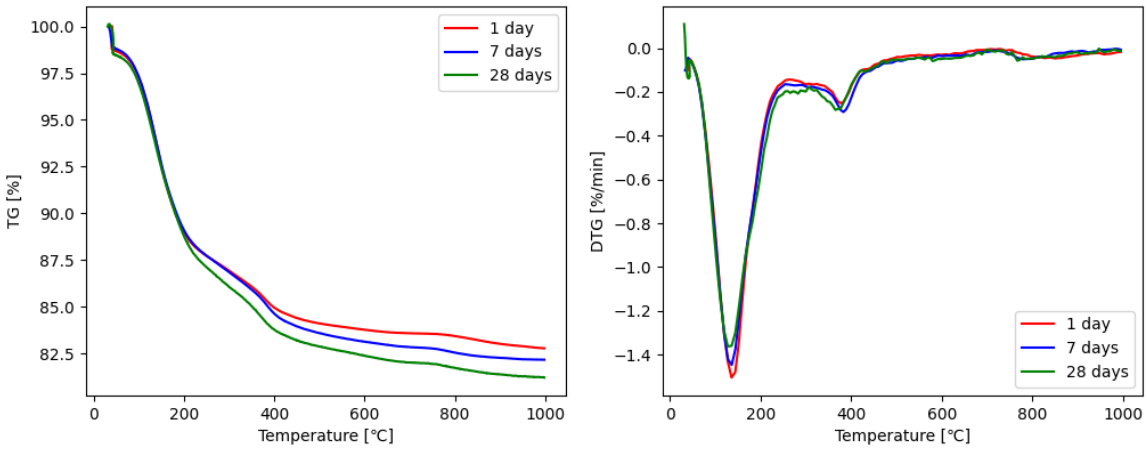

Figure 79: N6REF

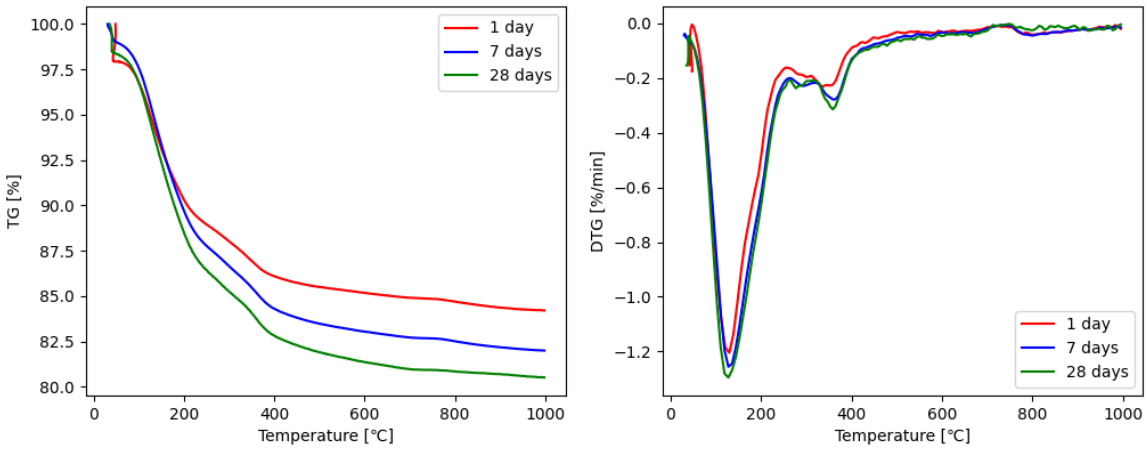

Figure 80: N6A1.73.

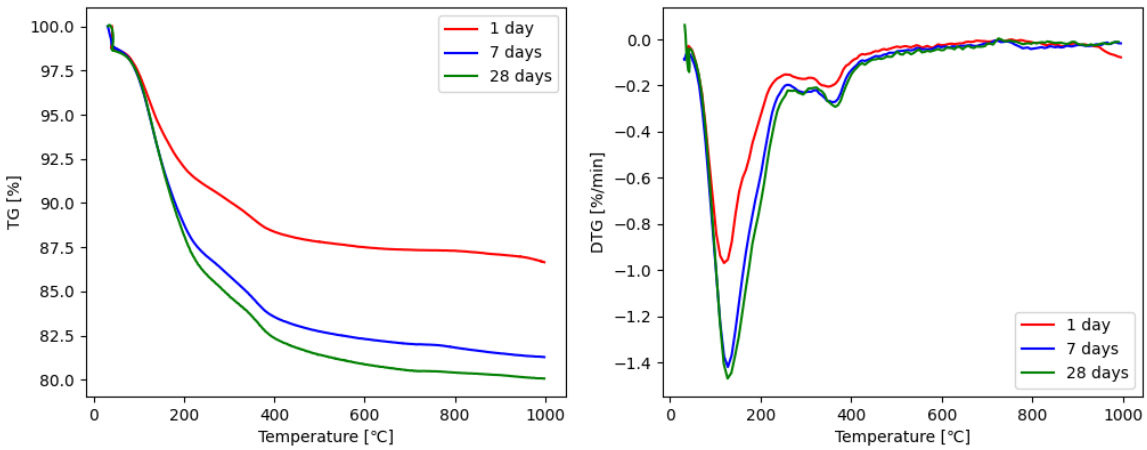

Figure 81: N6A3.04

G Appendix: XRD

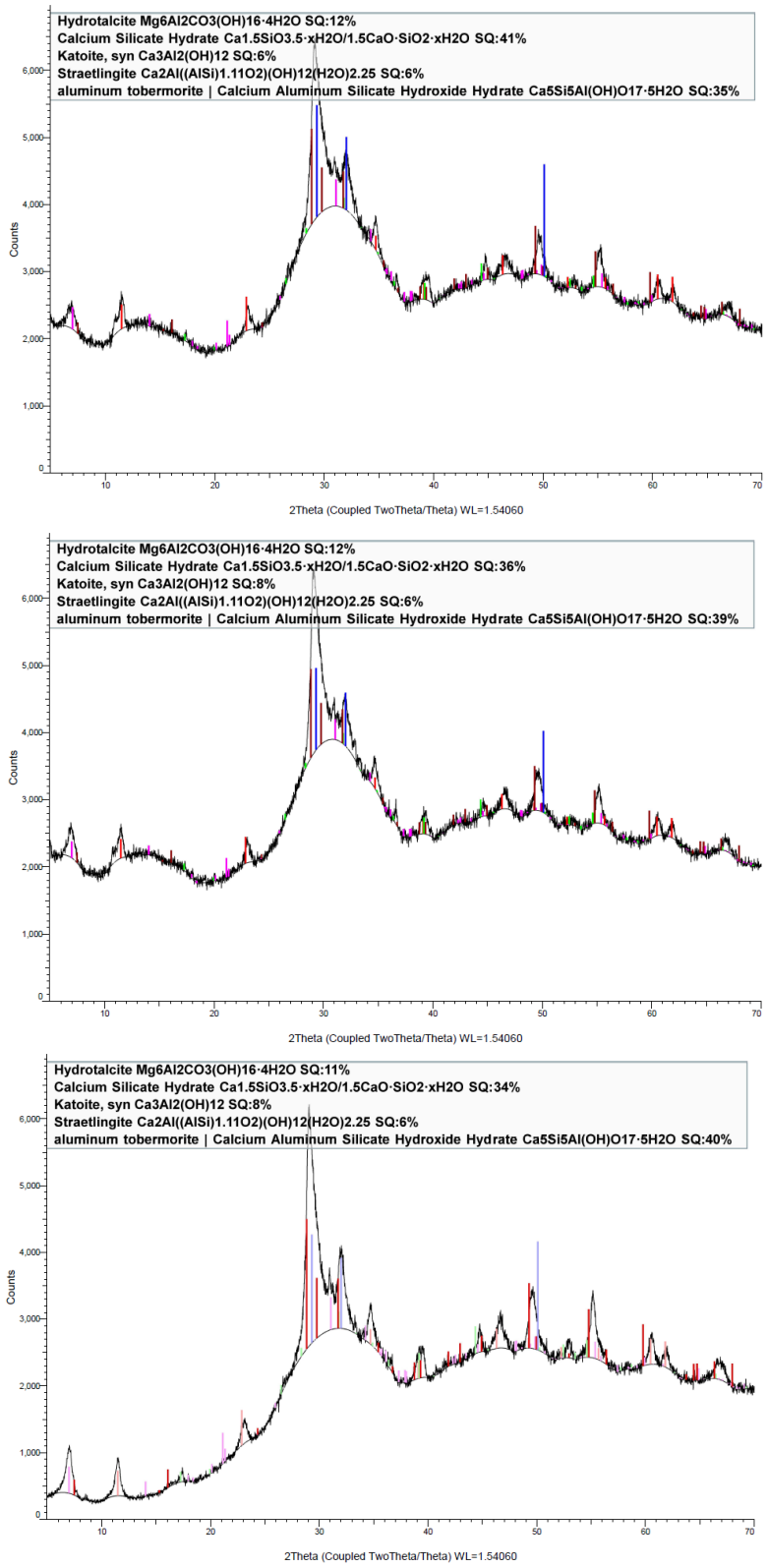

Figure 82: XRD results of N4REF at 1, 7 and days respectively

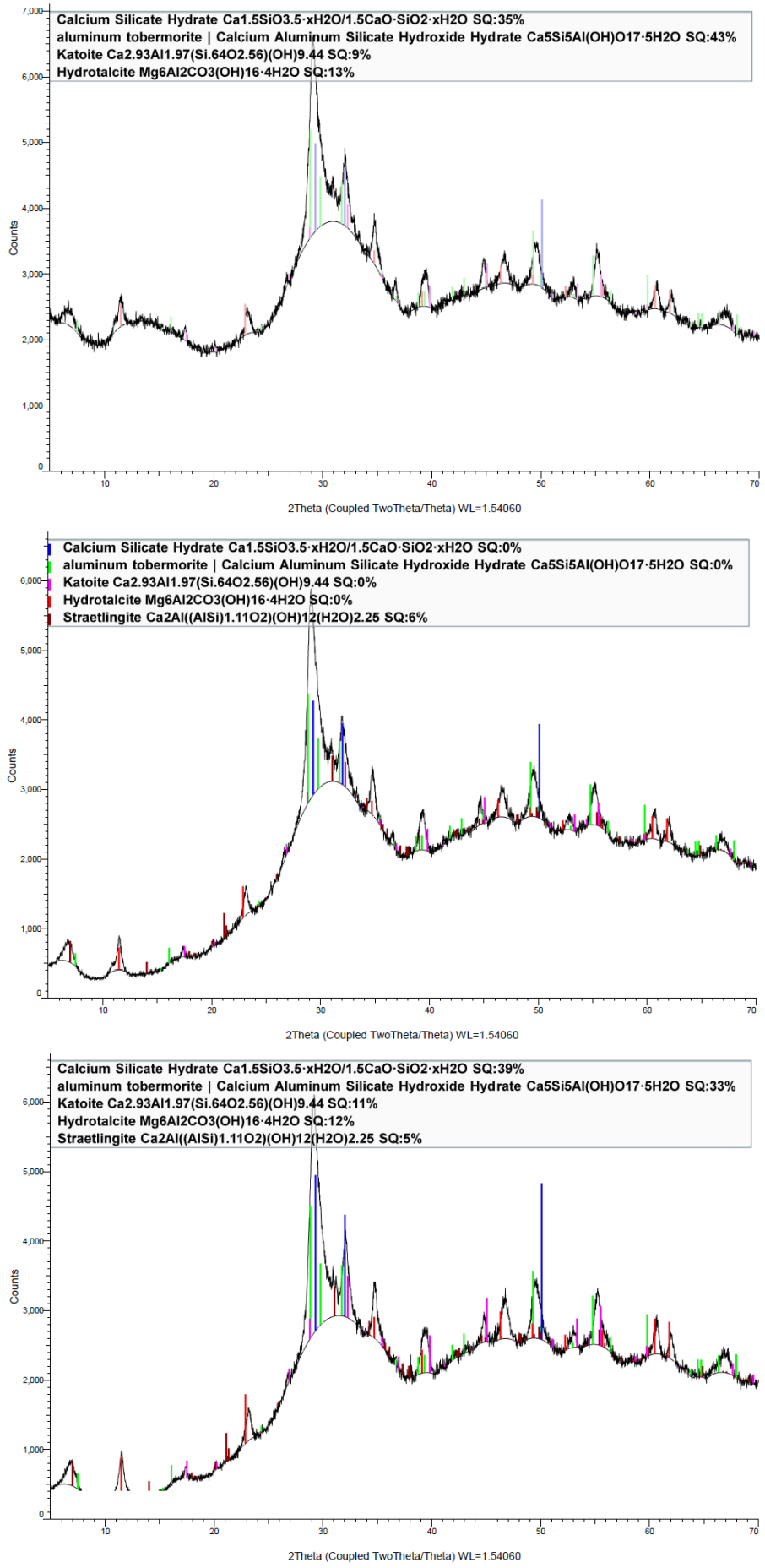

Figure 83: XRD results of N4A0.66 at 1, 7 and 28 days respectively

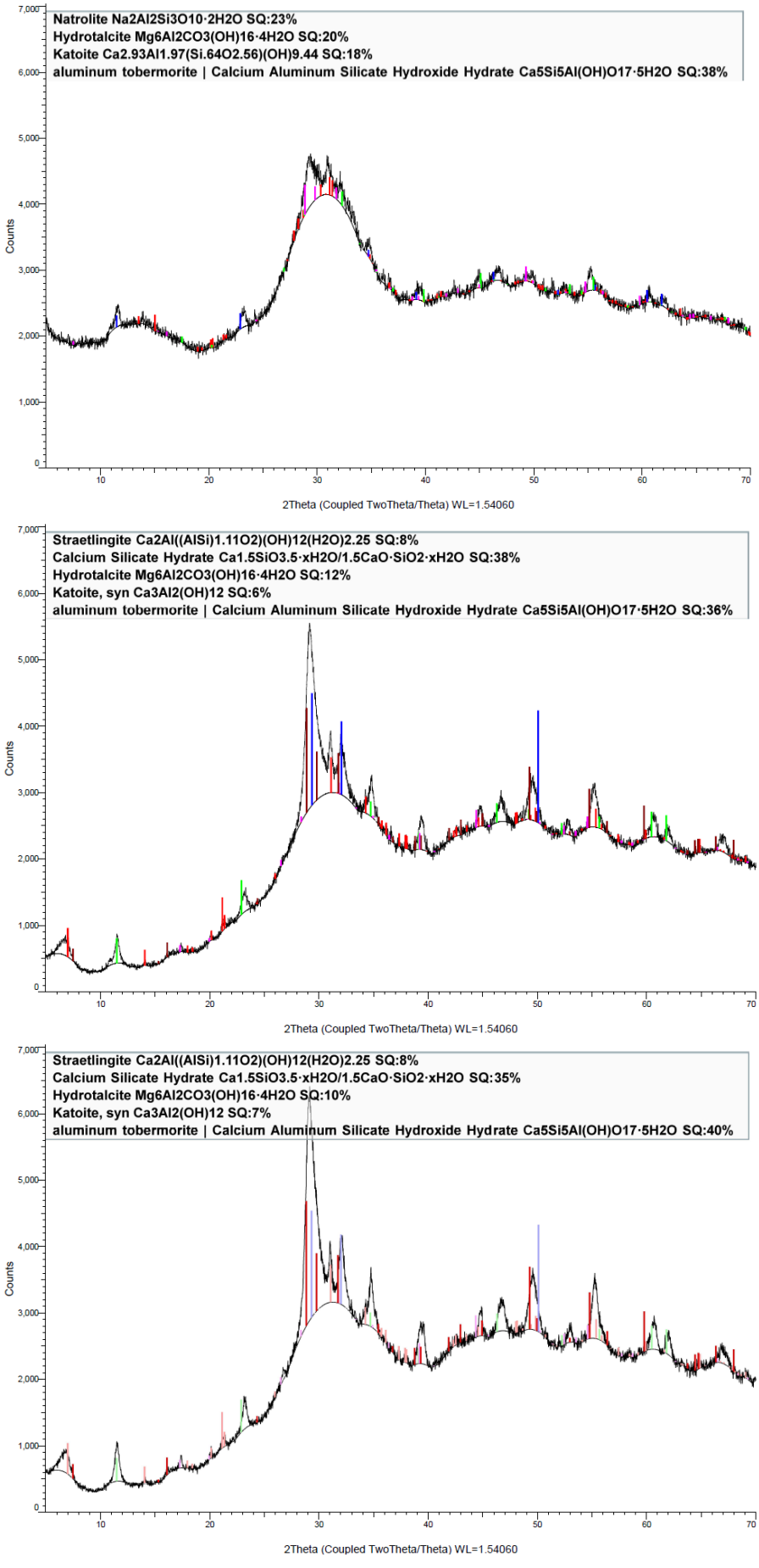

Figure 84: XRD results of N4A2.02 at 1, 7 and 28 days respectively

H Appendix: SEM-EDS

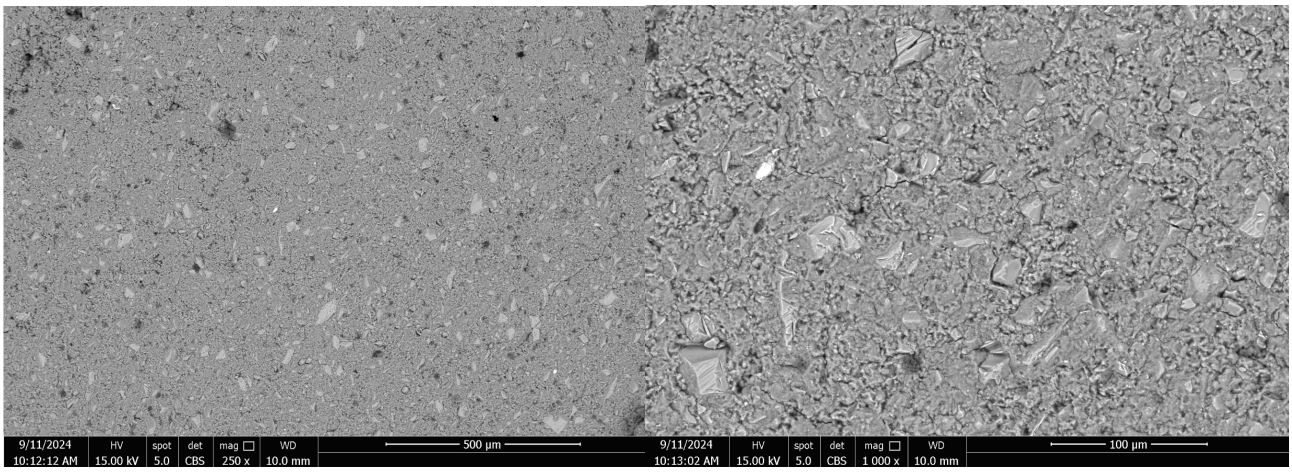

Figure 85: SEM images of N4REF at different magnifications

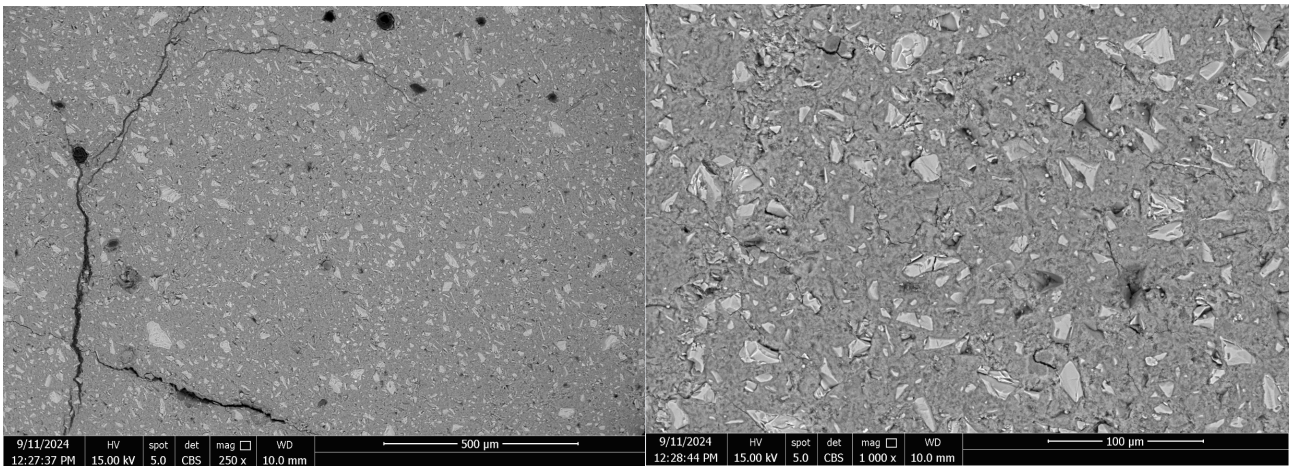

Figure 86: SEM images of N4A2.02 at different magnifications

References

Benhelal, E., Zahedi, G., Shamsaei, E., & Bahadori, A. (2013). Global strategies and potentials to curb co2 emissions in cement industry. *Journal of Cleaner Production*.

BetonAkkoord. (2018). *Betonakkoord voor duurzame groei* (Tech. Rep.). Ministry of Infrastructure and the Environment.

Bouzouaid, L., Lothenbach, B., Fernandez-Martinez, A., & Labbez, C. (2021). Portlandite solubility and ca2+ activity in presence of gluconate and hexitols. *Cement and Concrete Research*.

Chen, B., Wang, J., & Zhao, J. (2021). Effect of sodium aluminate dosage as a solid alkalineactivator on the properties of alkali-activated slag paste. *Advances in Materials Science and EngineeringVolume 2021*.

Chithiraputhiran, S., & Neithalath, N. (2013). Isothermal reaction kinetics and temperature dependence of alkali activation of slag, fly ash and their blends. *Construction and Building Materials*.

Duxson, P., Provis, J. L., Lukey, G. C., Mallicoat, S. W., Kriven, W. M., & van Deventer, J. S. (2005). Understanding the relationship between geopolymer composition, microstructure and mechanical properties. *Colloids and Surfaces A: Physicochemical and Engineering Aspects Volume 269, Issues 1–3, 1 November 2005, Pages 47-58*.

Glukhovsky, V. (1994). Ancient, modern and future concretes. *Proceedings of the first international conference on alkaline cements and concretes (Vol. 1, pp. 1-8)*.

Graham, T. R., Hu, J. Z., Jaegers, N. R., Zhang, X., Pearce, C. I., & Rosso, K. M. (2022). *An amorphous sodium aluminate hydrate phase mediates aluminum coordination changes in highly alkaline sodium hydroxide solutions* (Tech. Rep.). INORGANIC CHEMISTRY FRONTIERS.

Kapeluszna, E., Łukasz Kotwica, Rózycka, A., & Łukasz Gołek. (2017). Incorporation of al in c-a-s-h gels with various ca/si and al/si ratio: Microstructural and structural characteristics with dta/tg, xrd, ftir and tem analysis. *Construction and Building Materials*.

Kónya, P., & Földvári, M. (2008). Thermoanalytical investigation of cavity filling natrolite group minerals in basalts. *Journal of Thermal Analysis and Calorimetry, Vol. 94 (2008) 1, 209–218*.

Lambert, P., & Mangat, P. (2016). *Sustainability of construction materials, chapter 18: Sustainability of alkali-activated cementitious materials and geopolymers*. Woodhead Publishing.

(2023). (Lecture slides, $B2_U2_W6_L2_Alkaliactivatedmaterialsand Geopoymerconcrete_fundamentalsandmixdesign$)

Li, J., Geng, G., Myers, R., Yu, Y.-S., Shapiro, D., andCarlo Carraro, ... Monteiro, P. J. (2019). The chemistry and structure of calcium (alumino) silicate hydrate: A study by xanes, ptychographic imaging, and wide- and small-angle scattering. *Cement and Concrete Research*.

Li, Z., Zhang, S., Liang, X., & Ye, G. (2020). Cracking potential of alkali-activated slag and fly ash concrete subjected to restrained autogenous shrinkage. *Cement and Concrete Composites*.

Liu, T., Chen, Y., Yuan, B., Zhuang, W., Brouwers, H., & Yu, Q. (2024). Sodium aluminate activated waste glass: Reduced efflorescence behavior by c(n)ash transformation. *Cement and Concrete Research*.

Liu, T., Tang, Y., Ling, X., Stapper, J., Kunther, W., & Yu, Q. (2024). Naalo2 activated slag and mswi bottom ash: Phase assemblages and thermodynamic assessment of long-term leaching behavior. *Cement and Concrete Composites*.

Liu, T., Yu, Q., & Brouwers, J. H. (2022). In-situ formation of layered double hydroxides (ldhs) in sodium aluminate activated slag: The role of al-o tetrahedra. *Cement and Concrete Composites*.

Lothenbach, B. (2010). Thermodynamic equilibrium calculations in cementitious systems. *Materials and Structures/Materiaux et Constructions*.

Marvila, M. T., de Azevedo, A. R. G., & Vieira, C. M. F. (2020). Reaction mechanisms of alkali-activated materials. *IBRACON Structures and Materials*.

Myers, R. J., Bernal, S. A., & Provis, J. L. (2014). A thermodynamic model for c-(n-)a-s-h gel: Cnash-ss. derivation and validation. *Cement and Concrete Research*.

Myers, R. J., Bernal, S. A., & Provis, J. L. (2017). Phase diagrams for alkali-activated slag binders. *Cement and Concrete Research*.

Myers, R. J., Lothenbach, B., Bernal, S. A., & Provis, J. L. (2015). Thermodynamic modelling of alkali-activated slag cements. *Applied Geochemistry*.

Nugteren, H.-W. (2010). *Secondary industrial minerals from coal fly ash and aluminium anodising waste solutions* (Unpublished doctoral dissertation). Delft University of Technology.

Okoronkwo, M. U., & Glasser, F. P. (2016). Strätlingite: compatibility with sulfate and carbonate cement phases. *Materials and Structures*.

Paudel, S. R., Yang, M., & Gao, Z. (2020). ph level of pore solution in alkali-activated fly-ashgeopolymer concrete and its effect on asr of aggregates with different silicate contents. *Journal of Materials in Civil EngineeringVolume 32, Issue 9*.

Provis, J. L., & Bernal, S. A. (2014). Geopolymers and related alkali-activated materials. *Annual Review of Materials Research*.

Provis, J. L., & van Deventer, J. S. (2014). *Alkali activated materials state-of-the-art report, rilem tc 224-aam*. Springer.

Scrivener, K., Snellings, R., & Lothenbach, B. (2015). *A practical guide to microstructural analysis of cementitious materials*. CRC Press.

Snellings, R., Chwast, J., Özlem Cizer, Belie, N. D., Dhandapani, Y., Durdzinski, P., ... Lothenbach, B. (2018). Rilem tc-238 scm recommendation on hydration stoppage by solvent exchange for the study of hydrate assemblages. *Materials and Structures*.

Sun, B., Ye, G., & de Schutter, G. (2022). A review: Reaction mechanism and strength of slag and fly ash-based alkali-activated materials. *A review: Reaction mechanism and strength of slag and fly ash-based alkali-activated materials*.

Sun, Y., Wang, Z., Park, D., Chen, Y., Kim, H., Kim, W., & Lee, H. (2023). Mathematical determination of the maximum heat release for fly ash cement paste: Effect of heat flow monitoring time, calculation approach and fly ash content. *Thermochimica Acta*.

Wang, J., Hu, Z., Chen, Y., Huang, J., Ma, Y., Zhu, W., & Liu, J. (2022). Effect of ca/si and al/si on micromechanical properties of c(-a)-s-h. *Cement and Concrete Research*.

Yuksel, I. (2018). *Waste and supplementary cementitious materials in concrete, chapter 12: Blast furnace slag*. Woodhead Publishing.

Zhang, S., Keulen, A., Arbi, K., & Ye, G. (2017). Waste glass as partial mineral precursor in alkali-activated slag/fly ash system. *Cement and Concrete Research Volume 102, December 2017, Pages 29-40*.

Zhang, S., Li, Z., Ghiassi, B., Yin, S., & Ye, G. (2021). Fracture properties and microstructure formation of hardened alkali-activated slag/fly ash pastes. *Cement and Concrete Research*.

Zuo, Y. (2019). *Experimental study and numerical simulation of the reaction process and microstructure formation of alkali-activated materials* (Unpublished doctoral dissertation). Delft University of Technology.